DIODE-LASER SENSORS FOR HARSH ENVIRONMENTS WITH APPLICATION TO PULSE DETONATION ENGINES

Report No. TSD-142

Scott Thomas Sanders
November 2001

.

Abstract

Diode-laser sensors have been developed for monitoring gas properties (e.g., temperature, pressure, velocity, and species concentrations) in relatively harsh (high-pressure, high-temperature, multiphase, and transient) combustion flows. The sensors have been applied to study an experimental propulsion concept, the pulse detonation engine (PDE), with the goal of enhancing PDE development and modeling efforts.

Optically harsh environments present many challenges, including severely broadened absorption features, limited spectroscopic data, extinction, and beam steering. To enable quantitative measurements in the midst of these challenges, two advanced sensing strategies have been fostered: wavelength multiplexing and broad wavelength scanning. Both strategies attempt to recover broad spectral information with fast time response (coined, "all spectra, all the time"), enabling straightforward measurement of high-pressure absorbers as well as rejection of both spectrally broadband and slowly varying noises. Wavelength multiplexing has been employed to measure H_2O mole fraction and temperature in PDEs (Chapter 3); broad wavelength scanning has been employed to measure C_2H_4 fuel in PDEs (Chapter 3), gas temperature and pressure in Cs-seeded PDEs (Chapter 3), high pressure and nonuniform-temperature O_2 in static cells (Chapter 4), and high pressure H_2O in static cells (Chapter 4). The sensors demonstrated in static cells are modeled after successful PDE sensors but are intended to support measurements in other harsh environments such as gas turbine and piston engines.

Acknowledgements

I would like to thank my adviser, Prof. Hanson, for enthusiastic support and for encouraging my creative tendencies. I wish to thank my reading committee, Prof. Edwards and Dr. Jeffries, for devoting time to this thesis and for assistance throughout my Ph.D. studies.

Special thanks are due to John Herbon and Jon Koch, for finding time to help me on a moment's notice and to my colleagues: David Davidson, Shang-I Chou, Ted Furlong, Shawn Wehe, Michael Webber, Jian Wang, Brian Kirby, and David Horning; and to my PDE teammates: Tom Jenkins, Wei Fan, Jeff Baldwin, Nobuhiro Yamanishi, Jeff Bielicki, Muruganandam Thiruchengode, Dan Mattison, Lin Ma, Jon Liu, and Kevin Hinckley. Thank you all for your technical assistance as well as your friendship.

I would like to gratefully acknowledge Dr. Kailas Kailasanath at the Naval Research Laboratory for insightful discussions and for providing me with detonation simulation results.

Finally, thanks are due to my family for prayers and encouragement and especially to my wife, Beth, for unwavering companionship and guidance.

This research was supported by the Office of Naval Research, the Air Force Office of Scientific Research, and by General Electric Corporation.

Contents

List of Tables

List of Figures

Chapter 1

Diode-laser sensors for harsh flows: challenges and solutions

1. Introduction

Diode-laser absorption sensors have long been applied to measure gas properties (e.g., temperature, velocity, and species concentrations) in a variety of controlled laboratory experiments. Extensive work has been done in static cells (e.g., Varghese et al. 1980; Webber et al. 2001), flames and exhausts (e.g., Hanson 1980; Furlong et al. 1998; Wang et al. 2000), plasmas (e.g., Baer et al. 1992; Chou et al. 2001), and shock tubes (e.g., Hanson 1977; Nagali et al. 1999). The lessons learned in these applications have provided a strong foundation for the work detailed in this thesis: application of diode-laser sensors to gas-phase measurements in relatively harsh environments.

Diode lasers are now available at many wavelengths throughout the 0.2–20 μm range (Wang et al. 2001a). To perform the work described in this thesis, AlGaAs and InGaAsP lasers in the 0.7–1.8 μm range were chosen because they are advanced and inexpensive, owing in large part to the vast telecommunications market existing near 1.55 μm. Furthermore, this wavelength range is coincident with mature Si, InGaAs, and Ge detector technologies. Many species are accessible in this wavelength range, either through vibrational transitions (e.g., H_2O: sections 3.3, 4.6; fuels: section 3.2) or electronic transitions (e.g., O_2: sections 4.2–4.5; alkali metals: sections 3.4–3.5).

A simplified diode laser sensor is shown schematically in Fig. 1.1. A diode laser beam is directed through the flow of interest. The incident intensity is termed I_O and the transmitted intensity, monitored with a detector, is termed I. By measuring I, I_O, and L, the spectral absorption coefficient k_ν can be determined using the Beer-Lambert law (see also Arroyo et al. 1993):

$$\frac{I}{I_O} = e^{-k_n L} . \qquad \text{(eq. 1.1)}$$

Note that eq. 1.1 neglects light loss by processes other than gas absorption and assumes uniform properties along the line-of-sight. The functionality of the spectral absorption coefficient on gas properties, given for the usual case of additive absorption by

$$k_n = X_{absorber} P \sum_{i=1}^{N} S_i(T) f_i(n, T, P, X_j) , \qquad \text{(eq. 1.2)}$$

forms the foundation for gas sensing; $X_{absorber}$ is the mole fraction of the absorber, P [atm] is the gas pressure, S_i [cm^{-2}/atm] is the temperature-dependent linestrength of the i^{th} transition, ϕ_i [cm] is the frequency-, temperature-, pressure-, and composition-dependent lineshape function of the i^{th} transition, and N is the number of transitions existing in the spectral range of interest. S and ϕ are commonly obtained using databases such as HITRAN and HITEMP (Rothman et al. 1998). The challenges that arise when applying the basic sensor shown in Fig. 1.1 to harsh environments, and their solutions, are presented in this chapter.

2. Challenges

The pulse detonation engine (PDE), detailed in Chapter 2, is the archetype of an optically-harsh environment. Table 1.1 lists some of the PDE properties (column I) that cause a variety of sensing challenges (column II). Each of these challenges is present in most diode-laser sensing applications, but to a lesser degree than in the PDE. As an example, consider the sensor shown in Figure 1.1. If the alignment is sensitive enough (e.g., due to a very long path length, L), extremely small air currents (see Caron et al. 1998) can deflect the beam so that the detector registers a reduced intensity, I. Such sensitivity is known as beamsteering, and is undesirable in most diode-laser absorption measurements. Often, beamsteering can be removed with limited effort (e.g., reduced path length, focusing optics, or a larger detector). However, in the PDE environment, angular beam deflections of approximately 3 degrees are common, and these are not easily removed (see Appendix A). The PDE environment typically requires great attention to each challenge listed in Table 1.1.

Of the eight sensing challenges listed, two (broad absorption features and limited spectroscopic data) are purely spectroscopic. The remaining six can be considered noise sources; one of these (thermal emission) is an additive noise, and the rest are multiplicative noises. Additive noises are present even when the laser is off, whereas multiplicative noises modulate the intensity of the laser beam. Again considering Fig. 1.1, additive thermal emission noise radiated by hot gases or particulate in the flow is undesirable because it can be misidentified as increased laser transmission. Similarly,

multiplicative noise due to a fouled (e.g., soot-covered) window attenuates the laser beam; such noise can be confused with laser absorption by gases in the flow.

3. Specialty solutions

For each of the sensing challenges listed in Table 1.1, there is at least one "specialty solution" (see column III). Previous workers have engineered these specialty solutions to address the challenges listed in column II. Many have been thoroughly discussed in the literature (see the references in Table 1.1) and exercised in the applications listed in section 1.1. Because the PDE has severe versions of the same challenges solved previously, extended or modified versions of the same specialty solutions are often successful. As an example, thermal emission, typically eliminated by diffraction gratings *or* laser intensity modulation / lock-in amplification, is best removed from PDE experiments by applying *both* techniques simultaneously. Window fouling problems are another example. Traditionally, water condensation on optical surfaces has been combated by a purge flow of dry gas (e.g., Furlong, 1998). In PDE experiments, a liquid water film will condense on optical-access windows with a thickness that grows at a rate of approximately 4nm/μs (Sanders et al., 2001a). The growing thin films cause an undesirable oscillatory transmission *increase* because they act as transient antireflection coatings. Purge flows are not easily implemented in PDEs, so a modified solution, namely heating the windows to ~ 500 K, has been chosen. Transmission histories recorded in a PDE with and without heated windows are shown in Fig. 1.2.

One PDE challenge, beamsteering, and its specialty solution, uniform-response beam collection, deserves special attention. Initial work on uniform-response beam collection systems, designed to register transmitted beam intensities without any sensitivity to position, was performed in shock tube experiments (Petersen et al. 1997). This work has been extended to manage the relatively intense beamsteering present in PDE experiments, as detailed in Appendix A.

The specialty solution for laser beam extinction (cleaner flows) is only sometimes acceptable. For instance, if laser beam extinction is caused by dusty combustion gases, filtering the reactants to reduce particulate (and thus reduce laser beam extinction effects) is appropriate. However, if laser beam extinction is caused by fuel sprays or nascent soot, one cannot reduce these effects without fundamentally altering the flow. Such action is typically unacceptable. When measurements in multiphase flows are desired, there is, in fact, no specialty solution for laser beam extinction.

4. Universal solution: increased spectral information

One could employ all of the specialty solutions in Table 1.1 simultaneously to solve all of the severe measurement challenges (except for laser beam extinction) presented by PDEs. Although onerous, this approach has, in fact, been successfully demonstrated in a detonation tube at Stanford University; a resulting transmission versus time trace, demonstrating approximately 0.4% noise (presumably due to laser beam extinction) is presented in Fig. 1.3. Unfortunately, it is not only the application of

specialty solutions that is laborious, but also the *identification* of new sensing challenges that arise (for instance, the condensation problem evident in Fig. 1.2 was properly identified over a period of *years*). Fortunately, there is a simpler way to reduce noise. A single, universal solution to all of the challenges (including laser beam extinction) is available: increased spectral information. In this solution, transmission information is obtained at multiple wavelengths in a time that is short relative to the times that any of the noise sources (window birefringence, emission, extinction, window fouling, beamsteering, and mechanical vibration) change. Because these noise sources are frozen, their effects can be eliminated in a straightforward manner (detailed in section 1.5) as long as a measurable laser intensity still reaches the detector. In addition, if the spectral information encompasses a broad enough wavelength range, the spectroscopic challenges (spectrally-broad absorption features and limited spectroscopic data) can be mitigated. Thus, all of the challenges are solved with one elegant solution. Of course, the specialty solutions are still occasionally needed and should not be discarded. For instance, although increased spectral information enables schemes for rejecting emission noise, the specialty solutions described above are typically more efficient for this purpose.

5. Wavelength multiplexing and broad wavelength scanning

Increased spectral information is obtained in two ways: wavelength multiplexing and broad wavelength scanning, as depicted in Fig. 1.4. The wavelength multiplexing strategy uses many laser sources to interrogate multiple discrete wavelengths

simultaneously. Conversely, the broad wavelength scanning strategy modulates the wavelength of a single laser to obtain continuous spectral information throughout some spectral window.

The latter strategy is preferable in most cases for the following three reasons. First, it uses a simpler optical system (one laser as opposed to many). Second, as is evident from Fig. 1.4, it yields continuous spectral information, which is especially useful for eliminating challenges associated with broad absorption features and limited spectroscopic data. For example, the integrated area of an absorption transition (directly measured by broad wavelength scanning but not easily obtained by wavelength multiplexing) is insensitive to the (usually unknown) lineshape broadening parameters (Sanders et al. 2001b). Also, continuous spectral information allows straightforward compensation for mildly wavelength-dependent noise sources. For example, soot particles in combustion flows typically acquire a complicated size distribution, and the wavelength-dependence of their extinction is therefore seldom predictable. This fact can make it difficult to interpret transmission information at several discrete wavelengths. However, with continuous spectral information, an arbitrary polynomial can be used to "fit away" all noise sources that have a weak wavelength-dependence relative to the gas phase absorbers, as detailed in the literature (Wang et al. 2001b). The third reason broad wavelength scanning is preferable to wavelength multiplexing is that a single, scan-wavelength laser beam is usually immune to noise sources that vary across the beam diameter. For example, if a scan-wavelength beam becomes partially clipped (e.g., by beamsteering), all wavelengths interrogated during the scan will be similarly affected. To contrast, in a multiplexed beam, the energy at the various wavelengths may be differently

distributed through space; in this case, partial clipping will affect the wavelengths differently, and this difference is likely to be interpreted as absorption. Thus, to the extent that noise sources vary over the beam diameter, multiplexed beams must be "co-energetic" as well as co-linear; this requirement is not always easily met.

Despite these three advantages of broad wavelength scanning, wavelength multiplexing still enjoys frequent application, often because sufficiently tunable lasers are not available at appropriate wavelengths. However, even when such lasers are available, wavelength multiplexing may be favorable when speed outweighs accuracy as a measurement goal (i.e., for combustion control). Because wavelength multiplexing delivers less information, the accompanying data reduction techniques are necessarily faster. Another upside to the sparse spectral information offered by wavelength multiplexing is that the sensor spends all of its time interrogating the most critical parts of the absorption spectrum (typically absorption maxima and minima). Thus, no time is "wasted" on broad scans through the less-critical portions of the spectrum. This advantage becomes critical when temporal averaging is employed to enable measurements of very weak absorbers.

Armed with increased spectral information and select specialty solutions, diode laser sensors have been successful in pulse detonation engines, as detailed in chapter 3.

PDE properties	Sensing challenges	Specialty Solutions
High pressures (up to 50 atm)	Broad absorption features	Basic spectroscopic studies
	Stress-induced window birefringence	Conditioned windows (Petersen et al. 1997)
High temperatures (up to 4000 K)	Limited spectroscopic data	Basic spectroscopic studies
	Thermal emission	Filters or diffraction gratings
		Laser intensity modulation / lock-in amplification
Multiphase (soot and liquid fuel)	Laser beam extinction	Cleaner flows
	Window fouling	Purged (Furlong 1998), self-cleaning, or heated windows
Shock waves	Beamsteering	Uniform-response detection (Appendix A; Petersen et al. 1997)
	Mechanical vibrations	Rugged optical systems

Table 1.1. Summary of PDE measurement challenges and associated solutions

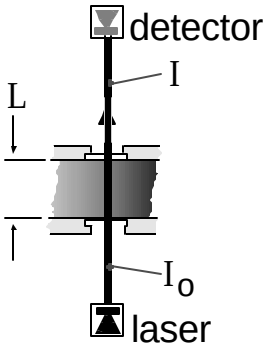

Figure 1.1. Basic diode laser sensor, highlighting incident intensity $I_{O,}$ transmitted intensity I, and path length L.

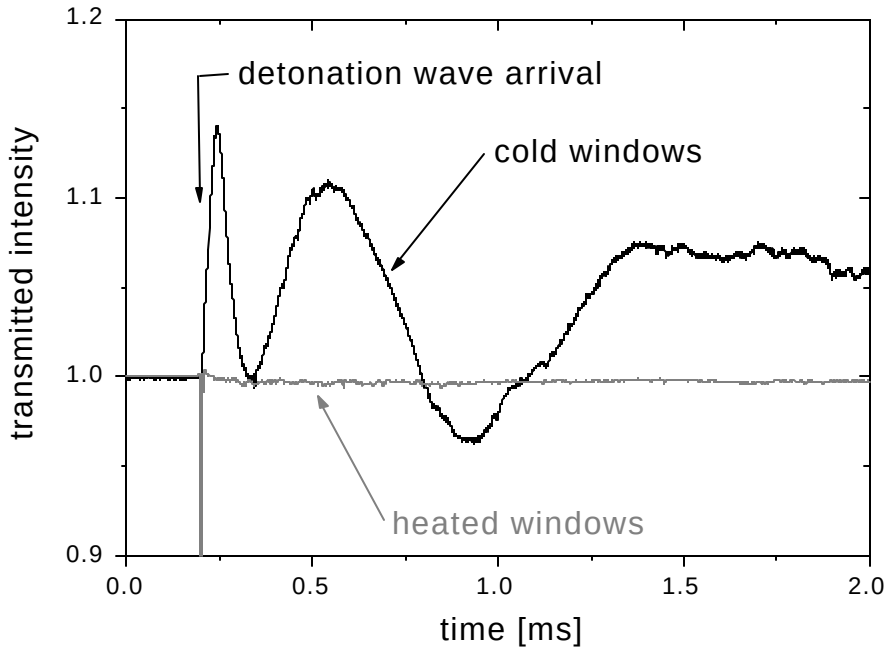

Figure 1.2. Transmission histories recorded during a single pulse of the Stanford PDE. Heated windows, a specialty solution listed in Table 1.1, remove a major noise source associated with water condensation on PDE optical access windows.

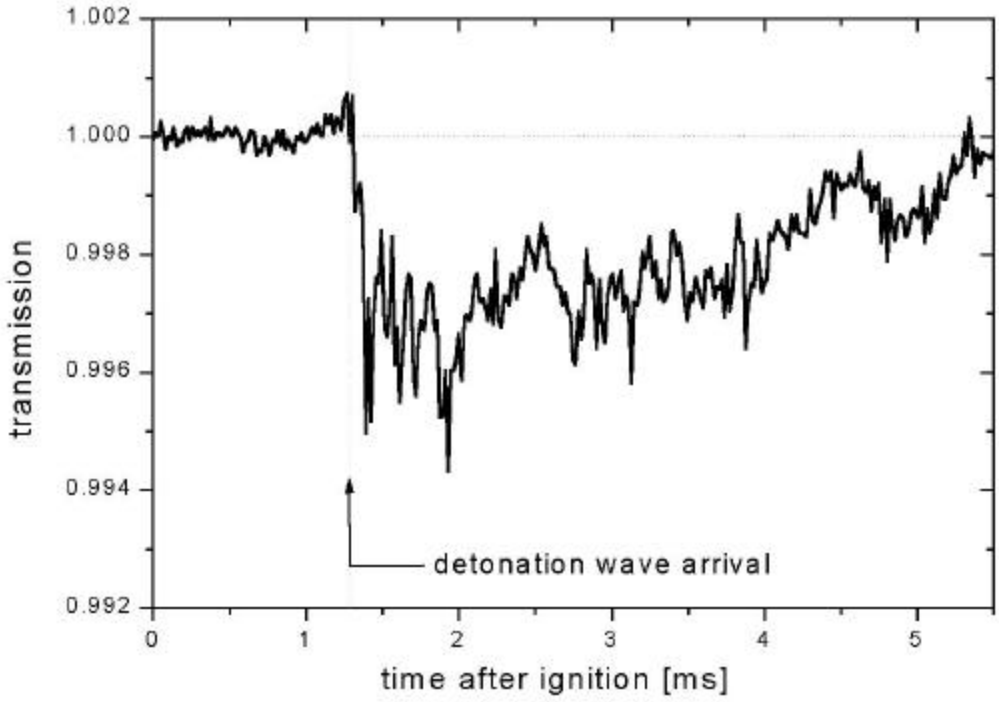

Figure 1.3. Transmission history recorded during a single pulse of the Stanford PDE. Appropriate specialty solutions from Table 1.1 have been applied to minimize noise. The remaining noise is presumably due to extinction and therefore can only be removed by removing particulate from the flow.

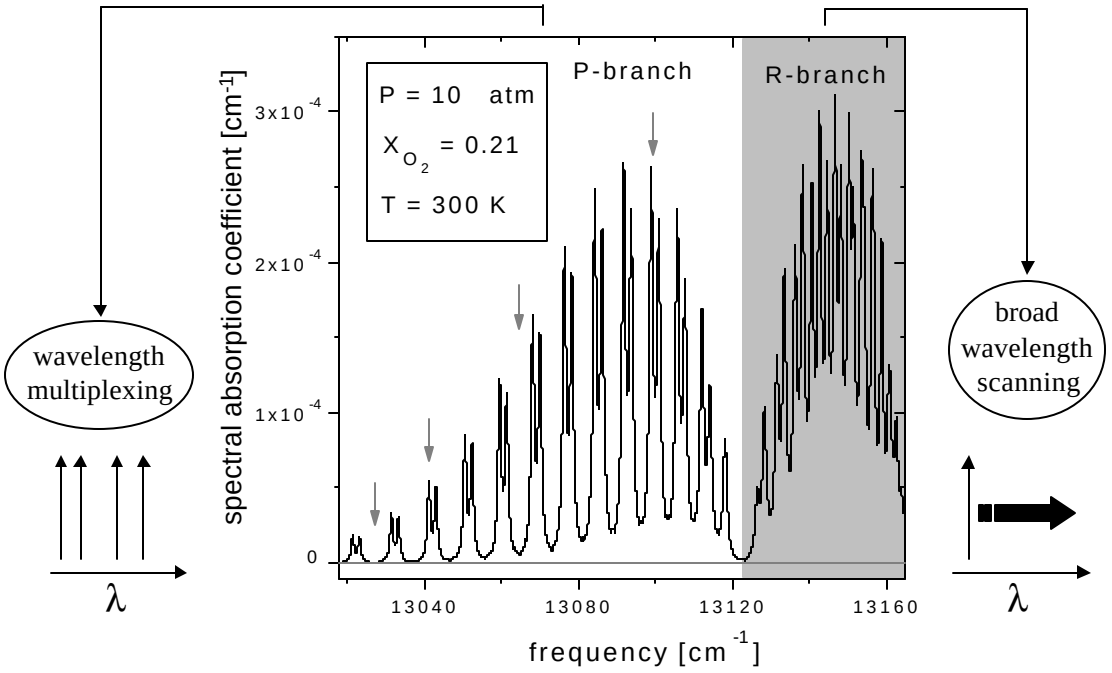

Figure 1.4. High-pressure O_2 absorption spectrum highlighting two techniques for obtaining increased spectral information: wavelength multiplexing and broad wavelength scanning.

Chapter 2

Pulse detonation engines

1. Introduction

The pulse detonation engine (PDE) concept dates back to the German V-1 "buzz bombs" of World War II, which were designed to employ detonations, but in practice were only "pulse deflagration engines". Motivated by potential advantages over conventional propulsion concepts (see, e.g., Eidelman 1997; Bussing et al. 1994), several researchers have studied PDEs extensively, both experimentally (e.g., Schauer et al. 2001; Brophy et al. 2000) and numerically (e.g., Kailasanath et al. 2000a; Mohanraj et al. 2001). Although most of the experimental studies have used traditional sensors (such as pressure transducers), some optical studies of PDEs have recently been reported (Lee et al. 2000; Shepherd et al. 2001). At present, PDEs are most commonly envisaged as airbreathing thrusters for ~ Mach 2 flight.

2. Chronology of a PDE cycle

The PDE cycle is depicted as a six-stage event in Figure 2.1. The PDEs studied in this thesis are simple stainless steel pipes, closed at one end (the "head end") and open at the other ("tail") end. In stage 1, a detonable mixture is delivered to the tube at the head

end. When the mixture has partially- or fully-filled the tube, an ignition event (stage 2) initiates a deflagration near the head end. If conditions are right, the deflagration will transition to a detonation that propagates toward the tail end of the tube (stage 3) at a velocity of roughly 2 km/s (depending on the fill mixture properties). The detonation exits the tube (stage 4), leaving behind a tube full of high-pressure gas. Rarefaction waves propagate back into the tube to exhaust the burned gases (stage 5), and after a series of "breathing" oscillations, the tube is left with residual combustion products. After a delay (stage 6), the cycle repeats.

3. Simple detonation model

A one-dimensional, method-of-characteristics view of the actual detonation event provides insight into PDE physics as well as a means for calculating PDE properties for comparison with measured data. A simplified x-t diagram is shown in Fig. 2.2. The detonation is assumed to initiate as a fully-developed Chapman-Jouget wave at the origin. This wave (bold in Fig. 2.2) is followed by an expansion fan that serves to decelerate the gas behind the wave to zero velocity, enforcing the zero-velocity head end boundary condition. Standard method-of-characteristics techniques (e.g., Thompson 1971) can be used to calculate gas properties (temperature T, pressure P, and burned gas velocity u) in the dark shaded region of Fig. 2.2, typically assuming a constant ratio of specific heats k = $k_{C\text{-}J}$. Using T and P, species mole fractions such as the water vapor mole fraction, X_{H2O}, can be obtained with a chemical equilibrium solver. Sample gas property

calculations for a slice along time t_1 are shown in Fig. 2.3. Fig 2.3 represents an instantaneous spatial distribution of gas properties in a tube of length L = 1.35 m with stoichiometric C_2H_4 / air reactants. The gas properties are normalized by the appropriate Chapman-Jouget values: $X_{H2O,C-J}$ = 0.1123, T_{C-J} = 2927 K, P_{C-J} = 18.36 atm, and u_{C-J} = 818 m/s. Note that the wave speed V_{C-J} = 1822 m/s is not shown in Fig 2.3. Calculations along fixed x, such as the slice at x_1 indicated in Fig. 2.2, can be compared to diode-laser sensor data such as gas temperature histories, as demonstrated in section 3.3. Because simple method-of-characteristics solutions are only available in the dark shaded regions of Fig. 2.2, more advanced models are desired.

4. Detailed detonation model

The detailed detonation simulations presented in this thesis were performed by workers at the Naval Research Laboratory (NRL) in Washington, D.C. In brief, the simulations use a flux-corrected transport (FCT: a high-order, monotone-explicit method) model for convection and an induction parameter model (IPM) for chemistry; these are coupled using time step splitting techniques. The IPM employs real gas thermodynamics but essentially fixes the species concentrations and ratio of specific heats, k, at their Chapman-Jouget values. Like the simple model described above, the detonation is assumed to initiate immediately at the head end. Heat transfer to PDE walls is not considered. Although the simulations are one-dimensional in space, specification of the exit-end boundary condition is guided by two-dimensional simulations performed over a

large numerical domain. Further details are available in the literature (Kailasanath et al. 2000a, 2000b).

5. Diagnostics needs

Near stages 1, 4, 5, and 6 of Fig. 2.1 are listed PDE properties that have been measured using diode-laser sensors (select sensors, highlighted in Fig. 2.1, are detailed in Chapter 3; the remainder are discussed in the literature). Measurements of these properties have been previously unavailable via traditional techniques, but are needed for PDE development, model validation, and active PDE control.

In particular, the stage 1 measurements (fuel vapor concentration, oxygen concentration, oxygen temperature, and fuel spray properties in the liquid-fueled case) are needed to intelligently tailor PDE charges. In some cases, charges must be tailored to create an initial (pre-detonation) condition that can be easily modeled; typically this is a charge with well-known (within 5%), uniform (within 5%) equivalence ratio. In other cases, charges must be tailored to meet a PDE performance goal (e.g., maximum impulse, maximum specific impulse, or maximum spray vaporization in the liquid-fueled case).

Stages 4 and 5 measurements (water temperature, water concentration, soot volume fraction, gas velocity, Cesium temperature, and Cesium pressure—Cesium is seeded as a tracer) are used for direct comparison to PDE models. The details of burned gas velocity histories, for instance, are a very sensitive test of model validity. Likewise,

measurements of water concentration provide a check that a model's treatment of PDE combustion chemistry is appropriate.

Stage 6 measurements (water temperature and water concentration) are critical for improving PDE performance. In practical PDEs, the engine designer attempts to minimize the duration of the stage 6 delay to maximize the engine pulse rate and, in turn, maximize the average engine thrust. When stage 6 becomes too short, however, the reactants injected in stage 1 may autoignite, and the engine degenerates to a pulsed torch-in-a-pipe that produces very little thrust. Sensors that can monitor the temperature during the stage 6 delay can determine when it is safe to repeat stage 1. Active, diode-laser based control of the stage 6 delay is therefore envisaged for minimizing pulse-to-pulse interference.

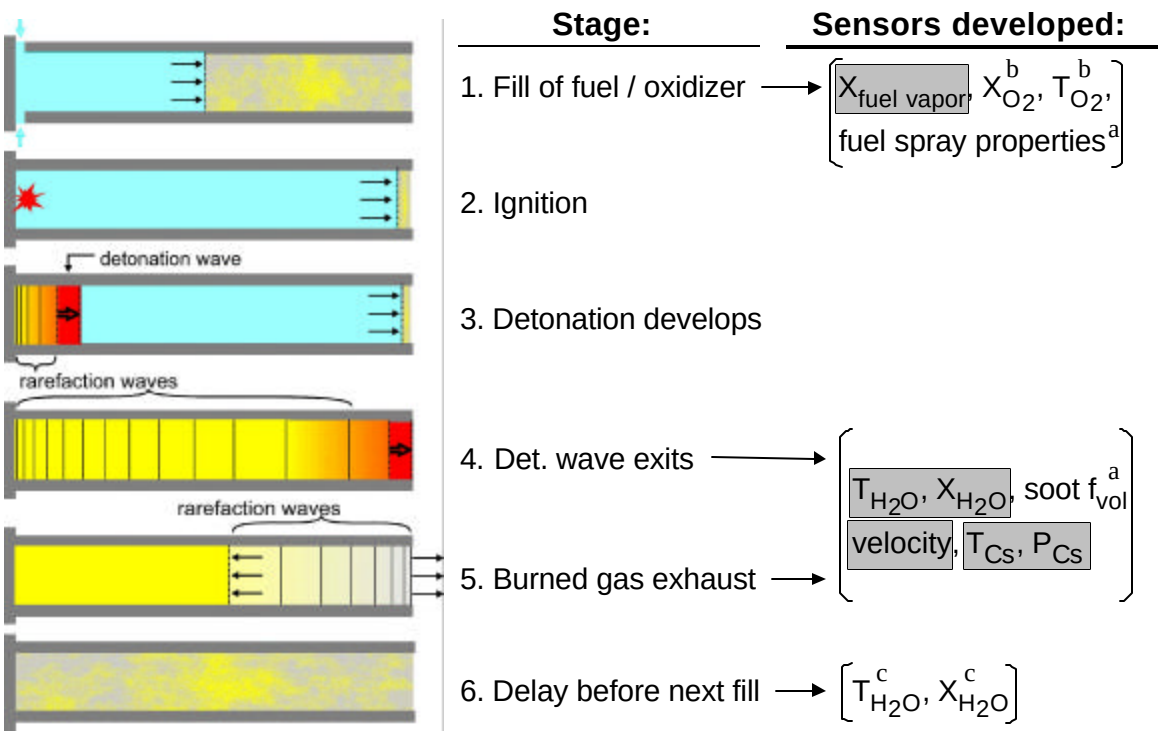

Figure 2.1. Stage-by-stage chronology of PDE cycle, indicating sensors applied for PDE development, control, and model validation. Gray shaded sensors are discussed in Chapter 3 of this thesis, others are detailed elsewhere: a = (Sanders et al. 2000a); b = (Sanders et al. 2000b); c = (Sanders et al. 2001c).

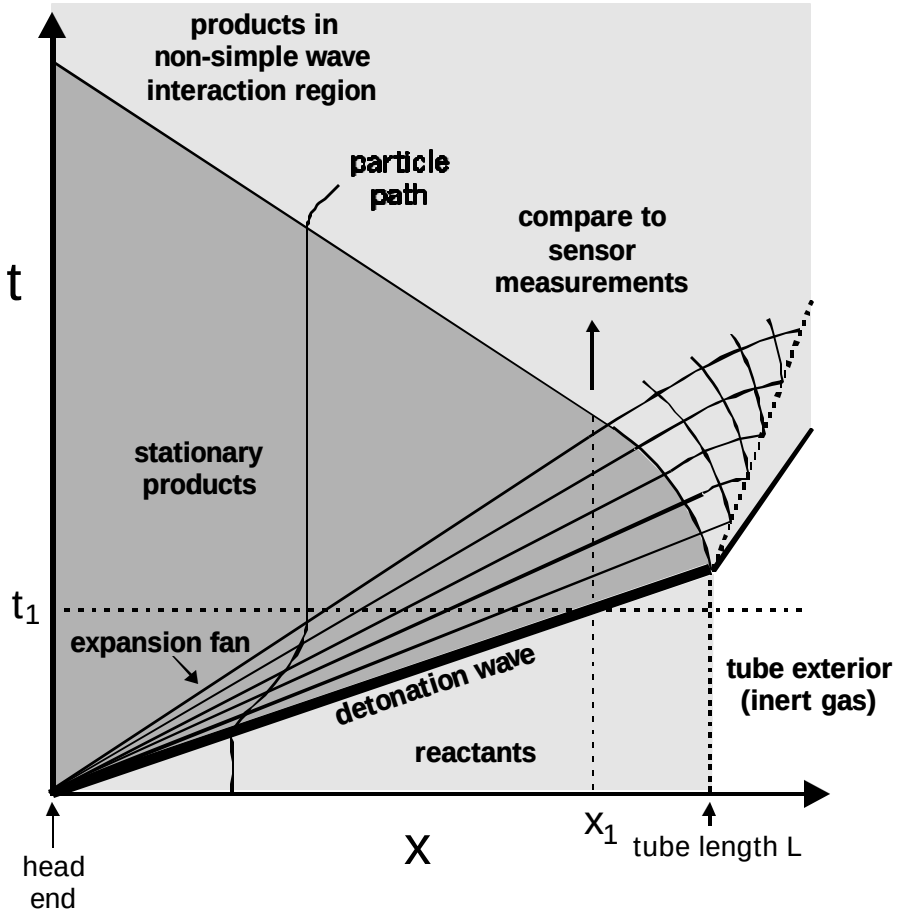

Figure 2.2. Simplified x-t diagram of an idealized detonation event.

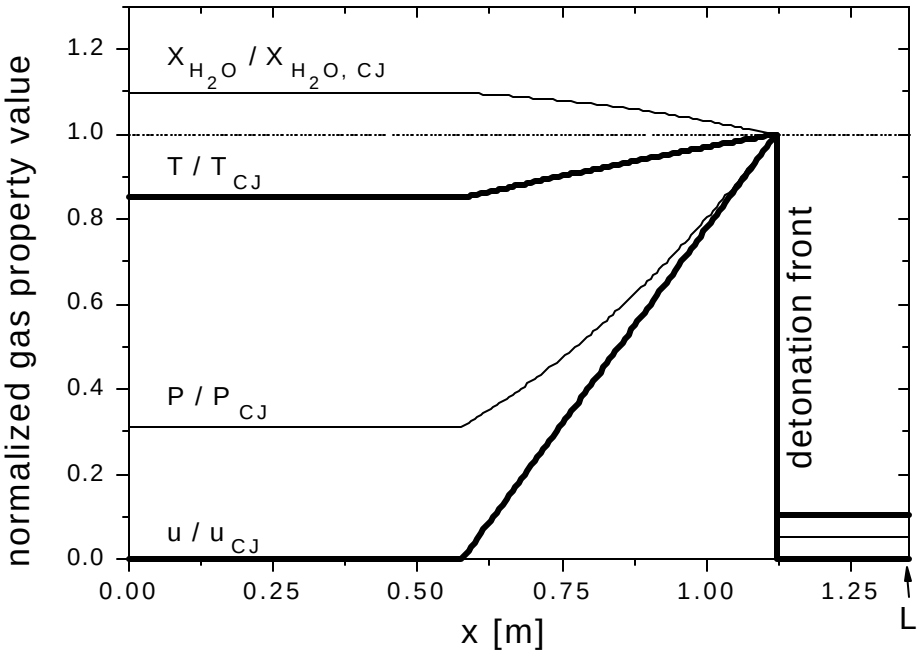

Figure 2.3. Sample gas properties calculated using the method of characteristics for a slice along time t_1 in Fig. 2.2. Properties are calculated for detonation of stoichiometric C_2H_4 / air and are normalized by their Chapman-Jouget values: $X_{H2O,C\text{-}J} = 0.1123$, $T_{C\text{-}J} = 2927$ K, $P_{C\text{-}J} = 18.36$ atm, and $u_{C\text{-}J} = 818$ m/s.

Chapter 3

Sensors applied for PDE development, control, and model validation

1. Introduction

In Chapter 2, the diagnostics needs that have been fulfilled by diode laser sensors were outlined using Fig. 2.1. In this chapter, select sensors highlighted in Fig. 2.1 will be detailed. All of the sensors discussed below use either wavelength multiplexing or broad wavelength scanning to enable accurate measurements in the harsh PDE environment, except the burned gas velocity sensor (section 3.4). The velocity sensor represents a rare case where signals are so strong and the data interpretation so unambiguous that advanced sensing techniques are not needed.

2. Stage 1 fuel vapor sensor for PDE development and control: broad wavelength scanning

Ethylene (C_2H_4) fuel has been used frequently in initial PDE studies, owing primarily to its detonability and ease of delivery to laboratory engines (relative to liquid fuels). In addition, because liquid fuels envisaged for practical PDEs are expected to pyrolize to ethylene or ethylene-like species prior to detonation events, an understanding

of ethylene detonations is desired. Although ethylene has been readily measured at low pressures using diode laser sensors (Mihalcea et al. 1998), measurements at and above atmospheric pressure are not trivial.

Survey spectra of C_2H_4 in the 2800–14500 cm^{-1} range have been recorded in the literature (Brock et al. 1994). Because C_2H_4 is larger than traditional molecules targeted by diode lasers, its absorption features are almost always blended, resembling the high-pressure O_2 spectrum shown in Fig. 1.4. A handful of nearly-isolated transitions are available, however (notably the low-J lines in the R-branch of the $\nu_5+\nu_9$ combination band near 1.62 μm; see Georges et al. 1997). Although appropriate for monitoring cold or room-temperature ethylene (Sanders et al. 2001c), these lines are not useful in combustion applications where hot ethylene is of interest; their linestrengths decay to the level of interfering C_2H_4 (hot) lines at approximately 600 K, disabling measurements near or above this temperature. An alternative strategy is therefore needed for monitoring ethylene in PDEs.

The Q-branch of the $\nu_5+\nu_9$ combination band provides the solution: its strength is high over a broad range of temperatures and it is isolated from (much stronger than) nearby P- and R-branch features. However, it is spectrally broad, requiring an 8 cm^{-1} scan to record the feature using traditional scan-wavelength techniques, and traditional DFB lasers offer only about 2 cm^{-1} injection-current tuning. The requisite 8 cm^{-1} scans were achieved by obtaining a DFB laser with an uncommonly high series resistance (greater series resistance enables enhanced current-tuning as discussed in section 4.2) and exceeding the maximum recommended current by 40% during the injection-current scan.

An *in-situ*, single-sweep (in 1 ms) measurement of the $\nu_5+\nu_9$ Q-branch obtained in this way is shown in Fig. 3.1. Kilohertz-rate scans over this feature provide real-time, quantitative measurements of C_2H_4 mole fraction during PDE fills simply from the feature area (at T = 296 K, $X_{C2H4} = 2.276 \times \text{Area}[\text{cm}^{-1}] / L[\text{cm}]$). C_2H_4 temperature records can be obtained simultaneously if the shape of this feature is also analyzed.

The Q-branch-based ethylene mole fraction sensor has been applied simultaneously to the head and tail ends of the Stanford PDE, as shown schematically in Fig. 3.2. When the fuel / oxidizer input flow rates are controlled and well-behaved, measurements at these two locations are usually sufficient to understand the fuel / oxidizer distribution in the engine at the time of ignition; however, more measurement stations can readily be added using additional beamsplitters and detectors if necessary.

Sample data recorded at the tail measurement station for consecutive C_2H_4 / O_2 engine fills, one with and one without ignition, are shown in Fig. 3.3. A wealth of information can be obtained from such data. For instance, the rise of the fuel concentration is not instantaneous, owing to finite valve opening time and diffusion processes. This feature translates spatially into a slug of flow containing a nonuniform fuel concentration. If one desires to fill the engine with a uniform fuel distribution before firing, the nonuniform slug must be loaded beyond the tail end of the engine, resulting in wasted fuel. If one desires to waste no fuel, the nonuniform slug must remain in the engine, which may be undesirable. In many cases, one wishes to minimize the fuel concentration rise time seen in Fig. 3.3, and the sensor is of obvious utility for this task. The sensor is also useful for optimizing or controlling ignition timing. In the case shown

in Fig. 3.3, ignition occurs after a uniform charge has been established in the engine, resulting in wasted fuel.

The absolute uncertainty in the X_{C2H4} data shown in Fig. 3.3 is estimated at ±3%. Because it employs rapid, broad wavelength-scanning, the accuracy of the ethylene sensor is not impaired by any of the sensing challenges listed in Table 1.1; this immunity is demonstrated by the low noise level in the Fig. 3.3 data immediately after the detonation wave arrival at 510 ms. The sensor's accuracy is critical whenever the equivalence ratio of a PDE charge must be known or controlled.

3. Stage 4/5 T_{gas}, X_{H2O} sensor for model validation: wavelength multiplexing

Histories of gas properties such as temperature and H_2O concentration facilitate detailed validations of detonation models. When coupled with gas velocity measurements (such as presented in section 3.4) and standard pressure transducer measurements (such as presented in section 3.6), these histories provide a thorough metric with which to evaluate and improve PDE models.

A five-wavelength diagnostic used to measure H_2O temperature and mole fraction in PDE flows is shown in Fig. 3.4, applied to the Stanford PDE. An additional account of this sensor is available in the literature (Sanders et al. 2000a). Each of the five distributed feedback (DFB) diode lasers is typically operated at fixed wavelength. The wavelengths are carefully chosen, using simulated spectra such as those shown in Fig. 3.5. Three

wavelengths (λ_1, λ_2, and λ_3) target H_2O absorption features, and two (λ_{nr1} and λ_{nr2}; "nr" denotes nonresonant) track transmission losses due to the multiplicative noise sources (window birefringence, extinction, window fouling, beamsteering, and mechanical vibration) listed in Table 1.1. Although two H_2O wavelengths are typically sufficient for T_{H2O} and X_{H2O} measurements (Baer et al. 1996), three H_2O wavelengths are needed in this case to maintain temperature sensitivity over the relatively wide temperature range of interest (typically 900–3300K in airbreathing PDEs): the ratio of absorbances at λ_1 and λ_2 is sufficiently temperature-sensitive over the 900–2000 K range, and the ratio of absorbances at λ_1 and λ_3 over the 2000–3300 K range. Once gas temperature has been determined from the appropriate absorbance ratio, H_2O mole fraction is readily determined using an independent measurement of pressure and the measured absorbance at a selected wavelength.

The relative drawbacks of wavelength multiplexing, discussed in section 1.5, have repercussions for this sensor. First, because information is obtained only at one spectral location near each of λ_1, λ_2, and λ_3, the data reduction requires full details of the collisional broadening parameters for the contributing transitions near λ_1, λ_2, and λ_3 as a function of temperature. Although occasionally available in the literature (e.g., Nagali et al. 1997), such data are generally unknown, and therefore fixed-wavelength measurements of absorption coefficients, such as shown in Fig. 3.6, are needed to gain a rough understanding of the collisional broadening parameters (Sanders et al. 2000c). Second, because information is obtained only at two select nonresonant wavelengths, the subtraction of multiplicative transmission noise (due to window birefringence, extinction,

window fouling, beamsteering, and mechanical vibration) from raw transmission data must be based on an assumed wavelength-dependence of these noise sources (Sanders et al. 2000a). In the end, the wavelength multiplexing strategy, with its relatively limited spectral information, will generally provide less accurate results than the broad wavelength scanning strategy. However, the results can be made sufficiently accurate by multiplexing additional wavelengths or by eliminating noise sources using the specialty solutions listed in Table 1.1. The latter approach was applied in this five-wavelength sensor; beamsteering was eliminated using the optical collection system shown in Fig. 3.4 and detailed in Appendix A, and mechanical vibration effects were minimized by stiffening optical fibers and shielding optics from detonation blasts. The resulting uncertainties in T_{H2O} and X_{H2O} are typically ±10%.

Sample gas temperature and H_2O mole fraction histories recorded in the Stanford PDE using the Fig. 3.4 sensor are shown in Fig. 3.7. The measurements are compared to a method of characteristics calculation (see section 2.3) and an NRL simulation (section 2.4). General agreement between the measurements and both calculations is observed. However, the measured temperature deviates from the calculations at long times, possibly because heat transfer is neglected in both calculations. The two *calculations* disagree substantially in the X_{H2O} plot; the NRL simulation freezes the species concentrations at their Chapman-Jouget values, whereas the method of characteristics solution computes equilibrium species concentrations (which provide for increased H_2O mole fraction as the temperature decreases).

4. Stage 4/5 Cs-based u_{gas} sensor for model validation

Gas velocity histories recorded near the tail end of a PDE are especially sensitive to the PDE exit boundary condition. Modelers therefore desire gas velocity histories to validate their numerical PDE exit boundary condition, particularly in one-dimensional calculations where no simple exit boundary condition can be assumed *a priori* (Li et al. 2000); this is in contrast to the head end where a simple zero-velocity boundary condition is enforced by the head end wall. Because of the same sensitivity, experimentalists can also use gas velocity histories to ascertain the effects of experimental features such as PDE exit diaphragms used to create controlled PDE charges. Gas velocity histories are expected to be increasingly useful to modelers and experimentalists alike as emphasis shifts from straight tubes (useful for fundamental studies) to PDEs with nozzles and internal features (useful for practical applications).

The PDE is a challenging environment in which to measure gas velocity. High pressures disable traditional Doppler-shift-based absorption measurements (e.g., Wehe et al. 1999) because the large collisional width of an absorption transition obscures the relatively small Doppler shift produced by practical velocities. To remedy this problem, Doppler-shift velocimetry based on Rayleigh scattering has been considered; the Rayleigh-scattered linewidth is not broadened significantly by collisions (see Seasholtz et al. 1997) because Heisenberg broadening associated with absorber energy levels is

removed. However, the weak Rayleigh scattering signal, coupled with the fast time response needed to resolve PDE events, is expected to yield noisy velocity measurements. Therefore, Doppler-shift velocimetry based on Mie scattering (possibly from nascent soot but more likely from seeded particulate) has been considered. Although this strategy should be effective, the complexities of the seeding system and the optical system required to accurately quantify Doppler shifts encouraged us to develop an alternative strategy.

The novel sensor developed for measuring gas velocity (see also Sanders et al. 2001e) in PDE flows is shown in Fig. 3.8. Gas velocity is inferred by measuring the time-of-flight of seeded atomic Cesium vapor over a known distance. The sensor employs a single diode laser, fixed to the $6^2P_{3/2} \leftarrow 6^2S_{1/2}$ D_2 resonance transition of atomic Cs near 852 nm. A collimating lens (not shown) collects the output from the diode, focussing it slightly so the beam reaches a diameter of approximately 200 μm at the center of the PDE. The beam is split so that two beams, separated by 2 mm, are directed through the flow. The transmitted intensity of each beam is monitored independently by Si photodiodes.

Upstream of the probe beams, a stainless steel needle is held in the center of the PDE by an aerodynamically-shaped cross member having a 1.9 mm × 6.2 mm cross-section. The 150 μm diameter needle tip is located approximately 2 cm upstream of the probe beams. Saturated CsCl saltwater is periodically applied to the needle tip. During an engine cycle, the detonation wave travels over the needle and CsCl is entrained into

the burned gases that follow. As they rapidly equilibrate to the local burned gas temperature, the CsCl molecules dissociate to give a significant fraction of Cs atoms.

Sample transmission traces from each detector are shown in Fig. 3.9. The intense structure in both signals is due to unsteady Cs seeding; the needle emits "pulses" of Cs rather than a continuous, uniform Cs stream. As discussed in Appendix B, the details of the seeding mechanics are responsible for the formation of Cs pulses. The natural formation of Cs structure in the flow presents an opportunity to measure velocity simply by measuring the beam-to-beam time delay in the structure signature. Note that the downstream signal is essentially a time-delayed version of the upstream signal; from the time-of-flight, gas velocity is inferred. Using a one-dimensional cross-correlation, the time delay for a transmission data excerpt (such as the one shown in Fig. 3.9) is determined. The uncertainty in the beam locations and deviations from pure axial translation of cesium structures render such velocity measurements accurate to approximately 5%. Repeating the cross-correlation for each data excerpt, an entire velocity-versus-time history, such as the one shown in Fig. 3.10, can be obtained. Because the sensor measures the PDE centerline velocity, owing to the local Cs seeding, it is sensitive to local velocity fluctuations. To de-emphasize these fluctuations and reveal the centerline velocity trend, the measurement shown in Fig. 3.10 was generated by averaging three sequentially-recorded velocity histories.

The Fig. 3.10 measurements are compared to a simulation performed by the Naval Research Laboratory (NRL). Excellent agreement is observed up until the time that the tail-to-head travelling rarefaction arrives at the test station (this time corresponds to the

beginning of the non-simple wave interaction region labeled in Fig. 2.2). After this time, disagreements in timing and magnitude emerge, most notably near 5 ms where a dramatic drop in the measured velocity begins about 1 ms before the corresponding drop in the calculated velocity. Analysis of such disagreements can be used as a check on experimental procedures as well as a guide for evaluating models.

Compared to other available velocimetry techniques, the sensor has several advantages that make it especially well suited to PDEs. The sensor is rugged and simple; because the Cs absorption signal is very strong, neither wavelength multiplexing nor broad wavelength scanning are required to enable quantitative measurements. The sensor provides continuous gas velocity histories with fast time response in arbitrarily high pressure environments. The raw data can be rapidly reduced to unambiguous results because of the time-of-flight strategy. While not suitable for complex, multidimensional flows, time-of-flight velocimetry is appropriate for this well-behaved, one-dimensional flow.

The major disadvantage of the sensor is the need for an intrusive sting; however, practical PDEs often have internal features (e.g., to enhance detonation initiation) which could possibly be used as seeding surfaces. Furthermore, other atomic tracers could be used for velocimetry in practical engines, provided the tracer is not native to the engine (potentially generating unwanted "background" seeding) and the tracer is not consumed in the temperature range of interest (below about 1200 K, for example, Cs forms CsOH so readily that only 0.0001% of the seeded Cs will remain in atomic form, thus disabling Cs-based velocimetry).

5. Stage 4/5 Cs-based T_{gas} sensor for model validation: broad wavelength scanning

The H_2O-based temperature measurements described above in section 3.3 suffer from two shortcomings. First, because they are wavelength-multiplexed, they are inherently less robust and accurate than wavelength-scanning techniques, as detailed in section 3.3. Second, when PDE temperatures become high (> 3000 K), the H_2O absorbance becomes increasingly weak due to partition function (more rotational and vibrational states populated means less population in any one state), number density (decreases as 1/T), and chemical equilibrium (H_2O dissociates to OH, H, and O) effects.

A scan-wavelength temperature sensor based on Cesium absorption offers solutions to both of these problems. VCSELs, detailed in section 4.2, offer the rapid, broad wavelength tunability (~ 1 nm / μs) required to scan over high-pressure Cs absorption features, and they are readily available near the 852 nm D_2 resonance transition. Atomic Cs is a strong absorber at all temperatures (relevant to combustion), primarily because its partition function is freed of rotational and vibrational components.

For gas temperature measurements, the Cs-seeding approach detailed in section 3.4 is not favorable. The intense natural modulation of the Cs concentration that enabled velocity measurements undermines the continuity and accuracy of temperature measurements. Roughly-uniform Cs seeding is desirable, and can in fact be accomplished using the approach depicted in Fig. 3.11. In addition to the C_2H_4 and O_2

fill tanks, a heated tank containing Cs metal and high pressure Ar supplies the mixing tee near the PDE head end. During an engine fill, when all three supply-line valves are opened, a relatively weak Ar flow (containing trace Cs vapor) is mixed with the C_2H_4 / O_2 fill gases. The Cs immediately forms CsO particulate in the mixing tee, where O_2 is present. Thus the charge that fills the PDE contains a trace of CsO dust. The temperature of the Cs tank (and its mixing tee supply line) can be adjusted to optimize the Cs seeding fraction (in this case ~ 5 ppm was achieved at a temperature of ~ 500 K). Cesium is the easiest alkali metal to seed in this way because it has the lowest melting point (and the highest vapor pressure at any given temperature). Cesium metal is typically supplied in glass ampules which must be broken inside the tank while under Ar purge. The tank, valves, and supply line must be made of inert materials; we found that stainless steel components with teflon seals were acceptable. In liquid-fueled PDEs, a simpler seeding strategy is available; Cs can be added to the fuel in the tank (e.g., as CsCl salt) to generate a rougly-uniform Cs concentration in the charge. Unlike the locally-seeded PDE discussed in section 3.4, the uniformly-seeded PDE provides nonintrusive, line-of-sight averaged measurements.

The temperature sensor shown in Fig. 3.11 uses a single, rapidly-scanning VCSEL near 852 nm and two detectors. As a detonation wave passes the measurement station, detector 1 monitors Cs absorption lineshapes; raw data is shown in Fig. 3.12. Detector 2 simultaneously monitors 852 nm Cs emission from the same volume probed by the VCSEL beam; raw data is shown in Fig. 3.13. Two different Cs vapor temperatures, an electronic temperature and a kinetic temperature, can be obtained from

this sensor; these are expected to be equal because the electronic excitation time constant for typical PDE conditions is < 1 μs (see Teulet 1998, Teulet et al. 2001). The electronic temperature, $T_{Cs,\ electronic}$, is obtained from the ratio of the Cs population in the excited electronic state ($6^2P_{3/2}$, given by detector 2) to the Cs population in the ground electronic state ($6^2S_{1/2}$, given by the integrated absorbance areas of the lineshapes recorded by detector 1: $n_{Cs,6^2S_{1/2}}[cm^{-3}] = 3.2\times10^{12} \times \text{Area}[cm^{-1}] / L[cm]$). The kinetic temperature, $T_{Cs,\ kinetic}$, is obtained from the collisional width in the detector 1 lineshapes, $\Delta\nu_c$, governed by

$$\Delta\nu_C = 2\gamma \cdot P; \quad \gamma = \gamma_o\left(\frac{T_{Cs,kinetic}}{T_o}\right)^n, \qquad \text{(eq. 3.1)}$$

where γ (= $\gamma_{Cs\text{-detonation products}}$) is the overall collisional broadening parameter, P is the pressure (typically measured by a wall-mounted transducer), T_o is the reference temperature (300 K in this thesis), γ_o is the value of γ at temperature T_o, and n is the broadening temperature exponent. Thus, with measurements of $\Delta\nu_c$ and P (and thus of γ), $T_{Cs,\ kinetic}$ can be obtained from eq. 3.1, provided γ_o and n are known.

Given the data shown in Figs. 3.12 and 3.13, the first step in obtaining either temperature is to fit the Fig. 3.12 data as illustrated in Fig. 3.14. The data shown in Fig. 3.14 corresponds to the Cs absorption feature obtained immediately after detonation wave passage; the high pressure accounts for the large collisional width and shift relative to the hyperfine structure, provided for reference in Fig. 3.14. Even though the hyperfine structure contains 6 individual transitions (see the energy level diagram in Fig. 3.14), the small upper-state splittings can be neglected for our purposes here. Thus, a two-line

Voigt profile is fit to the data. An arbitrary two-line Voigt fit would have 8 total free parameters: two each of (area, $\Delta\nu_c$, Doppler width $\Delta\nu_D$, and position ν_o). However, in this case (partly because of Cesium's high molecular weight and partly because of the high gas pressures existing during much of the detonation experiment), fixing both $\Delta\nu_D$ values to 0.03266 cm^{-1} (their values at the lowest expected temperature of 2000 K) introduces negligible errors. Also, the ratio of the two areas is fixed at 9/7 (given by hyperfine calculations), the line separation $\Delta\nu_o$ is fixed at 9192 MHz = 0.3064 cm^{-1}, and the two $\Delta\nu_c$ are assumed equal. Thus, 5 of the 8 free parameters have been removed; the two-line Voigt fit now returns only three parameters: area, $\Delta\nu_c$, and ν_o. The area is used to obtain $T_{Cs,\ electronic}$, $\Delta\nu_c$ is used to obtain $T_{Cs,\ kinetic}$, and ν_o is not used. Note that ν_o contains pressure-shift information; like $\Delta\nu_c$, such information is pressure- and temperature-dependent, and therefore could be incorporated in future sensors. Histories of area and $\Delta\nu_c$ obtained by repeated application of the two-line Voigt fit during a 7 ms detonation experiment (3709 total scans) are shown in Fig. 3.15.

Incidentally, the area can also be used to infer the Cs vapor mole fraction (44 ppb for the scan shown in Fig. 3.14). In this experiment, the measured Cs vapor mole fraction is always much less than the Cs seeding fraction (5 ppm; see Fig. 3.11) because the majority of the Cs is present as either CsOH or Cs^+ (the former at temperatures below ~ 2600 K and the latter at temperatures above ~ 2600 K). The ionization to Cs^+ at high temperatures is actually convenient for emission measurements because it limits the required dynamic range (if Cs^+ were not favored at 4000 K, the emission would be some 10000 × the emission at 2000 K, rather than the ~ 50 × seen in Fig. 3.13).

By comparing the ratio of the measured emission (Fig. 3.13) to the measured area (Fig. 3.15) with the Boltzmann distribution, $T_{Cs,\ electronic}$ can be readily determined. However, because the emission measurement is not absolute, the $T_{Cs,\ electronic}$ history requires calibration; conveniently, in this well-controlled detonation experiment, the first $T_{Cs,\ electronic}$ data point can be fixed to the Chapman-Jouget temperature. The resulting electronic temperature history is shown in Fig. 3.16. Note that in less-controlled detonation experiments (particularly in practical PDEs) it may not be appropriate to calibrate the $T_{Cs,\ electronic}$ sensor using the Chapman-Jouget value; in many instances one may wish to *measure* whether individual detonations reach the Chapman-Jouget temperature. The $T_{Cs,\ kinetic}$ sensor, discussed below, is suitable for this purpose.

Knowing both $T_{Cs,\ electronic}$ and pressure (from a wall-mounted transducer; see Fig. 3.19), the corresponding equilibrium species concentration histories can be computed, as shown in Fig. 3.17. Note that the gas composition changes dramatically during this detonation experiment (assuming equilibrium chemistry is obeyed), and with it the ratio of specific heats, k (indicated in Fig. 3.17). The NRL simulation's assumption of constant gas composition and k (fixed at the Chapman-Jouget values) may be responsible for the absolute temperature disagreements of up to 14% in Fig. 3.16. The uncertainty in the $T_{Cs,\ electronic}$ measurement is estimated at ± 5%.

To determine $T_{Cs,\ kinetic}$ from the $\Delta\nu_c$ record shown in Fig. 3.15, we first divide $\Delta\nu_c$ by $2\times$ P to obtain γ (following eq. 3.1). Next, best-fit values of the parameters n (–2.02) and γ_o (9.48 cm^{-1}/atm) and are found using $T_{Cs,\ electronic}$ as the temperature standard, as shown in Fig. 3.18. Although such data are scarce in the literature, these values might be compared with an estimation of n = –1.38 and γ_o = 0.68 for N_2-broadened potassium

(Wehe, 2000). The large discrepancy in γ_o values is reconciled by a finding that sodium's D_2 line is broadened much more severely by H_2O than N_2 ($\gamma_{Na\text{-}H2O,2000K} \approx \gamma_{Na\text{-}N2,500K}$; see Nefedov et al. 1999). Note that direct measurement of room-temperature γ_o values for atomic alkalis broadened by species such as H_2O and CO_2 are impossible because of the extreme reactivity of these gases. Returning to the linear fit in Fig. 3.18, the curvature of the data at high temperatures indicates that a single γ_o and n are somewhat inappropriate over the full temperature range, presumably because of the changing gas composition shown in Fig. 3.17. A composition-dependent fit is applied to capture this curvature. The linear fit is applicable over the 2000–3200 K temperature range; the composition-dependent fit is applicable over the full temperature range. Neither fit is intended to provide fundamentally accurate spectroscopic data; rather, the fits are designed to enable $\Delta\nu_c$-based temperature measurements over a limited temperature range and for a specific gas composition (namely, one approximating the equilibrium products of C_2H_4/O_2). Further work is required to extend the kinetic temperature measurement technique presented here to other gas compositions or temperature ranges.

Using the composition-dependent fit shown in Fig. 3.18, the measured γ values plotted in Fig. 3.18 can be converted to the $T_{Cs,\ kinetic}$ record shown in Fig. 3.16. The uncertainty in $T_{Cs,\ kinetic}$ is estimated at $\pm$ 7%. The fit performed in Fig. 3.18 forces the two temperature records plotted in Fig. 3.16 to agree (to the extent that the composition-dependent fit matches the Fig. 3.18 data). Even so, the agreement represents a critical advancement, because now detector 2 can be removed from the Fig. 3.11 setup and temperature measurements based on *absorption only* can be performed. Furthermore, the absorption-based ($\Delta\nu_c$-based) measurements are absolute; the single-laser, single-detector

sensor can be used without calibration to obtain gas temperature in any Cs-seeded, C_2H_4/O_2 combustor (using an auxiliary pressure measurement). Alternatively, detector 2 can be retained to enable $T_{Cs,\ electronic}$ measurements (again requiring calibration) and the $\Delta\nu_c$ records and composition-dependent fit can be used to obtain gas pressure rather than $T_{Cs,\ kinetic}$; this is demonstrated in Fig. 3.19. The spectroscopic pressure measurement agrees well with the transducer measurement, up until $t \approx 5$ ms. The transducer measurement is in error after this time, presumably because it has poor low-pressure accuracy, especially in the moments immediately following a high-pressure transient. Because of unreliable transducer measurements, data after $t \approx 5$ ms has been omitted from the Fig. 3.16 $T_{Cs,\ kinetic}$ plot and the Fig. 3.18 fit. The measured pressures agree reasonably well with the simulated pressures; notable disagreements include the time of the onset of the pressure plateau and the absolute pressure values during the plateau.

6. Summary of model comparisons

Figure 3.20 summarizes the measured and simulated gas properties for detonation of stoichiometric C_2H_4 / O_2. In general, the plots agree well, with several exceptions in timing and magnitude. The details of these exceptions should be useful for advancing PDE modeling efforts, with the ultimate goal of PDE models which are capable of rapidly and accurately predicting the performance of an arbitrary PDE. Presently, it is believed that updating the simulation to account for the gas composition and k variations shown in Fig. 3.17 will greatly improve the agreement in Fig. 3.20.

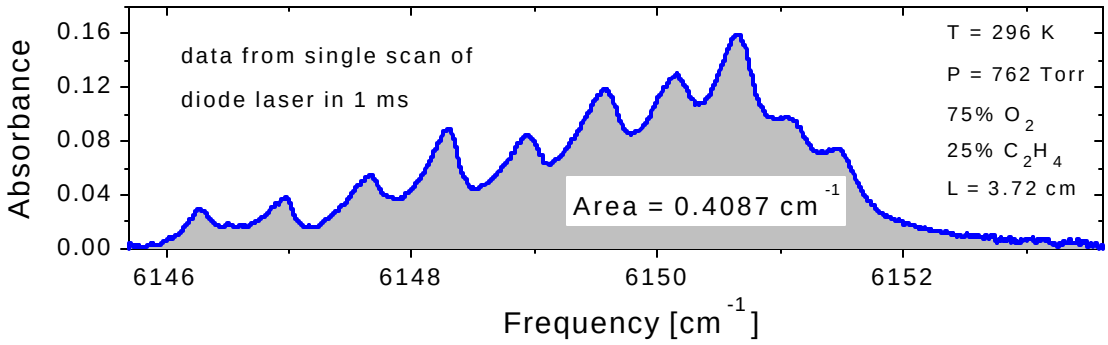

Figure 3.1. Single-sweep measurement of the $\nu_5+\nu_9$ combination band Q-branch of C_2H_4, for PDE conditions corresponding to stoichiometric C_2H_4 / O_2. Using such measurements, X_{C2H4} histories such as the one shown in Fig. 3.3 can be obtained simply by monitoring the feature area (at T = 296 K, $X_{C2H4} = 2.276 \times \text{Area}[\text{cm}^{-1}] / \text{L}[\text{cm}]$).

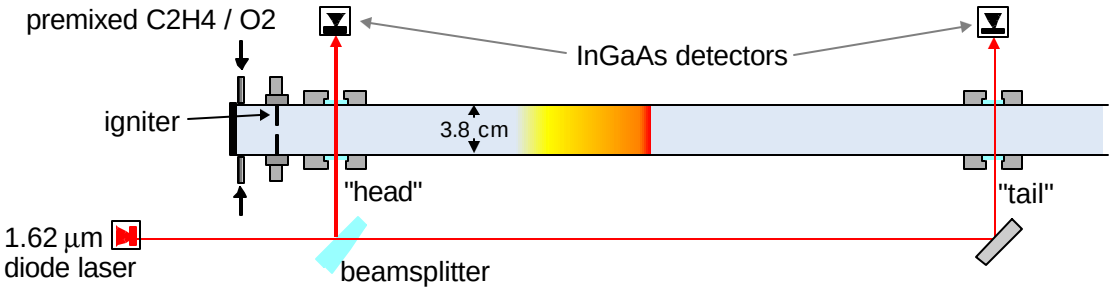

Figure 3.2. Schematic of Stanford PDE with diode-laser sensor applied to monitor C_2H_4 concentration near the head and tail ends.

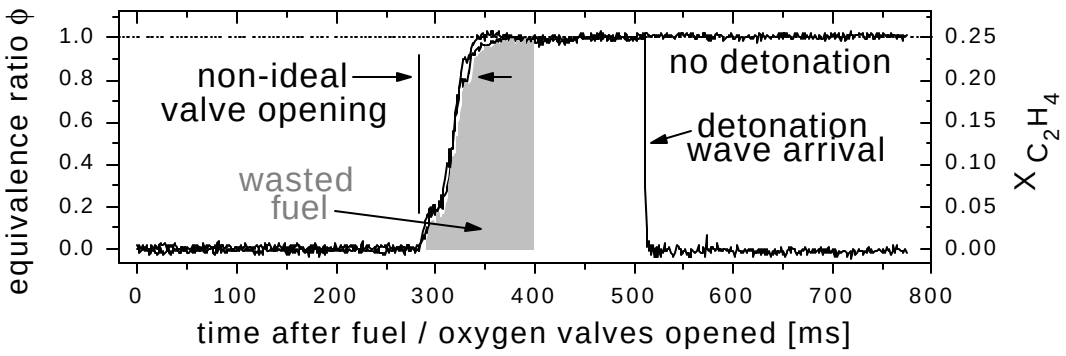

Figure 3.3. Sample C_2H_4 concentration data recorded at the tail measurement station (shown in Fig 3.2) for cases with and without ignition. A wealth of system information, such as the finite X_{C2H4} rise time (due to non-ideal valving and diffusion) can be inferred from such records.

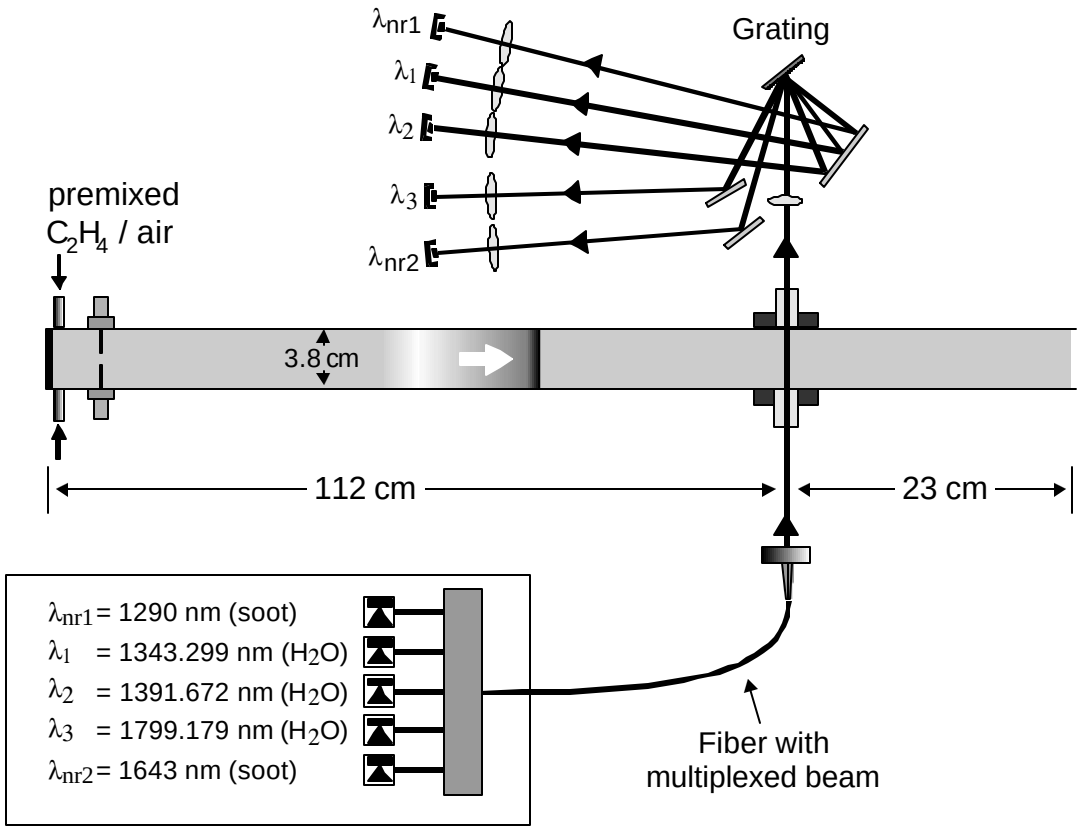

Figure 3.4. Five-wavelength-multiplexed diode-laser sensor for measuring T_{gas} and X_{H2O} in detonation flows.

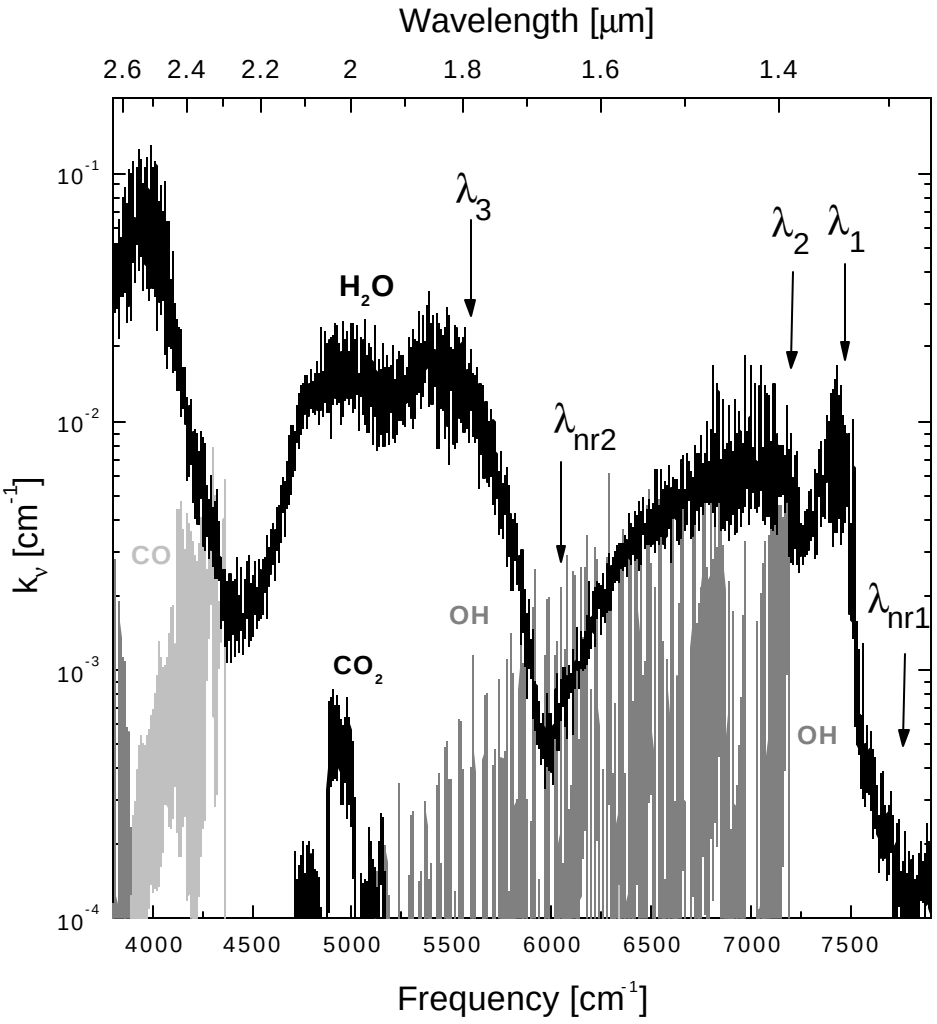

Figure 3.5. Calculated absorption spectra for equilibrium products of stoichiometric JP-10 / O_2 at representative PDE conditions of 3000 K and 15 atm. H_2O spectrum is calculated using the HITEMP database; remaining spectra are calculated using the HITRAN database.

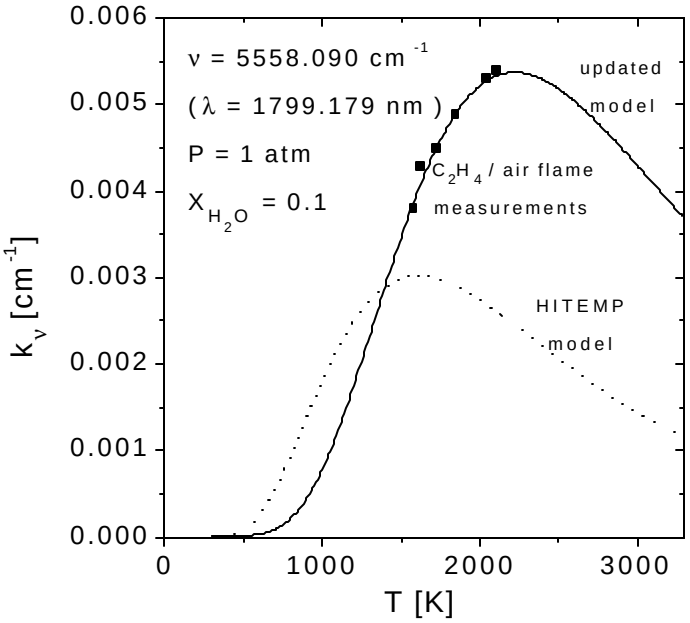

Figure 3.6. Black squares are measurements of the spectral absorption coefficient k_ν at the fixed wavelength of 1799.179 nm in a C_2H_4 / air flame. Because these measurements disagree with the HITEMP model, an updated model (see Sanders et al. 2000c), employing modified line positions, line strengths, lower state energies, and broadening coefficients, has been developed.

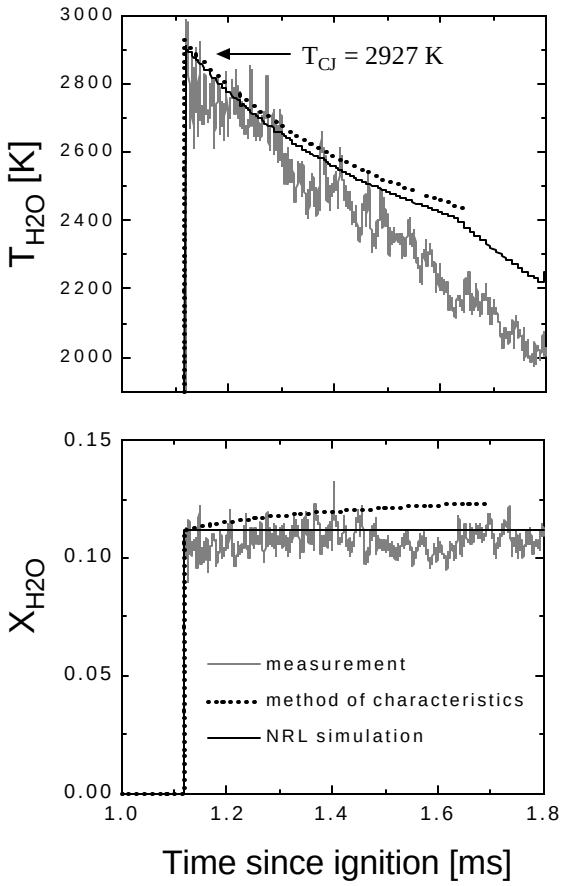

Figure 3.7. Sample gas temperature and H_2O mole fraction histories recorded in the Stanford PDE (relevant dimensions are provided in Fig. 3.4.) for detonation of stoichiometric C_2H_4 / air. The method of characteristics solution terminates near 1.7 ms when the non-simple wave interaction region (indicated in Fig. 2.2) is reached.

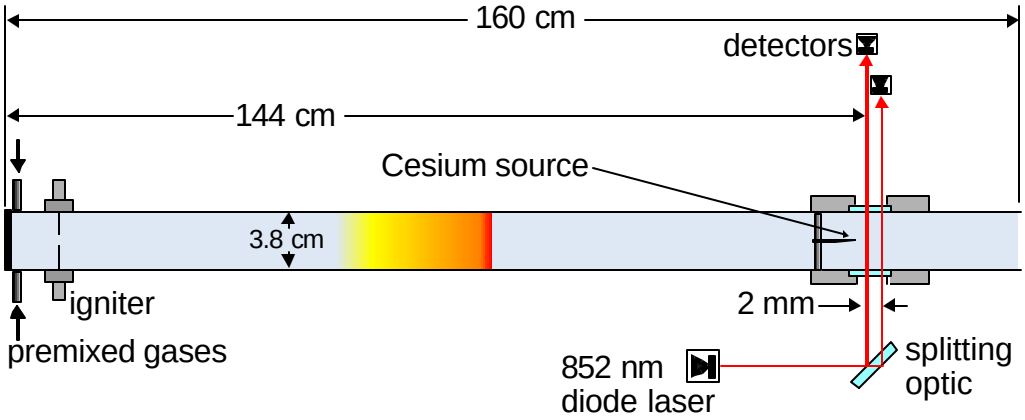

Figure 3.8. Schematic diagram of PDE gas velocity sensor. A stainless steel needle is held in the center of the PDE by an aerodynamically-shaped member having a 1.9 mm × 6.2 mm cross-section. CsCl salt is applied to the 150 μm diameter needle tip. Each diode laser beam is focused near the center of the PDE to a spot size of approximately 200 μm.

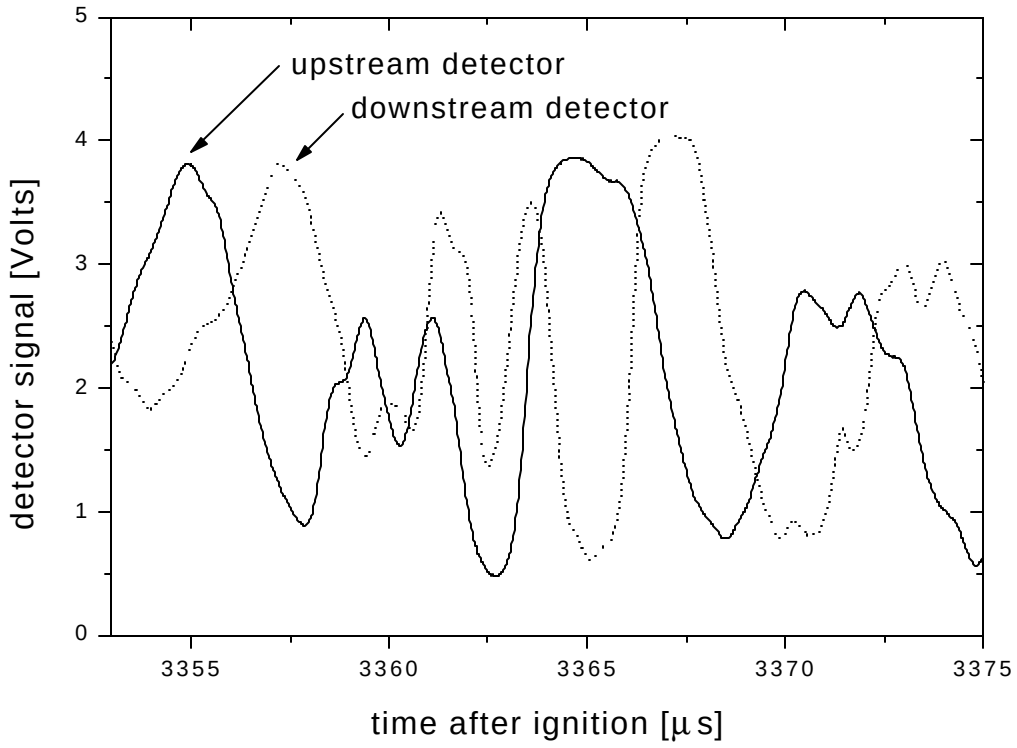

Figure 3.9. Sample raw transmitted intensity data recorded by each detector shown in Fig. 3.8 while burned gas is flowing at a measured velocity of 855 m/s. The signal at the downstream detector is essentially a delayed version of the signal at the upstream detector. The gas velocity in the PDE is inferred from the delay, using the known axial offset between the two probe beams.

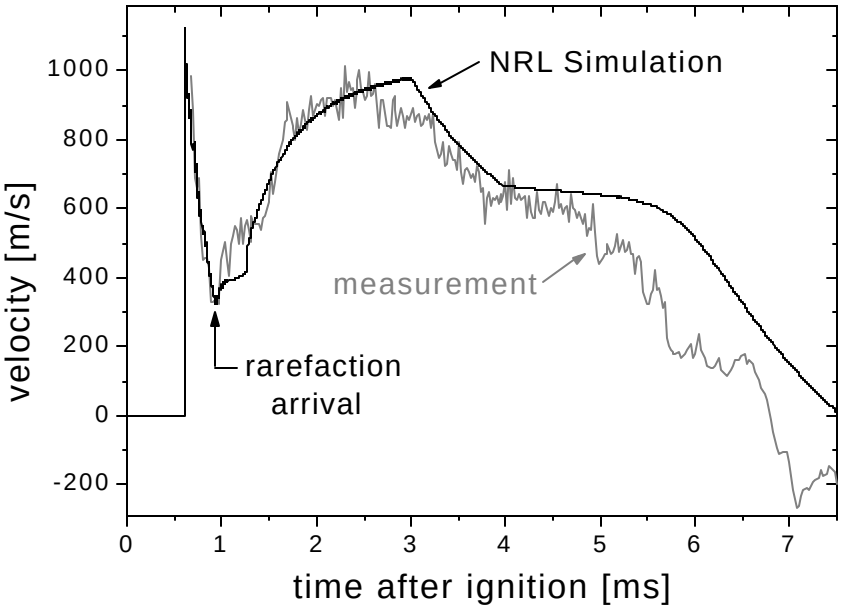

Figure 3.10. Burned gas velocity histories (measured and computed) for detonation of stoichiometric C_2H_4 / O_2 (relevant dimensions are provided in Fig. 3.8). Individual velocity data points are inferred from subsets of raw data such as the one shown in Fig. 3.9.

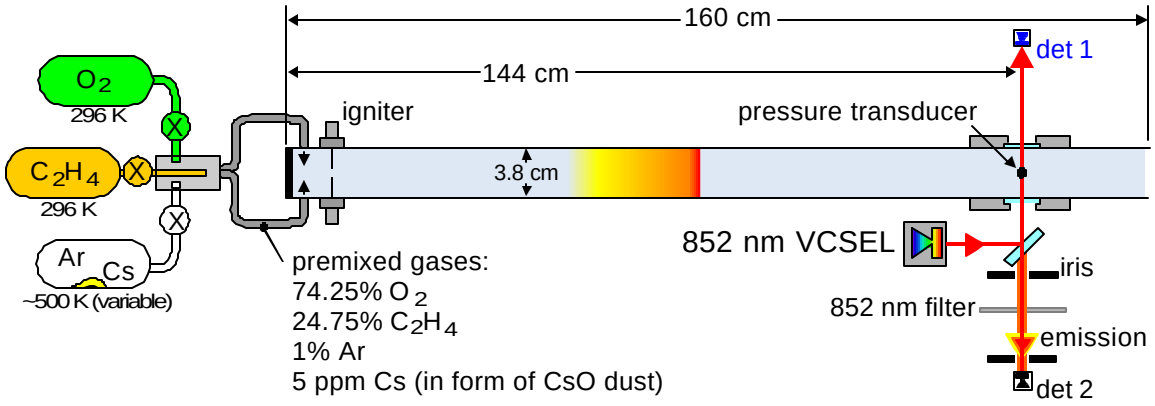

Figure 3.11. Schematic of Cs seeing system and Cs-based sensor for PDE gas temperature measurements. Detector 1 monitors Cs absorption lineshapes (whose area gives ground state Cs population) and detector 2 monitors Cs emission (whose intensity gives excited state Cs population). Cs electronic temperature is inferred from the ratio of these two populations. Alternatively, Cs kinetic temperature is inferred from the collisional linewidths in the detector 1 signal.

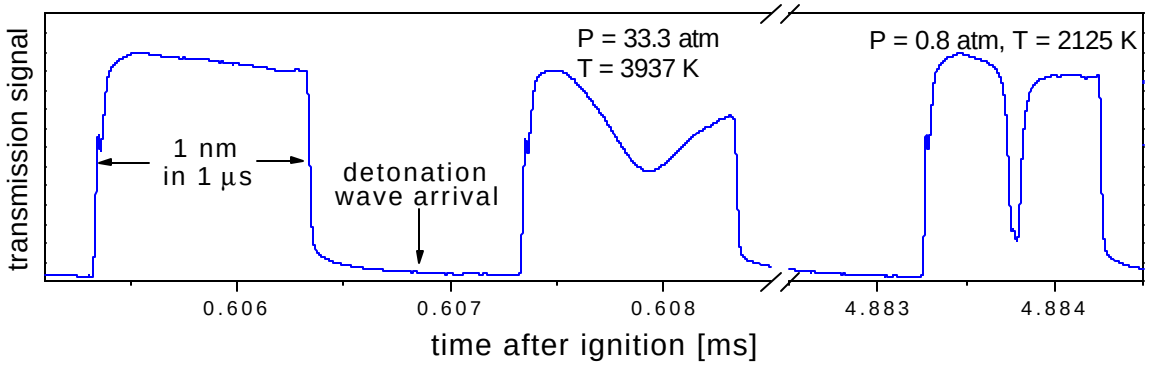

Figure 3.12. Raw Cs transmission data recorded by detector 1 of Fig. 3.11. The first scan shown is prior to the detonation wave arrival. The second is immediately following the detonation wave, and exhibits strong collisional broadening. The third is approximately 4 ms after the detonation wave arrival, and reveals hyperfine splitting.

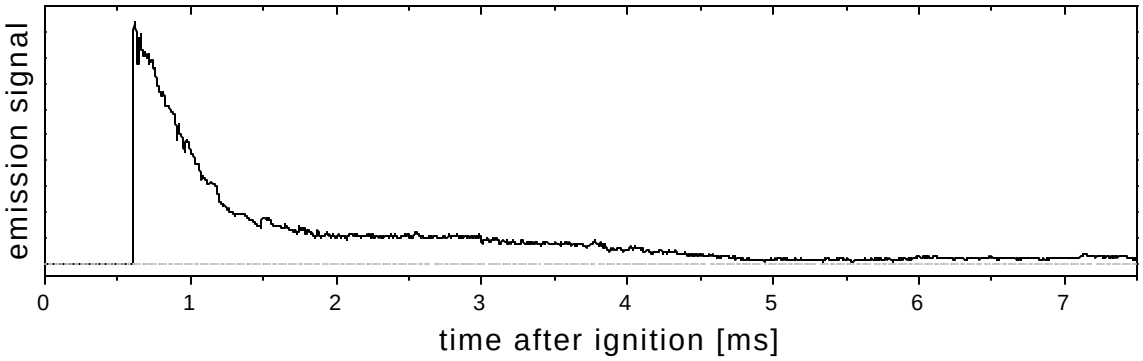

Figure 3.13. Raw Cs emission signal recorded by detector 2 of Fig. 3.11. This signal represents emission in the 852 ± 5 nm spectral region and is proportional to the Cs population in the excited $6^2P_{3/2}$ state.

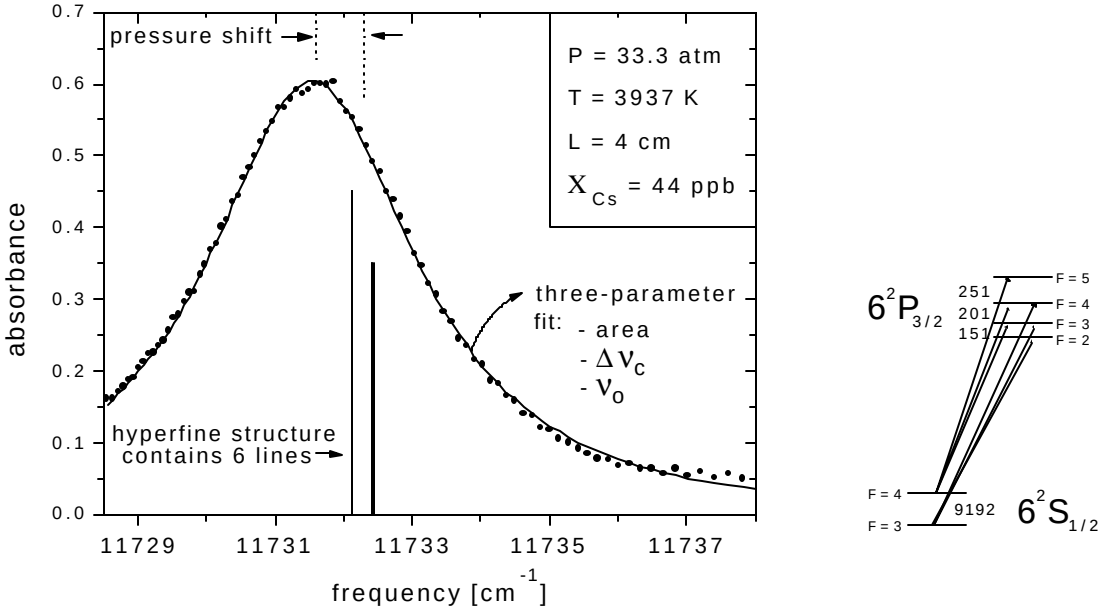

Figure 3.14. Cesium absorption feature recorded immediately after detonation wave passage. Although the feature contains six hyperfine-split transitions (see the energy level diagram on right: splittings are given in MHz), a two-line Voigt fit (assuming fixed spacing and fixed relative heights) is sufficiently accurate for extracting total feature area, collisional linewidths (assumed equal), and feature position.

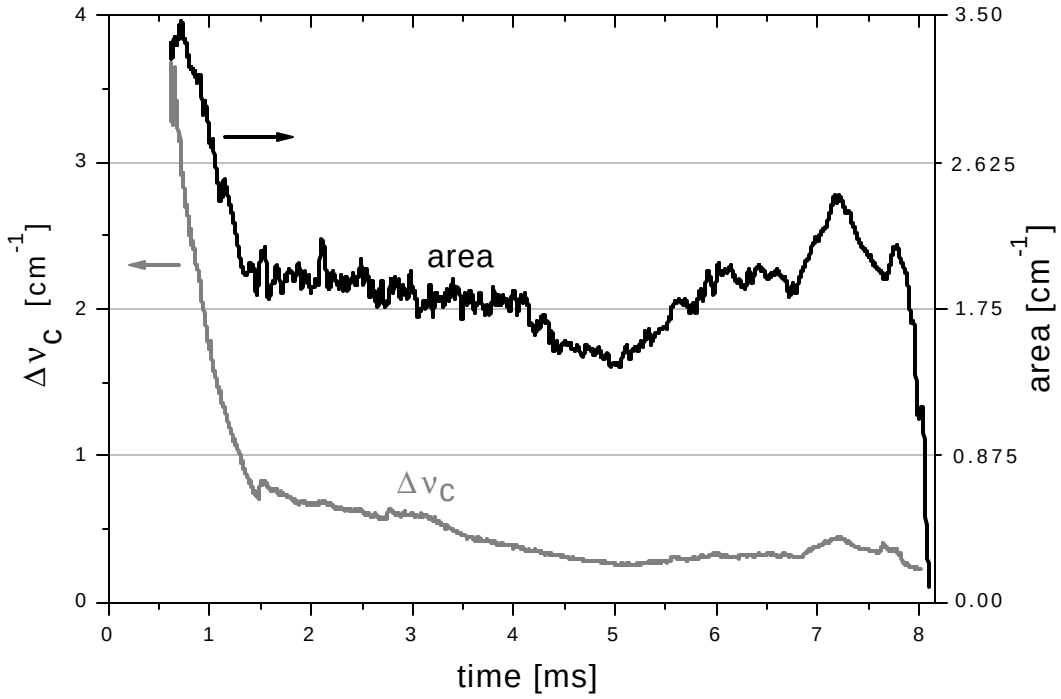

Figure 3.15. History of pertinent lineshape parameters obtained by repeated application (3709 total fits) of the two-line Voigt fit shown in Fig. 3.14. The total Cs absorption feature area (right-hand axis) provides the ground state Cs population, which is used to calculate $T_{Cs,\ electronic}$ (shown in Fig. 3.16). The collisional linewidth of each component line, $\Delta\nu_c$, is used to calculate $T_{Cs,\ kinetic}$ (also shown in Fig. 3.16).

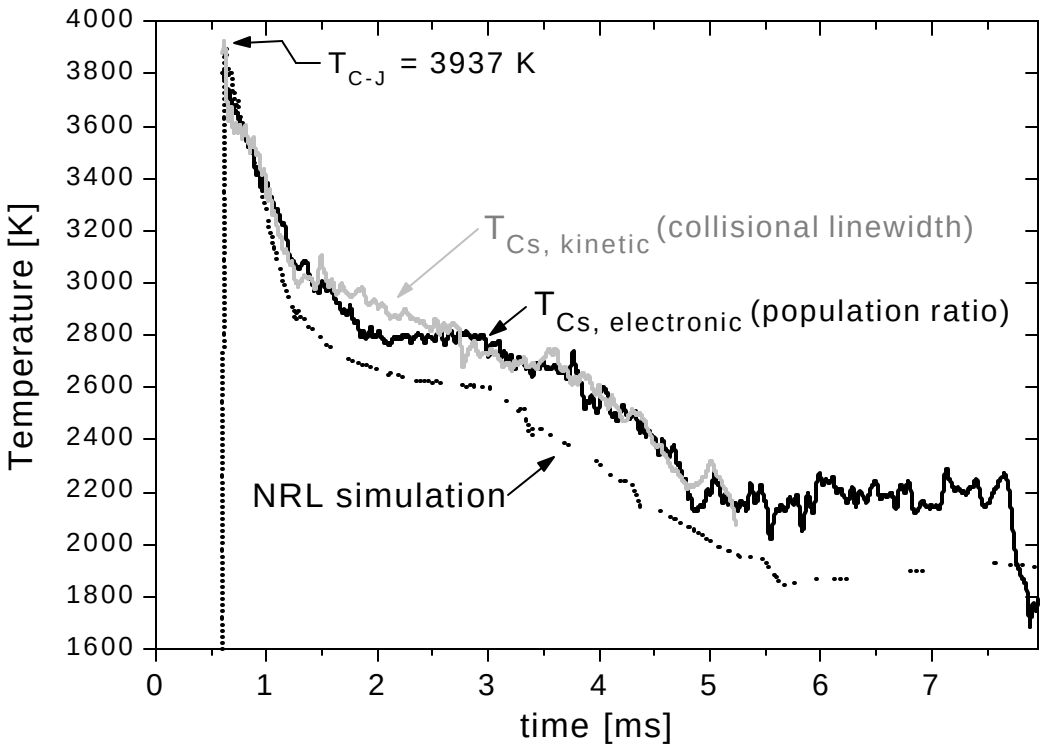

Figure 3.16. Measured and computed gas temperature histories for detonation of stoichiometric C_2H_4 / O_2 (relevant dimensions are provided in Fig. 3.11). The simulation assumes a fixed ratio of specific heats, k, which is somewhat inappropriate (see Fig. 3.17), and is likely responsible for disagreements of up to 14% in absolute temperature.

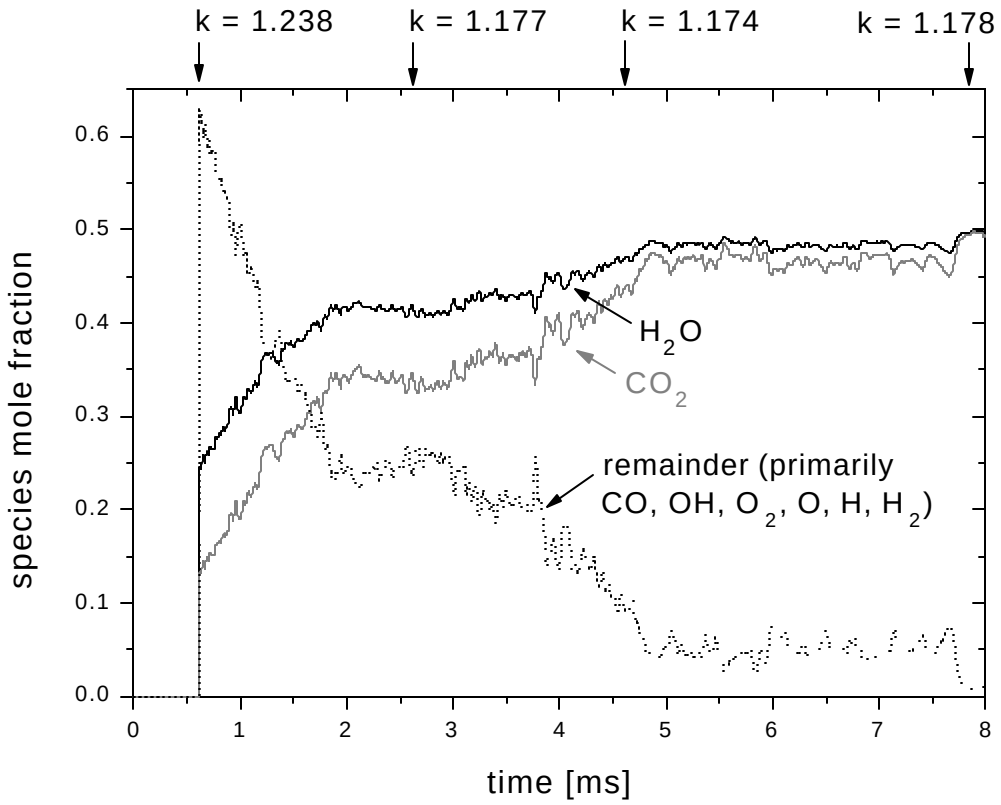

Figure 3.17. Calculated equilibrium species concentration histories for detonation of stoichiometric C_2H_4/O_2, obtained using the measured $T_{Cs,\ electronic}$ history shown in Fig. 3.16 and the measured $P_{spectroscopic}$ history shown in Fig. 3.19. The ratio of specific heats, k, is indicated at selected compositions.

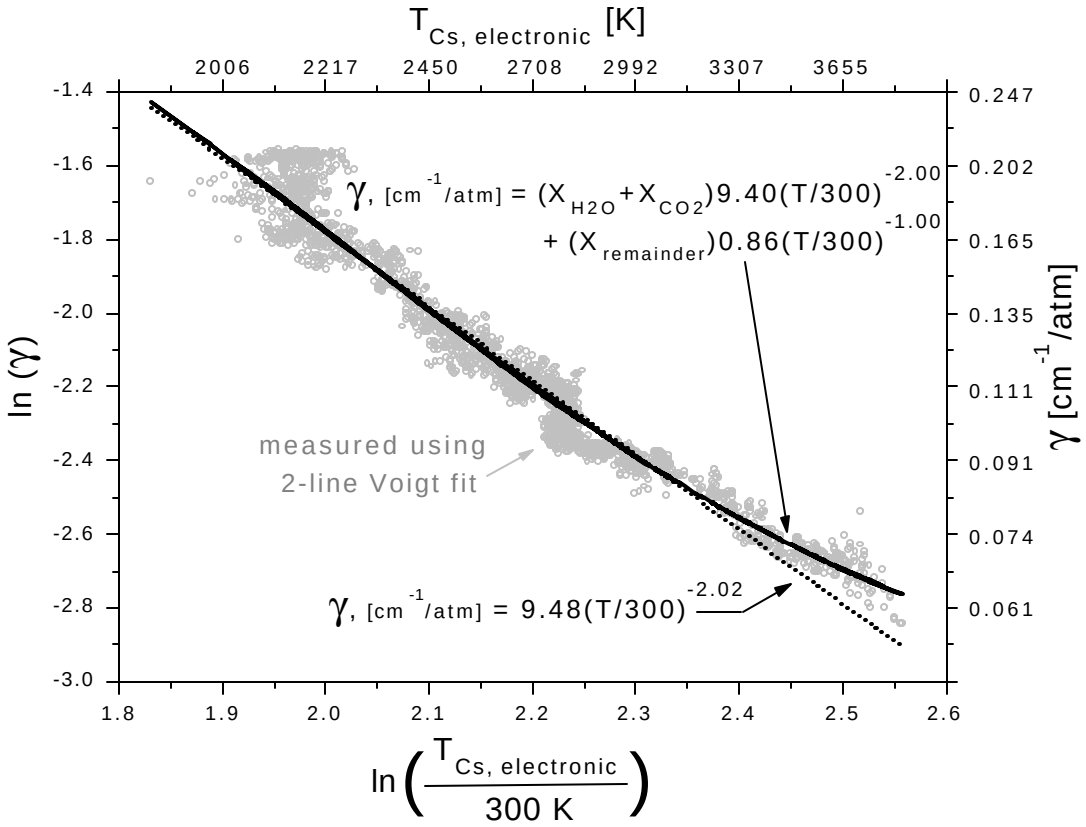

Figure 3.18. Determination of the best-fit overall Cs collisional broadening parameter, $\gamma_{\text{Cs-detonation products}}$, and its temperature dependence, using the measured Cs electronic temperature as the standard. The data deviates from a linear fit at high temperatures, presumably because of the changing gas composition shown in Fig. 3.17. To capture this trend, a composition-dependent fit is applied. Neither fit is intended to provide fundamentally accurate spectroscopic data; rather, the fits predict γ over a limited temperature range (2000 – 4000 K) and for a specific gas composition (namely, one approximating the equilibrium products of stoichiometric C_2H_4 / O_2). Using the composition-dependent fit, gas (kinetic) temperature can be determined from lineshape and pressure measurements, as illustrated in Fig. 3.16; alternatively, using the same fit, gas pressure can be determined from lineshape and (electronic) temperature measurements, as illustrated in Fig. 3.19.

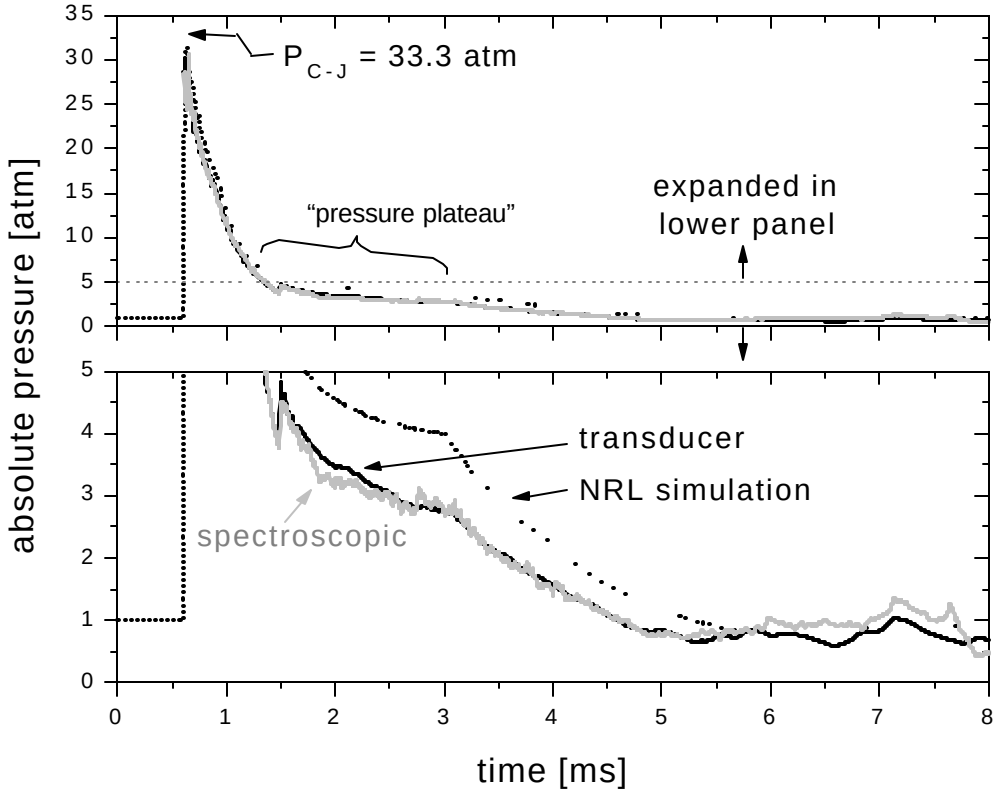

Figure 3.19. Measured and computed pressures for detonation of stoichiometric C_2H_4 / O_2 (relevant dimensions are provided in Fig. 3.11). The spectroscopic pressure is obtained using the measured $\Delta\nu_c$ history shown in Fig. 3.15, the measured $T_{Cs,\ electronic}$ history shown in Fig. 3.16, and the composition-dependent fit shown in Fig. 3.18. The transducer pressure record begins to disagree with the spectroscopic pressure record after t = 5 ms, presumably because it is designed to measure high pressures and has poor low-pressure accuracy, particularly when an intense pressure transient has recently occurred.

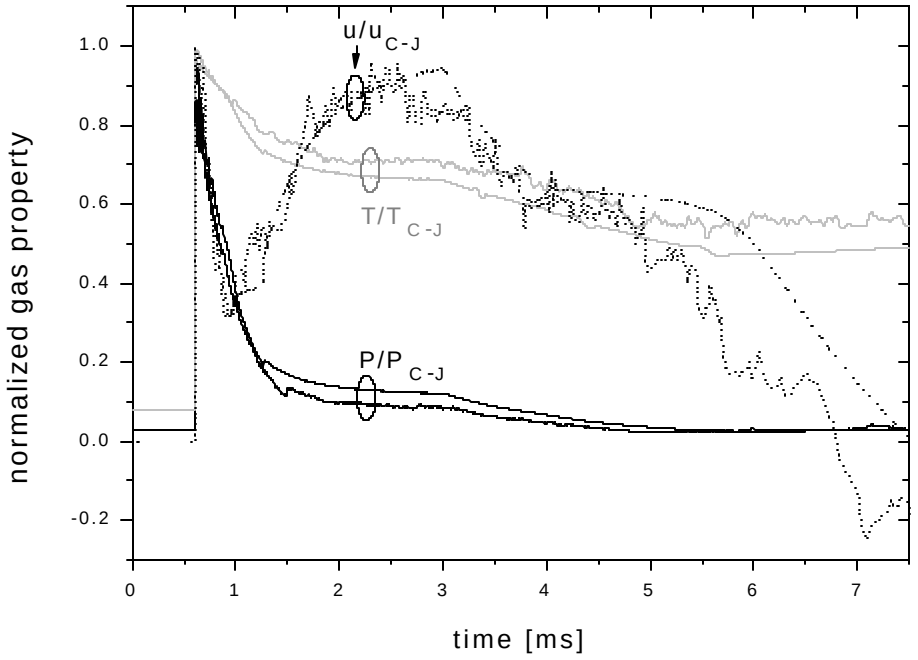

Figure 3.20. Summary of measured and computed gas properties for detonation of stoichiometric C_2H_4 / O_2 (relevant dimensions are provided in Fig. 3.11). The properties are normalized by their Chapman-Jouget values: u_{C-J} = 1039 m/s, T_{C-J} = 3937 K, and P_{C-J} = 33.3 atm. The measured temperature shown is $T_{Cs,\ electronic}$ (Fig. 3.16), and the measured pressure is $P_{spectroscopic}$ (Fig. 3.19).

Chapter 4

Beyond PDEs: the industrial potential of advanced sensors

1. Introduction

Chapter 3 has demonstrated the potential of advanced sensors, particularly those employing broad wavelength scanning, for obtaining quantitative measurements in PDEs. Other harsh environments, many of which receive greater industrial interest than PDEs, can be tackled using the same strategies. This chapter demonstrates the advanced capabilities of sensors that exploit broad wavelength scanning concepts, and projects their utility in a variety of harsh environments such as gas turbine and piston engines.

2. The advent of the VCSEL

VCSELs (vertical cavity surface-emitting lasers) are responsible for initiating many of the rapid- and broad-scanning ideas presented in this thesis. Among the first-generation, single-mode VCSELs, sold commercially in the 700–990 nm wavelength range, were lasers with a relatively high series resistance (~ 1 kΩ; traditional DFB and FP diode lasers exhibit ~ 10 Ω). This high series resistance provides increased joule heating during standard injection-current scans, which in turn leads to broad wavelength scans. In addition, the VCSEL's relatively small size (largest dimension ~10 μm; traditional

diode lasers are ~200 μm) improves the thermal time response of the diode, enabling rapid scans. Figure 4.1 demonstrates the rapid, broad wavelength scans obtained by current-tuning a typical VCSEL, contrasted to the current-tuning characteristic of a standard DFB laser. The utility of this increased tunability for spectroscopic purposes is illustrated in Fig. 4.2; more spectral information can be recorded, and more rapidly. The reader should beware, however, that not all VCSELs will offer the dramatic advantage seen in Figs. 4.1 and 4.2; many later-generation VCSELs have been manufactured with a reduced series resistance, and their current-tuning ranges will thus be decreased.

3. VCSEL-based sensors for high pressure environments

One of the great advantages of the increased wavelength tuning range offered by VCSELs is the ability to measure high-pressure absorbers (or quasi-broadband absorbers such as C_2H_4; see section 3.2). Historically, the ~1 cm^{-1} current-tuning range of standard DFB lasers has effectively limited scan-wavelength absorption spectroscopy to atmospheric- and low-pressure environments. Increasing collisional linewidths prevent higher-pressure measurements, as illustrated in Fig. 4.3 for the case of O_2 A-band absorption. The narrow DFB tuning range, sufficient for recording full lineshapes at 1 atm (see, for example, Fig. 4.2), does not enable scans over sufficient spectroscopic structure at 10 atm. The 10 cm^{-1} VCSEL scan shown in Fig. 4.3 is, however, sufficient for obtaining the blended spectroscopic structure shown in Fig 4.4. This blended spectra is obtained using advanced fitting procedures (Wang et al. 2001b) which permit

quantitative measurements of O_2 concentration even though the laser is never scanned to zero absorption (baseline). Such fitting procedures require that the high frequency structure in a recorded transmission signal is entirely due to gas phase absorption; the noise sources listed in Table 1.1 do not compromise the measurement accuracy provided they contribute only low-frequency noise to the transmission signal.

The ~30 cm^{-1} scans offered by VCSELs (see Fig. 4.1) are sufficient for obtaining spectroscopic structure (and thus quantitative gas property measurements) at pressures up to approximately 30 atm at room temperature and 100 atm at combustion temperatures. Furthermore, because the 30 cm^{-1} VCSEL scans can be made very rapidly (e.g., every 10 μs as demonstrated in Fig. 4.2), accurate measurements in transient, turbulent, or shocking flows are enabled. This dramatic extension (from the traditional 1 atmosphere, 1 ms response time limit) positions diode laser sensors for widespread industrial impact; simple sensors for high pressure flows such as gas turbine and piston engines can now be envisaged.

4. Simple, VCSEL-based temperature sensors

Section 4.3 has demonstrated the utility of increased wavelength-tuning range for enabling high pressure sensors. The increased tuning range can also be exploited to enable simple temperature sensors.

Figure 4.5 shows a sensor comprised of a single VCSEL and detector used to demonstrate temperature measurements in a heated static cell. The VCSEL is tuned over

10 absorption lines of the O_2 A-band, as shown in Fig. 4.6. Because these lines have different lower-state energies, gas temperature can be inferred from their integrated absorbance areas using a Boltzmann plot as shown in Fig. 4.7. Using this technique, gas temperatures of 288 and 700 K were inferred when the actual (thermocouple-measured) cell temperatures were 292 and 710 K (error ~ 1.4%). The major source of this error is the (laser excess) noise in the Fig. 4.6 data; longer pathlengths therefore reduce the 1.4% error. The ability to obtain such accurate, line-of-sight averaged temperature measurements with a simple, one-laser sensor may be useful for a variety of industrial process sensing and control applications. Note that since broad wavelength scanning is already exercised to obtain accurate temperatures, the sensor is automatically prepared to interrogate high pressure flows (up to 100 atm, as discussed in section 4.3).

5. VCSEL-based sensors for approximate temperature distributions

The Boltzmann plot discussed in section 4.4 implicitly assumes a uniform temperature along the line-of-sight. If the actual gas temperature is nonuniform, the Boltzmann technique yields a path-averaged temperature that is not the mean temperature, but is typically weighted towards the lowest temperature in the path (owing to number density effects). An example is obtained by probing the simple two-temperature path shown in Fig. 4.8. Two cells (T_1 = 712 K, T_2 = 296 K) are arranged in series and the resulting absorption data (this time using 2 VCSELs to scan 16 lines) is shown in Fig. 4.9. When this data is cast as a Boltzmann plot (Fig. 4.10), significant

curvature is evident. The linear fit that yielded accurate temperatures in the uniform temperature case (discussed in section 4.4) now yields the path-averaged temperature of 404K.

Fortunately, because many absorption lines are scanned, there is more information in the Fig. 4.10 Boltzmann plot than is captured with a linear fit. This fact enables sensors for line-of-sight temperature distributions. Two advanced data analysis techniques, the discretization technique and the distribution fitting technique—described below, have been developed for recovering temperature distribution information from line-of-sight absorption data when significant curvature exists in the Boltzmann plot. Additional details of such temperature distribution measurements are available in the literature (Sanders et al. 2001b). In brief, traditional diode-laser absorption thermometry probes two absorption lines to obtain a single path-averaged temperature (Arroyo et al. 1994); VCSELs probe many absorption lines to obtain multiple temperatures, temperature distributions, or fits to assumed temperature profiles.

5.1. Discretization technique

The discretization technique involves postulating an array of temperatures $\mathbf{T} = [T_1, T_2, \ldots, T_n]$ that are possible along the line-of-sight (e.g., [1200, 1400, . . . , 2200 K] could be postulated in a typical combustion flow). Then, the line-by-line integrated absorbance areas $\mathbf{a} = [a_1, a_2, \ldots, a_m]$ can be approximated as

$$\begin{bmatrix} S_1(T_1) & S_1(T_2) & \cdots & S_1(T_n) \\ S_2(T_1) & S_2(T_2) & \cdots & S_2(T_n) \\ \vdots & \vdots & \vdots & \vdots \\ S_m(T_1) & S_m(T_2) & \cdots & S_m(T_n) \end{bmatrix} \begin{bmatrix} (PxL)_1 \\ (PxL)_2 \\ \vdots \\ (PxL)_n \end{bmatrix} = \begin{bmatrix} a_1 \\ a_2 \\ \vdots \\ a_m \end{bmatrix} \qquad \text{(eqs. 4.1)}$$

or

$$\mathbf{Sx} = \mathbf{a}$$

where **S** is a matrix of linestrength values [cm^{-2}/atm] and the elements of **x** represent the product of gas pressure [atm], absorber mole fraction, and path length [cm]. The array **a** is measured, and because **T** was postulated, **S** is known (provided the pertinent spectroscopic parameters have been tabulated); therefore **x** can be found by solving eqs. 4.1. It is usually best to choose m > n, in which case eqs. 4.1 becomes a least squares problem for **x**, best solved using a non-negative least squares (NNLS) algorithm. Typically, the pressure P is uniform and known, and therefore can be divided out of the vector ***x***, leaving the solution [$(xL)_1$, $(xL)_2$, …, $(xL)_n$]. The product xL is termed the column density; in general, the discretization technique determines the column density present in each specified temperature "bin" defined by the postulated temperatures [T_1, T_2, …, T_n]. No information regarding the way in which the constituent column densities are arranged along the path is obtained.

5.2. Distribution fitting technique

The discretization technique described above has two main advantages: it is fast because a linear system is solved, and it requires very little *a priori* knowledge of the temperature distribution in the flow (i.e., if a temperature bin vector [T_1, T_2, …, T_n] is chosen with equally-spaced bins, only the expected minimum and maximum

temperatures, T_1 and T_n, are required). Its major drawback is that the discretization may be too coarse unless many bins are used, and too many bins can result in an ill-conditioned problem. It is often, therefore, advantageous to assume a general form for the temperature and mole fraction distributions in the flow, and obtain the best-fit distributions for a given measurement of the area vector **a**, using a nonlinear function minimization algorithm. Use of this technique requires that a suitable form for the distributions can be assumed. Because the assumption of such a functional form effectively constrains the problem, the distribution fitting technique is typically more stable than the discretization technique.

The same area data, ***a***, can be analyzed with either technique, as is demonstrated below. The resolution and accuracy of either technique increases with the number of lines scanned.

5.3. Experimental results

The results obtained by applying the discretization technique to the Fig. 4.9 absorption data are shown as gray bars in Fig. 4.11. The actual cell conditions of 712 and 296 K are shown as dotted bars for comparison. No *a priori* information about the path (except the gas pressure of 1 atm and the total path length of 40 cm) was used in the data reduction. Figure 4.11 highlights the sensor's potential for use in engineering applications: the sensor can provide rapid temperature distribution information of the type shown. Whereas previous sensors employing Fabry-Perot or DFB lasers have been limited to providing a single temperature and mole fraction along a line of sight, the VCSELs used by this sensor effectively allow a range of temperatures and mole fractions

to be measured. To illustrate the utility of such expanded information, consider applying the sensor to monitor flow properties near the fuel injectors in a gas turbine engine. Typically, maximum uniformity (i.e. all of the O_2 in a single temperature bin rather than distributed as in Fig. 4.11) is desired in this region. By measuring the major temperature components in the flow, the sensor could reveal unwanted hot spots, cold spots, and exceptionally-broad temperature distributions. In general, the sensor's ability to rapidly report data of the type shown in Fig. 4.11 should be useful for controlling systems whose performance is impacted by gas temperature distributions.

In this simple, two-temperature path, the distribution fitting technique amounts to assuming the existence of only two (uniform-property) cells, and determining which two temperatures and mole fractions best reproduce the measured **a** vector. For this case, the distribution fitting technique returns T_1 = 284 K, T_2 = 687 K, $x_{O2,1}$ = 0.188, and $x_{O2,2}$ = 0.225; these best-fit temperatures are within 4% and 10%, respectively, of the actual values.

In a second demonstration, the vertically-oriented cell shown in Fig. 4.12 was used to establish a stratified air column with a known, linear temperature distribution. Using a single laser to scan 10 R-branch absorption lines (the same lines scanned by VCSEL #2 in the two-temperature path demonstration), the absorption data shown in Fig. 4.13 were obtained. Because of the slightly longer path length and the cooler temperature portion, the peak absorbances are greater than in Fig 4.9, resulting in a higher signal-to-noise ratio. Therefore, even though only 10 R-branch lines are probed, the discretization technique yields very good results if relatively few temperature bins are used. The solution **x** to eqs. 4.1 is obtained using a NNLS algorithm. The column density, shown in

Fig. 4.14a (right vertical axis), is found by dividing **x** by the known pressure of 1 atm. To determine the total O_2 mole fraction, the vector **x** is divided by the known pressure of 1 atm and the known total path length of 50 cm, and the result is termed **x′**. The sum of the elements of **x′** is the measured value of x_{O2}, 0.226 in this case. The vector **x′′**, formed by dividing **x′** through by x_{O2}, represents the fraction of absorber in each temperature bin; **x′′** is plotted in Fig. 4.14a, referenced to the vertical axis on the left. The measured data shown in Fig. 4.14a is compared to the actual bin-wise discretization of the known linear temperature distribution. Because of the reduced number of bins employed, the discretization is relatively coarse, but the agreement between the measured and actual discretizations demonstrates the sensor's fidelity. Even when coarsely discretized, the sensor is potentially useful for applications requiring a broad sense of the temperature nonuniformity.

When the distribution fitting technique is used to interpret the linear temperature distribution data, the best-fit uniform-mole-fraction linear temperature distribution is found to have T_{lo} = 235 K, T_{hi} = 593 K, and x_{O2} = 0.227. This result is plotted in Fig. 4.14b. The measured temperature distribution is everywhere within 5% of the actual (thermocouple-verified) distribution. By imposing the known form for the temperature distribution, the same data that generated the coarse discretization of Fig. 4.14a was made to generate the more meaningful result of Fig. 4.14b.

The above experiments demonstrate that, in flows containing simple nonuniformities, the distribution fitting technique is more robust than the discretization technique, because it incorporates additional (user-supplied) information. The distribution fitting technique is especially useful whenever a simple and accurate

functional form for the property distributions in the flow is known or can be assumed. When such a form is not available (i.e., in the case of unknown or complex flow properties), the discretization technique may be favorable; this is especially true if approximate information is sufficient (i.e., if one is looking only for the appearance of a cold zone in a hot system), or if computational cost must be minimized (i.e., for rapid control applications).

5.4. Discussion

Although more powerful than standard two-line thermometry, the multi-line sensor is still a line-of-sight technique, and therefore provides no information regarding the way in which the composite temperatures are arranged along the probed path. *A priori* knowledge about a flow must be incorporated to gain such information. However, the sensor's fast time response (as fast as 10 μs in some cases) and simplicity make it more attractive than spatially resolved (e.g., LIF) techniques techniques for a variety of industrial flow monitoring and control applications.

It is well known that, in general, spectroscopic thermometry performs best over wide temperature ranges (measurements spanning the entire 300–3000 K range with 5% accuracy are straightforward but measurements in the 300–330 K range with 0.05% accuracy are nearly impossible; this is in contrast, for example, to vapor pressure thermometry). The reason for this behavior is that the Boltzmann distribution forces a relatively weak temperature dependence in spectra such as the one shown in Fig. 4.6.

Because of this behavior, measurements of narrow temperature distributions with the multi-line technique will be more challenging than measurements of wide ones. For example, if the above demonstration were repeated with cell temperatures of 396 and 296 K rather than 712 and 296 K, poorer results should be expected. The results could, however, be improved by scanning over more than 16 absorption lines (e.g., by multiplexing additional lasers). Still, the inability to resolve small temperature differences will limit the sensing technique, prohibiting, for example, accurate measurements of temperature fluctuations in most turbulent flows.

The most successful applications of the multi-line technique are expected to be in highly-nonuniform flows or flows in which the general form of the temperature distribution is known *a priori*. An important example of the latter is at the turbine inlet in gas turbine engines, discussed in section 4.7.

6. Rapid temperature-tuning of standard diode lasers

Sections 4.3-4.5 have demonstrated the utility of broad wavelength scanning for species concentration and temperature measurements as well as approximate temperature distribution measurements in flows up to high (100 atm) pressures. These advanced sensing capabilities were enabled by broadly-tunable VCSELs, which, at present, are only commercially available in the 700–1000 nm wavelength range, essentially limiting accessible species to O_2 and a handful of atomics (such as Cs). In contrast, standard edge-emitting diode lasers are currently available at many wavelengths throughout the

350–2000 nm range and therefore provide access to a wide variety of species of industrial interest (notably H_2O, CO_2, and fuels such as C_2H_4). In addition, recently-developed quantum cascade (QC) lasers offer wavelengths in the 2000–20000 nm range, further extending the list of accessible species. To facilitate application of the sensing strategies detailed in sections 4.3–4.5 to all diode-laser-accessible species, rapid temperature-tuning (RT-tuning) has been developed.

It is well known that most diode lasers can be broadly temperature-tuned. Slow, broad temperature scans (e.g., 1.9 nm in 10 minutes (Vogel et al. 2001)) are routinely employed, using a temperature-controlling device that is large relative to the laser active region. Most sensing applications require faster scans, however, because the scan duration (1 / scan repetition rate) equals the minimum sensor response time, which must be fast enough to track relevant changes in flow properties. Previous workers have therefore attempted to accelerate temperature tuning by using relatively small thermoelectric laser temperature controllers, but have estimated a temperature tuning limit of 0.1–1 Hz scan repetition rate (Allen 1998)—still too slow for most applications. Since injection current tuning enables scan repetition rates of approximately 1 kHz (see Fig. 4.1), sufficient for many applications, it has been used almost exclusively, even though only narrow wavelength scans (~ 0.3 nm) are possible.

Rapid and broad diode laser tuning is obtained by RT-tuning, wherein a temperature-controlling element of negligible thermal mass is used to modulate the laser output wavelength. To demonstrate the concept, we used a focused (~100 μm spot size) 5.4 W, 532 nm beam from a Coherent® Verdi laser to pulse-heat a 1.4 μm DFB diode laser as shown in Fig. 4.15. The 532 nm beam was chopped with a 50% duty cycle using

an acousto-optic modulator (AOM) to generate the heating pulses. The diode laser's gold surface reflected approximately 50% of the incident power, so that ~ 2.7 W (sufficient to raise the temperature of the active region ~ 60 ^{o}C) was absorbed during the heating pulse; the diode then cooled ~ 60 ^{o}C by conduction between heating pulses.

RT-tuning enabled a 10-fold increase in the DFB laser tuning range offered by standard current-tuning techniques, as shown by the solid curves of Fig. 4.16. The curves are plotted versus scan repetition rate, which equals twice the heating laser chopping frequency because both diode laser scan directions (heating and cooling) are counted. Both solid curves in Fig. 4.16 roll off at high scan repetition rate due to the thermal capacitance of the diode; their similar shapes indicate that RT-tuning is identical to injection-current tuning from a time-response standpoint, and simply enables a deeper thermal modulation. Whereas the maximum thermal modulation depth (the maximum tuning range) for current-tuning is limited by optical destruction of the laser facets, the maximum thermal modulation depth at a given scan repetition rate for RT-tuning will be limited by thermal destruction of the diode's integrity. The latter has not yet been thoroughly investigated; however, the laser used in these experiments was cycled through 60 ^{O}C at kHz rates for several minutes without an observable performance degradation. Furthermore, the laser's intensity noise, linewidth, and scan-to-scan wavelength repeatability matched typical injection-current tuning values. The (dashed) VCSEL current-tuning curve (Wang et al. 2001b) is shown for reference in Fig. 4.16. The VCSEL's higher series resistance and smaller size are responsible for the higher tuning range and higher-frequency roll-off.

To illustrate the virtue of the increased tunability offered by RT-tuning, we measured absorption spectra of H_2O vapor in the 1–10 atm range by directing the 1.4 μm diode laser beam through a gas cell as shown in Fig. 4.15. The laser power and tuning characteristics were monitored with a reference and etalon arm, respectively. Raw data from each of the detectors listed in Fig. 4.15 are shown in Fig. 4.17 for cell conditions of T = 292 K, P_{H2O} = 15 Torr, P_{air} = 1 atm. The etalon trace (free spectral range = 0.4 cm^{-1}) reveals that the wavelength tunes nonlinearly in time; however, the AOM could be programmed to provide arbitrarily-shaped heating pulses to linearize the tuning characteristic if desired.

The reference trace in Fig. 4.17 reveals an approximately constant laser power during the wavelength scans. This near-decoupling of wavelength and intensity modulation (common to all temperature-tuning techniques) has several advantages for spectroscopic sensing. For example, it enables arbitrarily-shaped heating pulses without severe power-curve distortion; current tuning, by contrast, often suffers from such severe power-curve distortion that only one of the scan directions (heating or cooling) is useful for spectroscopic measurements. Additionally, because the heating pulses control the wavelength, the need for an electrically-clean but rapidly-modulating current source is eliminated, and a low-noise DC current source can be used instead.

Raw data traces such as those shown in Fig. 4.17 were reduced to the absorption spectra shown in Fig. 4.18 using established methods (Nagali et al. 1999). Collisional broadening blends the spectral features together at high pressure, demanding a greater tuning range to recover the spectroscopic structure necessary for accurate measurements.

To our knowledge, Fig. 4.18 presents the first rapid-scan measurement of an entire high pressure H_2O absorption feature using a diode laser.

RT-tuning dramatically improves diode-laser gas-sensing capabilities, and can potentially advance a variety of scan-wavelength systems. Systems that require the laser to scan rapidly and then lock to a new wavelength could be constructed from a marriage of RT-tuning concepts and existing diode-laser temperature control strategies (Li et al. 1993).

Future RT-tuning realizations could employ more efficient strategies (e.g. direct heating of the semiconductor material with an auxiliary diode laser) or device modifications (e.g., small resistive heaters) to replace the high power laser used in these demonstrations. The device properties (e.g., thermal conductivity, size) could also be adjusted to minimize heating power requirements or maximize tuning speed.

7. Projected applications and recommendations for future work

Several applications of the sensing strategies described in this chapter are envisioned, enabling both basic and applied research. Supporting basic research, the ability to rapidly record flow properties in high-pressure environments (as demonstrated in section 3.5) provides opportunities for detailed studies of high-speed, transient, or shock-heated flows. An example of particular interest is temperature monitoring in shock tubes used for chemical kinetics studies.

One motivation for such measurements is to validate mechanisms for ignition of fuels *when the pre-shock fuel concentration is higher than ~ 1000 ppm*. Under these circumstances, chemical heat release significantly alters the post-shock gasdynamics. Thus, the bulk gas properties, which must be known throughout the ignition event to facilitate meaningful validations, cannot be predicted by simple theory. However, by direct measurement of the bulk gas pressure (using standard transducers) and temperature (using RT-tuning), meaningful data for mechanism validation can be collected.

The strategy for recording shock tube temperatures exploits the ability of RT-tuning to provide 1.5 cm^{-1} scans at 100 kHz, as shown in Fig. 4.16. Although standard injection-current tuning techniques provide 1.5 cm^{-1} scans, they do so only at 1 kHz, which is too slow for shock tube measurements. The 100 kHz scan repetition rate offered by RT-tuning enables temperature measurements every 10 μs, using traditional two-line diode laser thermometry (e.g., following Arroyo 1994), as long as the gas pressure is less than ~ 2 atmospheres. To facilitate such measurements in energetic shocks, ~ 1000 ppm H_2O vapor could be seeded into the pre-shock gases.

In the applied realm, the sensing strategies presented in this chapter provide new opportunities for studying high-pressure combustion environments such as gas turbine and piston engines. Of particular interest are measurements of gas temperature distributions at the turbine inlet in gas turbine engines. Here, the flow is tailored to have a high average temperature (permitting high thermal efficiency) but with cool spots in critical locations to prevent mechanical failure of turbine components. To optimize the temperature distribution, active control (e.g., of pattern factor or profile factor) is desired. The techniques presented in this chapter can be combined to develop robust sensors for

such control. Multiplexed, RT-tuned lasers can be used to scan over many high pressure (~30 atm) H_2O absorption features (the RT-tuned lasers could be replaced by long-wavelength VCSELs when they become available; see section 4.8). The multi-line technique can then be applied to determine an approximate, line-of-sight temperature distribution. Since intense modeling efforts have been applied to this flow, the general form for the expected distribution is already known; the reduction of the multi-line data to temperature distributions can incorporate this information to achieve accurate results.

In IC engines, line-of-sight averaged data is generally meaningless due to the highly-nonuniform flowfield. PLIF in optically-accessible engines has therefore become the norm; however, PLIF results are plagued by uncertainties associated with the noise sources (e.g., scattering and absorption due to soot and liquid fuel) listed in Table 1.1. Because diode-laser sensors based on broad wavelength scanning are immune to these noise sources, there is reason to apply them for in-cylinder measurements, particularly if spatially-resolved data can be recovered. Tomographic diode-laser sensors have been thoroughly established (Silver et al. 1995) for recovering spatial information from data taken along several lines-of-sight. The spatial resolution of the data is expected to be enhanced if the multi-line technique (section 4.5) is applied along each line of sight. Although it will be laborious to develop such a sensor, the sensor's potential ability to record quantitative and time-resolved images in IC engines is very attractive.

8. Survey of upcoming wavelength-agile technologies

Although first-generation VCSELs dominate Figs. 4.1 and 4.16, they are not the ultimate destination in the quest for rapid and broad wavelength tunability. Recently, the communication industry has sought "wavelength-agile" lasers for advanced optical networks. Lasers (both VCSELs and edge-emitters) that outperform the first-generation VCSEL in the spirit of Fig 4.16 are soon expected to be commercially available, at least in the 1.5 μm range.

Injection-current tuning and RT-tuning are both forms of temperature tuning; the laser wavelength is tuned because the changing temperature changes the index of refraction and therefore the resonant condition inside the laser cavity. Although simple to implement, temperature tuning is a poor candidate for achieving ultra-broad tunability, because materials failure considerations become an issue. In the RT-tuning experiments summarized above, temperature gradients as high as ~ 0.3 K / μm were temporarily established in the semiconductor material. Although no laser failures were observed in several minutes of testing, a preliminary failure analysis predicts that this temperature gradient should generate stresses near the threshold for cracking the semiconductor. Specialized laser design (i.e., tailoring the thickness and thermal conductivity of the semiconductor and its mounting structures to reduce thermal gradients) could be applied to enable RT-tuning without this danger. The VCSEL, in fact, is essentially immune to thermal gradient failures because of its small size. However, the high temperatures alone are of concern because they speed laser failure. The VCSEL's high series resistance (which enables the superior performance on Fig. 4.16) generates temperature swings of ~

100 C during injection current scans; if the case temperature is 0 C, the laser will temporarily reach 100 C during each scan. The lifetime of a typical diode laser at 100 C is only about 1 hour, compared to 770,000 hours at 20 C.

Because of the failure limits associated with broad temperature tuning, upcoming wavelength-agile technologies aim to introduce new tuning mechanisms. One example is the cantilever-VCSEL (c-VCSEL) that floats one of the laser facets (mirrors) on a moveable micro-cantilever (Chang-Hasnain 2000). The position of the mirror can be adjusted rapidly, and with it the laser wavelength. Another example is the sampled-grating DBR (SGDBR) laser, part of a family of monolithic tunable diode lasers of which a recent review is available (Coldren 2000), in which gratings at both facets are adjusted electrically to achieve broad wavelength scans.

Compared to the 4 nm offered by RT-tuning, these upcoming technologies aim to produce lasers whose tuning range is limited only by the spectral bandwidth of the gain medium. Lasers offering > 40 nm tuning (at up to MHz repetition rates) may soon be commercially available. Such lasers could be effective for further enhancement of the spectroscopic techniques discussed in sections 4.3–4.5 (e.g., enabling rapid measurements of very high pressure, broadband, or even liquid absorbers). There are obstacles, however, to their direct application in spectroscopy. Wavelength-agile lasers for communications applications are generally designed to *switch* rather than *scan* to a new wavelength; implementation of the scanning that is preferable for spectroscopic purposes (see section 1.5) may not be straightforward. Additionally, even if scans are possible, they may exhibit very high phase noise (meaning the laser does not tune smoothly from wavelength “a” to wavelength “b”, but “jitters” along the way). This

feature will pose a major problem for high-resolution spectroscopy (e.g., scans over many atmospheric-pressure gas-phase absorption features) but only a minor problem for broadband or high-pressure absorbers.

9. Advanced wavelength multiplexing

Although this chapter has emphasized wavelength-agile techniques for sensing in harsh environments, advanced wavelength multiplexing could be an attractive alternative in future applications. Traditional wavelength-multiplexed spectroscopy has combined relatively few (2–7) wavelengths along a single line of sight, yielding information at a handful of discrete wavelengths as illustrated in Fig. 1.4. Advanced wavelength multiplexing techniques, such as dense wavelength division multiplexing (DWDM – an existing communications technology) can be considered for providing relatively continuous spectral information.

A typical DWDM system combines many (up to 1000) wavelengths, spaced by 10-200 GHz, transmits them through the same fiber, and then detects each wavelength's intensity independently. Because such systems are maturing as communication devices, they could become inexpensive and robust enough for sensing applications. The narrow channel spacing renders the spectral information nearly continuous, resembling the information obtained from wavelength scanning techniques. However, unlike wavelength scanning, advanced wavelength multiplexing techniques are not limited by laser scan time, and therefore could be useful for sensing in extremely transient flows.

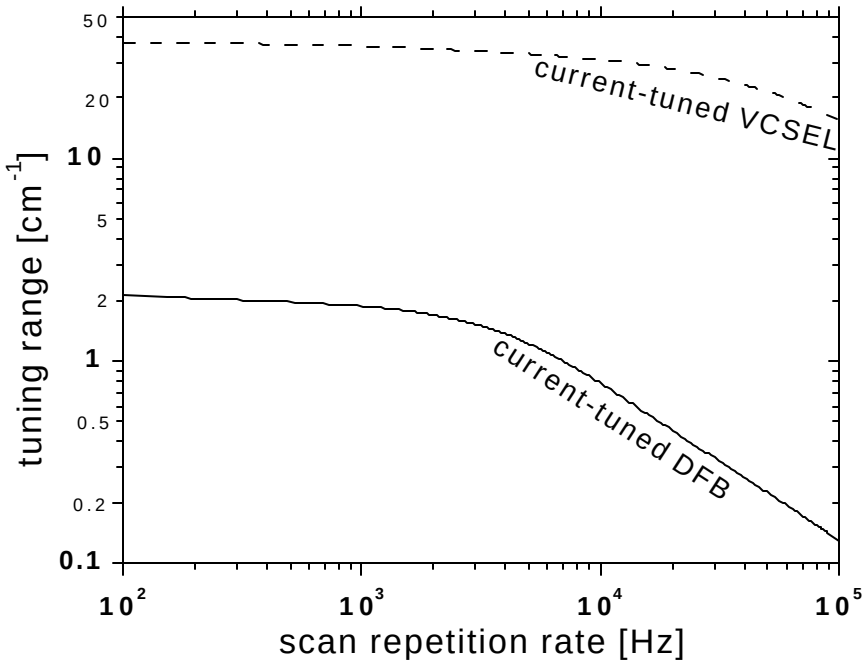

Figure 4.1. Injection-current tuning curves for a typical VCSEL and DFB laser. Many harsh environments demand rapid, broad wavelength scans; the VCSEL is superior to the standard DFB for this purpose.

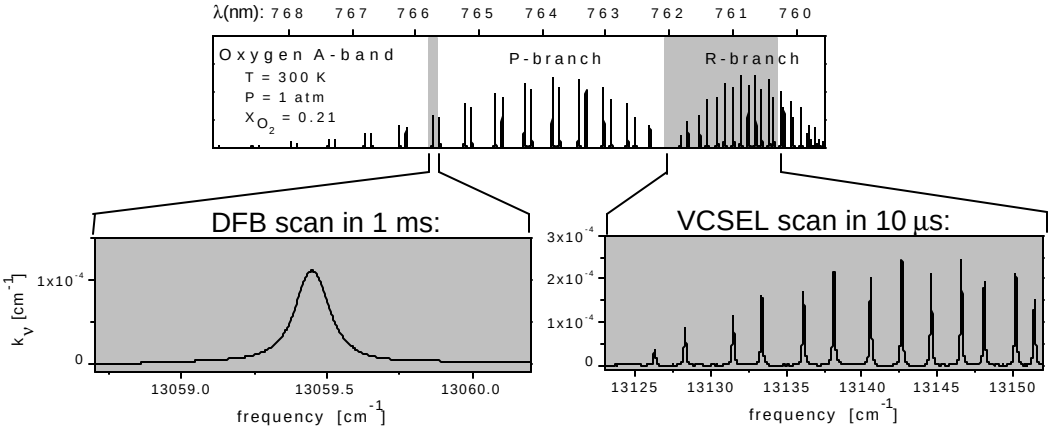

Figure 4.2. Sample measured O_2 A-band absorption spectra, highlighting the increased tuning range (× 20) and rate (× 100) offered by VCSELs.

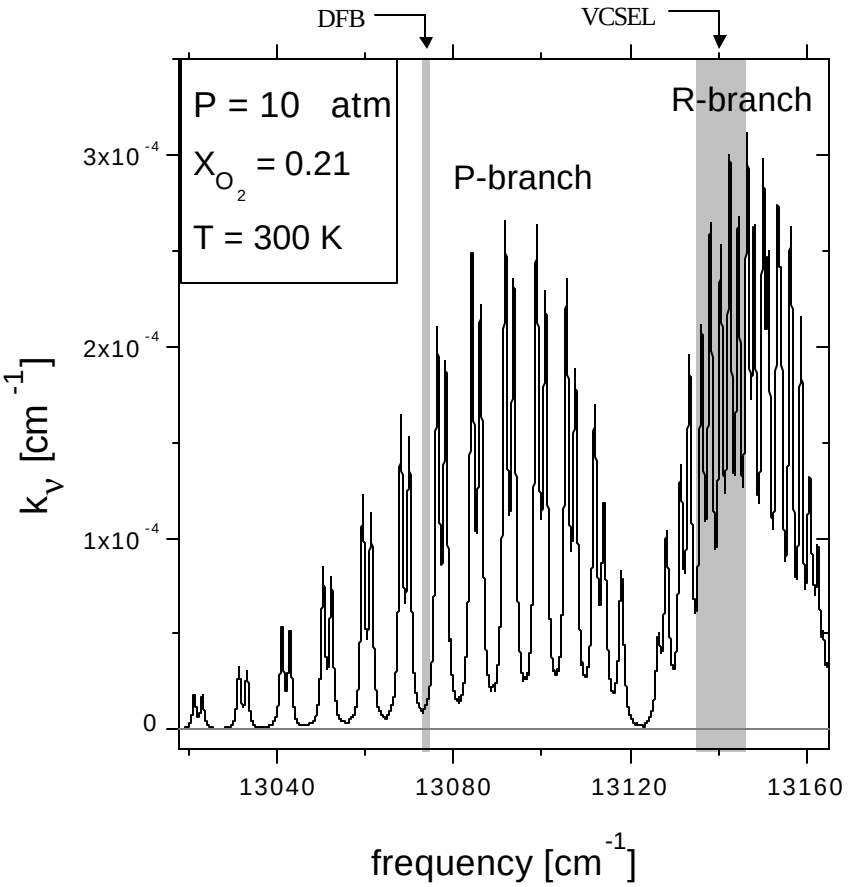

Figure 4.3. Simulated high-pressure O_2 absorption spectrum, highlighting utility of increased tuning range. The DFB tuning range is insufficient to recover spectroscopic structure, whereas the VCSEL tuning range enables the measurements shown in Fig. 4.4.

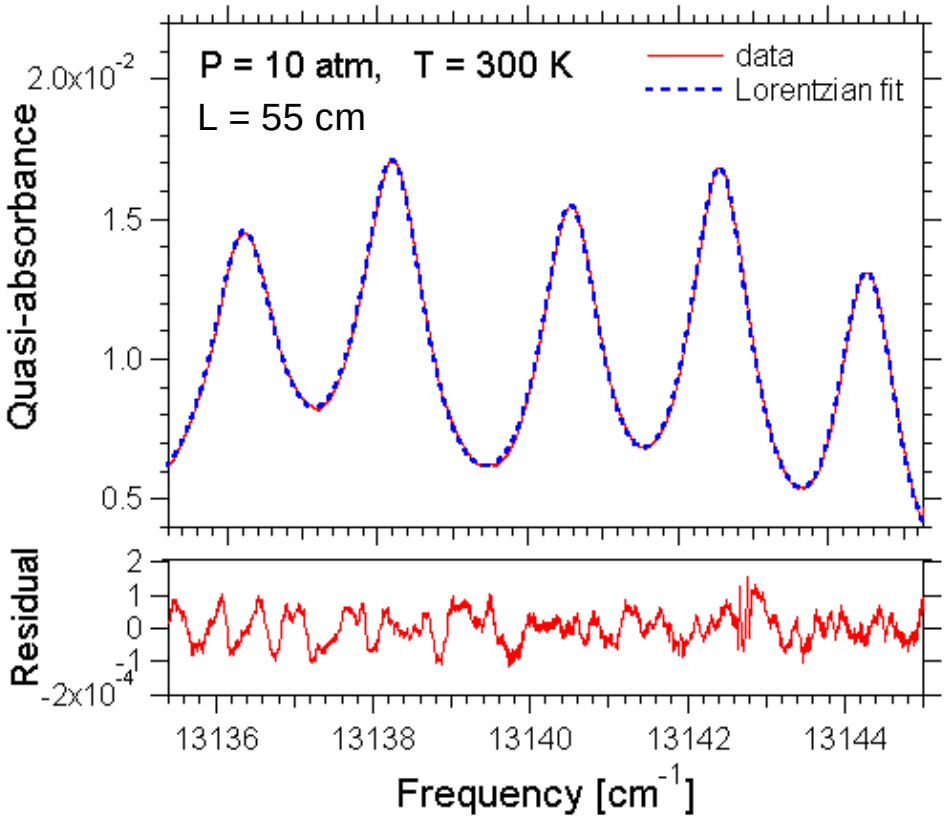

Figure 4.4. Measurement of the blended 5-line high pressure O_2 absorption feature highlighted in Fig. 4.3. Because no baseline can be obtained (the laser is never tuned to regions of negligible absorption) in this 10 cm^{-1} scan, advanced fitting routines based only on the structure of the absorbance (termed "quasi-absorbance") and not its absolute value (Wang et al. 2001) are used.

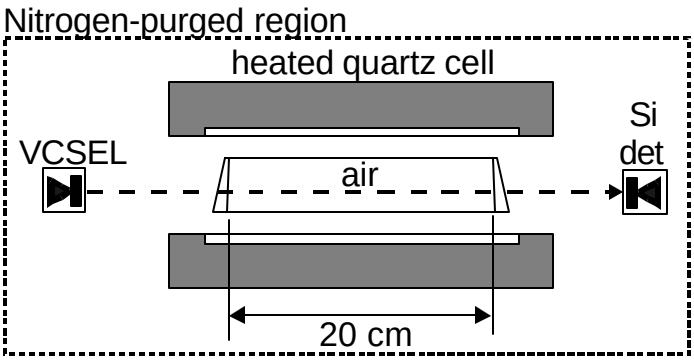

Figure 4.5. Schematic of single-VCSEL absorption sensor used for measuring gas temperature.

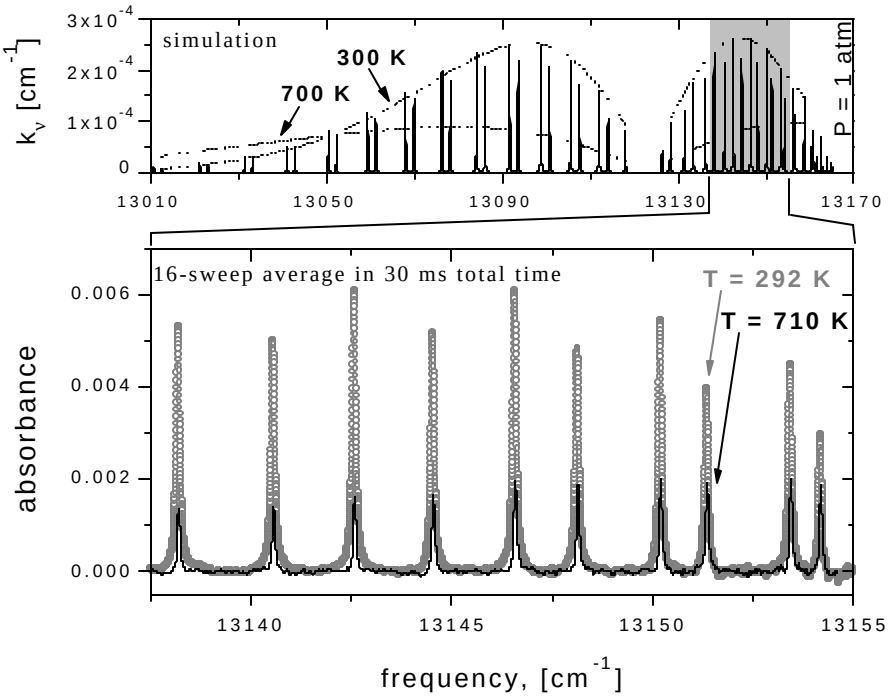

Figure 4.6. Measurements of 10 O_2 A-band absorption lines using the system shown in Fig 4.5. Results for two temperatures are shown; the relative heights of the 10 lines are sensitive to temperature, enabling the measurements depicted in Fig. 4.7.

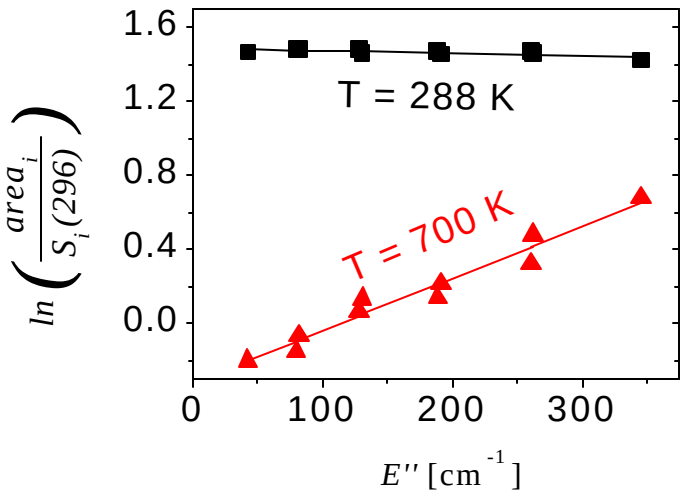

Figure 4.7. Boltzmann plot used to determine gas temperature from the absorption data shown in Fig 4.6.

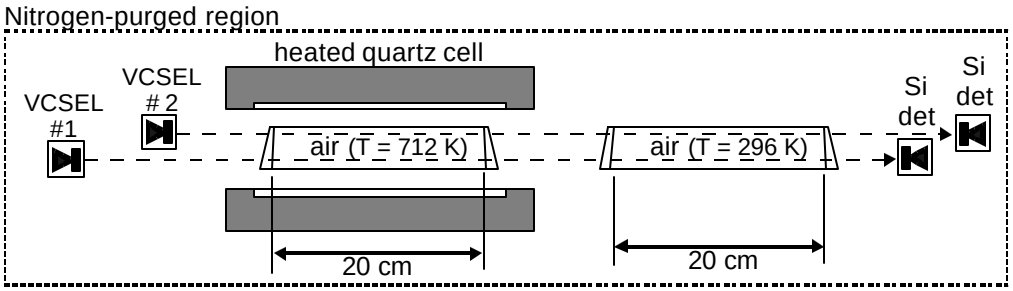

Figure 4.8. Two-temperature path used to demonstrate ability to recover temperature distribution information from a line-of-sight measurement of many absorption lines.

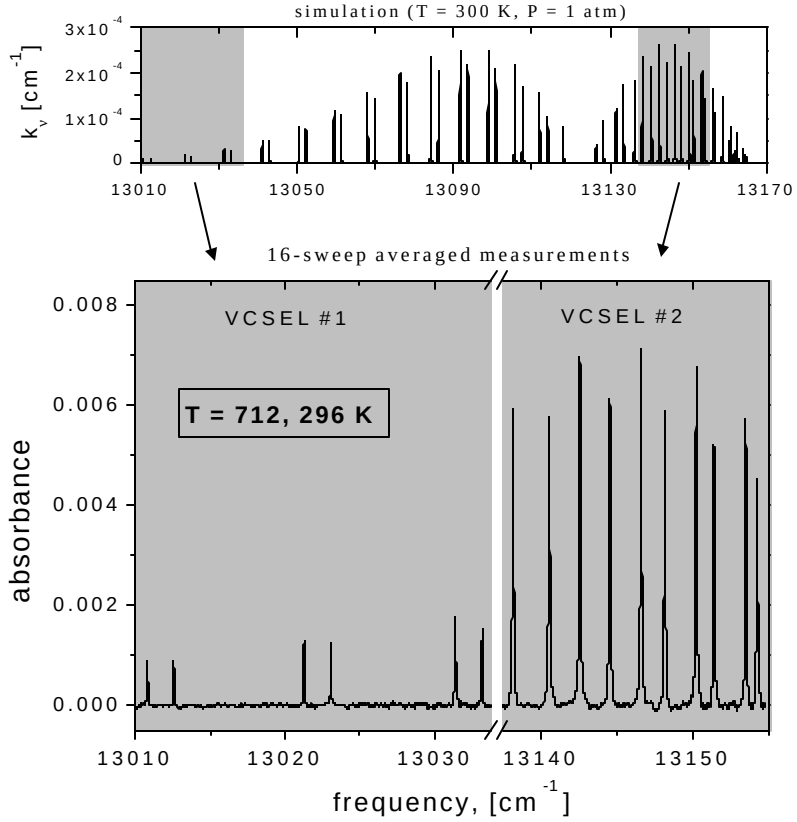

Figure 4.9. Combined absorption data from the two VCSELs shown in Fig. 4.8, recorded in 30 ms total time.

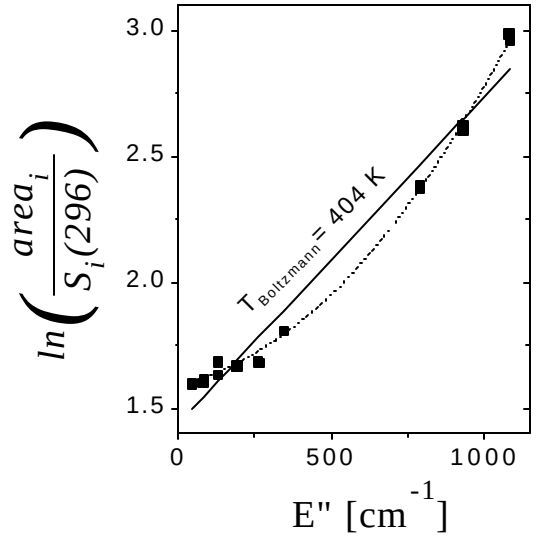

Figure 4.10. Boltzmann plot corresponding to the Fig. 4.9 absorption data. Because of the nonuniform temperature (see Fig. 4.8), significant curvature is evident; advanced data analysis schemes that consider the shape of the Boltzmann plot can infer temperature distributions, as demonstrated in Fig. 4.11.

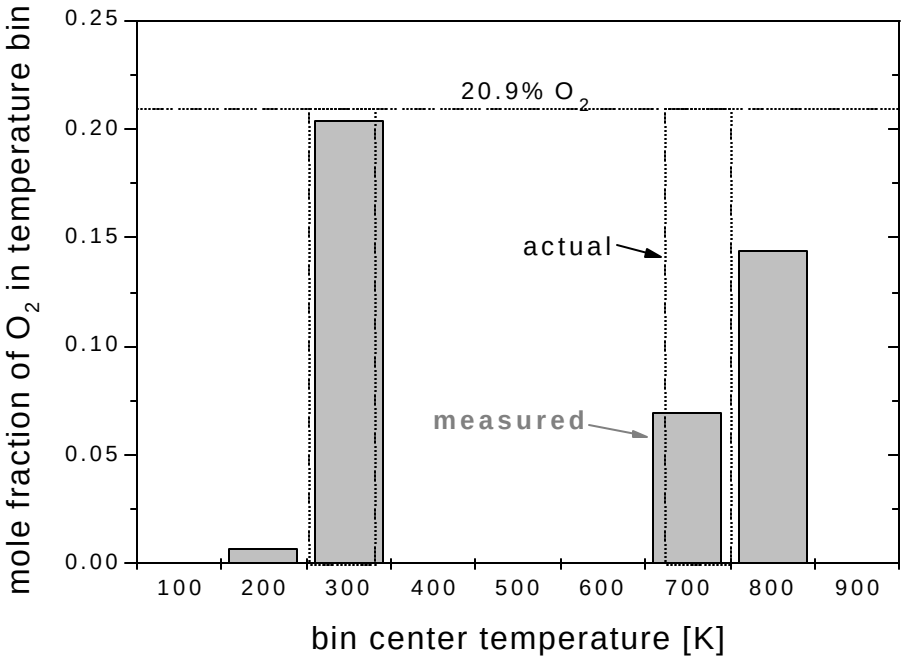

Figure 4.11. Sample temperature distribution measurement. Gray bars represent the temperature distribution inferred from the Fig. 4.9 data using advanced techniques (see Sanders et al. 2001b). Dotted bars correspond to the actual cell conditions shown in Fig. 4.8.

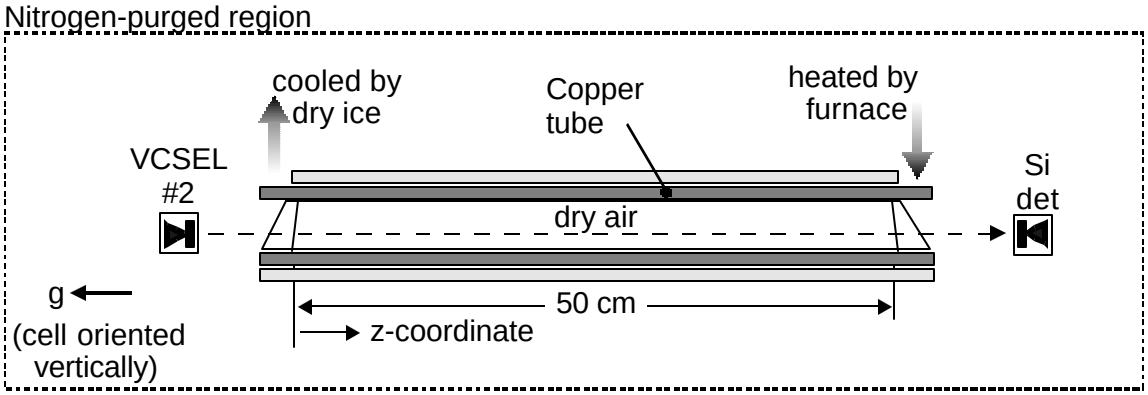

Figure 4.12. Cell used to demonstrate multi-line sensor in along a path containing a linear temperature distribution.

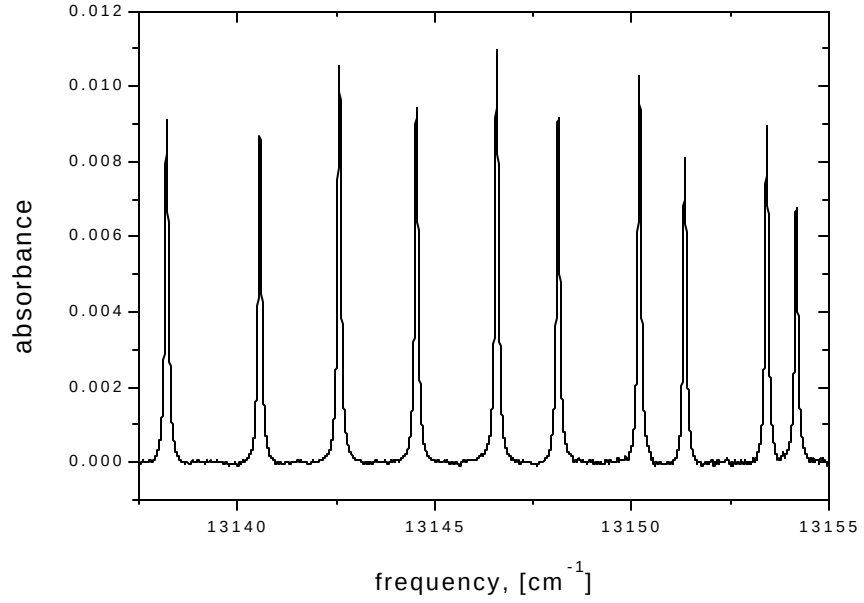

Figure 4.13. Absorption data recorded in the linear temperature distribution shown in Fig. 4.12. Lines scanned are the same scanned by VCSEL #2 in Fig. 4.9.

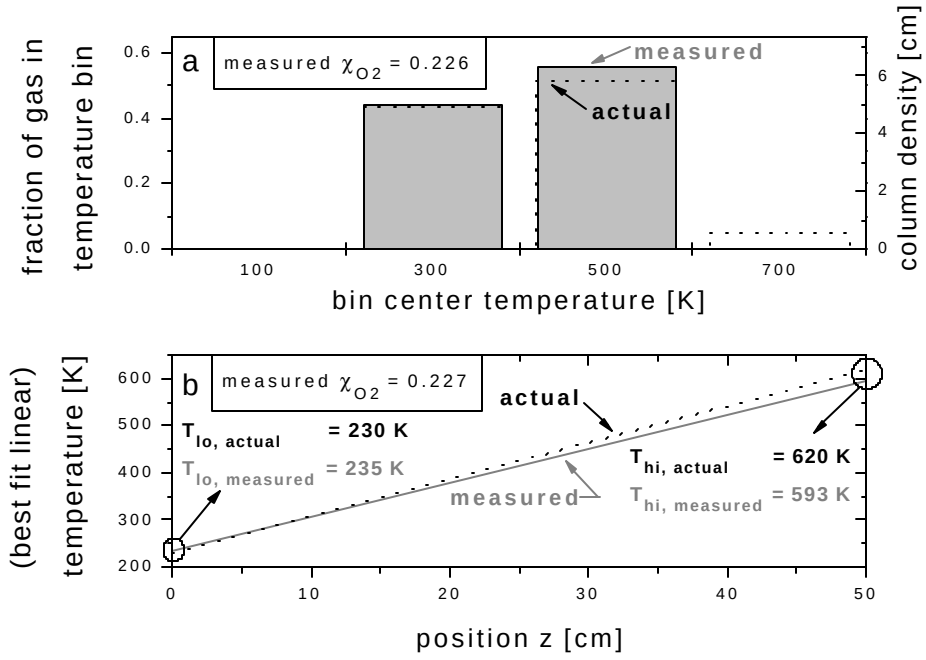

Figure 4.14. Linear temperature distribution results: a) discretization technique; b) distribution fitting technique.

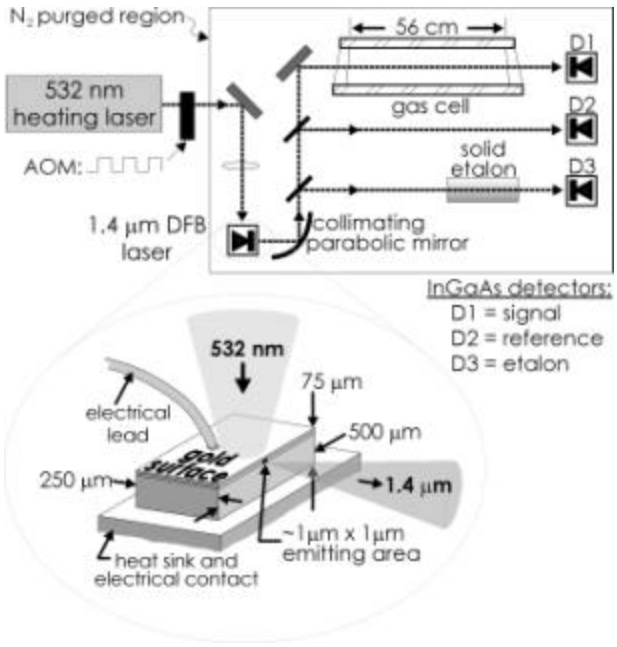

Figure 4.15. RT-tuning experimental schematic. Pulses of 532 nm radiation rapidly heat the diode laser, providing broadly-tunable 1.4 μm output.

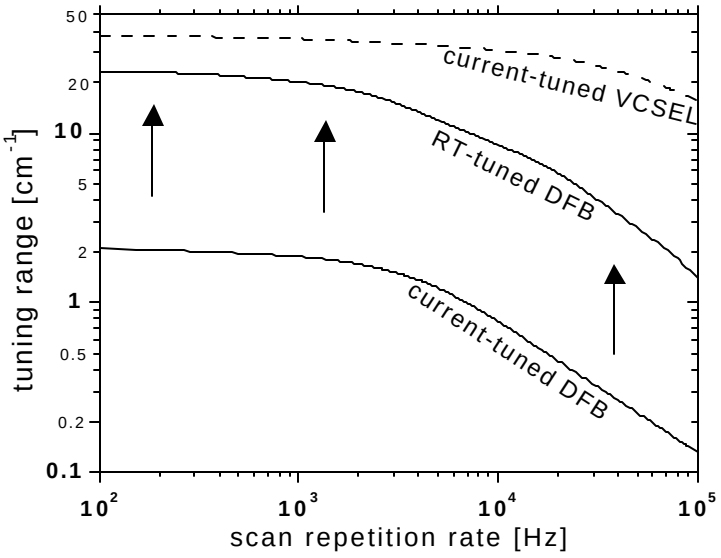

Figure 4.16. Demonstration of increased DFB tuning range offered by RT-tuning. Note that the VCSEL outperforms even the pulse-heated DFB, both in terms of range (due to its high series resistance) and rate (due to its small size).

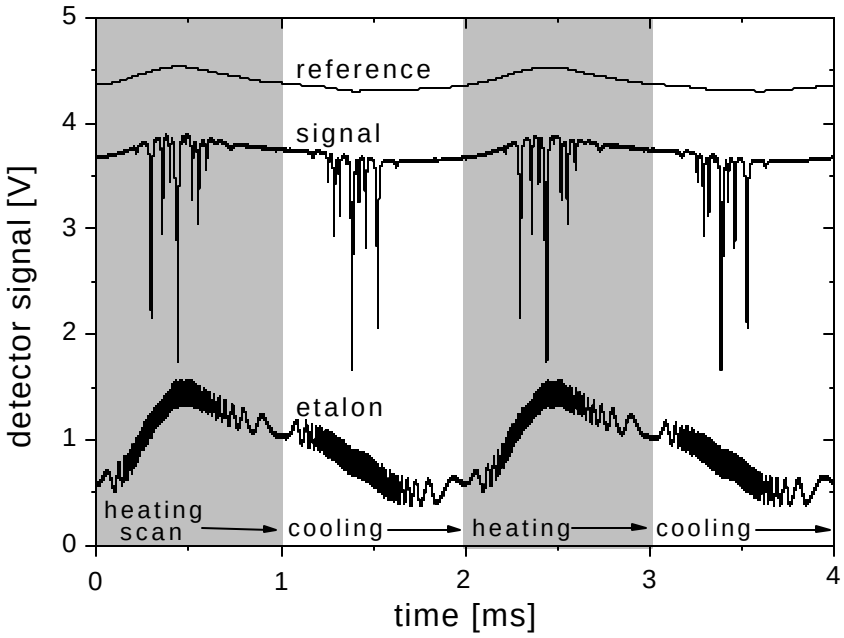

Figure 4.17. Raw data recorded from each of the 3 detectors listed in Fig. 1 at 1 kHz scan repetition rate (P_{air} = 1 atm).

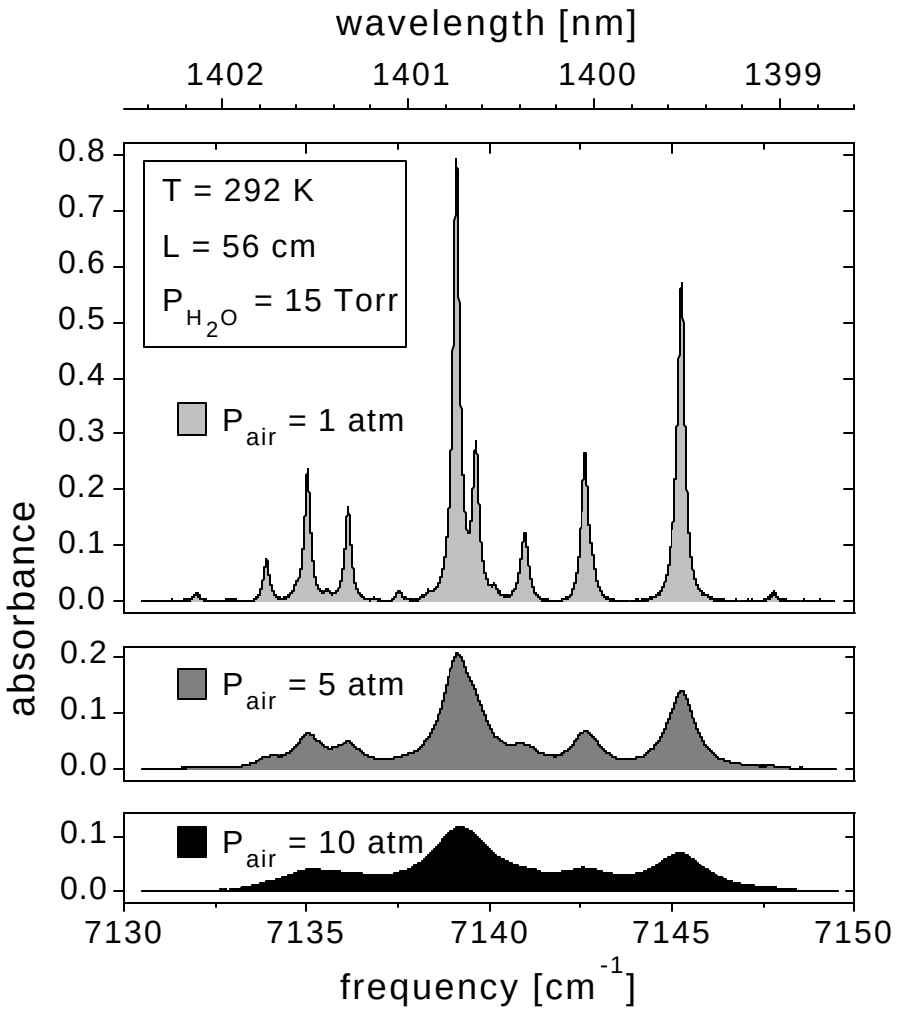

Figure 4.18. Measured H_2O absorption spectra at 1 – 10 atmospheres total gas pressure. The partial pressure of H_2O is held at 15 Torr; the remainder of the gas is dry air. Each measurement is obtained from a single (1 ms duration) scan of the diode laser.

Chapter 5

Conclusions

By exploiting wavelength multiplexing and broad wavelength scanning, diode laser sensing techniques have been extended in many directions. In particular, limitations associated with combustion flow noise (e.g., window birefringence, emission, extinction, window fouling, beamsteering, and mechanical vibration) have been essentially eliminated, at least in flows less harsh than PDEs (while "flow harshness" does not have a simple definition, we can consider, for instance, that typical PDEs emit nearly as strongly as a 4000 K blackbody, extinguish laser beams by ~ 50%, and deflect beams by a few degrees). The key to this noise immunity is the ability to rapidly acquire information at many wavelengths: the noise sources are relatively wavelength-independent, and therefore, strongly wavelength-dependent gas-phase absorption features can be effectively discriminated. In addition, broad spectral information reduces measurement challenges associated with limited spectroscopic data. For instance, by scanning over a full high-pressure lineshape, the total feature area can be accurately extracted even in the typical case where the lineshape broadening parameters are unknown; in short, broad spectral information in a relatively poorly-understood spectrum can often be substituted for narrow spectral information in a well-understood spectrum.

Because they recover increased spectral information, the same techniques that enhance noise immunity and reduce dependence on spectroscopic understanding also enable measurements of high pressure absorbers. This thesis has demonstrated measurements of atomic Cs to ~ 30 atm at 4000 K and H_2O to ~ 20 atm at 3000 K in

PDEs as well as O_2 and H_2O to ~ 10 atm in room temperature static cells. In addition, increased spectral information enables measurements of quasi-broadband absorbers; measurement of the entire Q-branch (containing hundreds of individual transitions) of a C_2H_4 combination band at 1 atm is demonstrated in this thesis.

Finally, broad spectral information has been shown to provide approximate temperature distribution information along a line-of-sight. In this thesis, measurements of O_2 at 1 atm and with temperatures spanning approximately 200 – 800 K have been demonstrated.

In summary, wavelength multiplexing and broad wavelength scanning have dramatically enhanced noise immunity and sensing capabilities. These advancements have enabled a variety of PDE diagnostics and show promise for sensing in many industrial systems.

Appendix A

Reduction of beamsteering noise in laser absorption diagnostics

1. Introduction

Beamsteering, the wander of laser light due to flowfield refractive index gradients, is unavoidable in many laser sensor applications of interest, especially in shocking or combusting flows. Line-of-sight laser sensors must cope with beamsteering effects in order to provide meaningful data, particularly when limited spectral information (sparse wavelength multiplexing or narrow wavelength scanning) is available. Strategic optical design can dramatically reduce the effects of beamsteering, enabling measurements in harsh environments. Four optical designs for reducing the effects of beamsteering are presented here, along with a general strategy for predicting the performance of sensors designed to minimize beamsteering effects.

2. Definition of beamsteering extent

Consider a small-diameter laser beam (relative to the smallest flowfield structures; extensions to large diameter beams are discussed below) that is directed through a combustion flowfield containing time-varying refractive index gradients as shown in Fig. A.1. The laser beam exits with an unsteady lateral offset and angular

displacement that depend on the details of the index gradients. Let us define the beam steering extent anywhere in the system by the two-component vector (r,θ) shown in Figure A.1. Consider the simple optical arrangement shown, aligned but with the combustor turned off. Imagine we were to mark the beam path with the dotted line shown, and then turn on the combustor. If, at any time t and at any location x along this line, we were to measure the offset of the beam r and the angular displacement of the beam θ, we would have fully specified the beam steering. Thus the beam steering extent (r,θ) is a function of (x,t).

Fortunately, we can simplify the steering extent concept in a way that will prove useful in determining the limits of beamsteering noise removal. Consider any point x in Fig. A.1 that is downstream of the combustor, $x > x_1$. In this region, no beamsteering takes place; the beam is merely transmitting the steering it acquired while passing through the flow. Optics texts (e.g., Welford 1978) demonstrate that the function $r \sin \theta$ will be conserved for any optimized optical system transforming this beam (etendue conservation). Specifically, using only a lens, a steering extent at point x_1 of (r_1,θ_1) can be transformed to any other steering extent (r_2,θ_2) at a point x_2 as long as $r_1 \sin \theta_1 = r_2 \sin \theta_2$. In the paraxial limit (small angles θ; less than approximately 15 degrees), this transformation condition reduces to $r_1\theta_1 = r_2\theta_2$, and the product $r_1\theta_1$ is called the etendue. Figure A.2 presents an example, where a lens transforms light emitted at ≤ 3 degrees from a 4 mm diameter aperture to ≤ 12 degrees, 1 mm; the etendue 12 mm°deg is held constant. We therefore need only consider the product $r_1\theta_1$ (shown in Fig. A.1) versus time to specify the steering extent. If we are concerned only with the worst steering event in a flow, we can drop the time dependence and consider only $(r_1\theta_1)_{max}$. Also, we

can remove our prerequisite that the laser beam be small compared to the flowfield structures by letting $(r_1\theta_1)_{max}$ describe the most severely-steered portion of the beam. We henceforth adopt the maximum expected product of offset and angular displacement at the ouput optical port of a given combustor, $(r_1\theta_1)_{max}$, as that combustor's beamsteering extent.

3. Acceptable beamsteering extent of a detection system

We may now easily determine the maximum steering a given detection system can accept, as limited by various components in the system. Typically, the detector will be the limiting component. The detector will have an active area radius r_d with adequately uniform sensitivity and will accept rays at an angle $< \theta_d$ from the normal to the active area without significant loss of quantum efficiency. The product $r_d\theta_d$ will be the maximum steering extent we can hope the detection system to accommodate.

4. Predicting a flowfield's beamsteering extent

The ability to predict a flowfield's beamsteering extent will prove invaluable in determining *a priori* whether a laser diagnostic can accommodate the beamsteering of a given combustor. Shock waves and turbulent flow layers are the dominant sources of beam steering encountered by optical diagnostics of combusting flows.

Snell's law has been used successfully to calculate the steering of a beam by a shock wave (Kiefer et al. 1981) as demonstrated in Figure A.3. Estimates of the gas densities on both sides of the shock are sufficient to estimate the steering using the approximate relation

$$\frac{n-1}{n_{ref}-1} \approx \frac{\rho}{\rho_{ref}} \qquad \text{(eq. A.1)}$$

where n and n_{ref} are the unknown and reference refractive indices, and ρ and ρ_{ref} are the gas densities. For reference, a typical beamsteering extent observed during detonation wave passage (in a 4 cm diameter detonation tube) is 10 mm°deg; this observed value is approximately what can be calculated using rudimentary raytracing ideas as shown in Fig. A.3.

Turbulent flow structures can significantly steer beams, particularly if the average eddy size is larger than the beam diameter (Petersen et al. 1997). The steering extent depends upon the details of the turbulence (Sutton 1969), but has been shown to be proportional to $D^{-1/6}L^{3/2}$, where D is the beam diameter and L is the path length of turbulent flowfield (Churnside et al. 1989). Using this rule, small-scale combustor behavior can be extrapolated to predict the steering extent of larger combustors.

5. Four anti-beamsteering detection systems

We demonstrated for a simple case in section 3 the maximum theoretical beamsteering extent a specific detection system could accommodate. This maximum was based on the detector size and angular aperture. The result is not, however, universal to all detection systems. Nor does it represent the ultimate maximum beamsteering extent acceptable, even for that particular detector. This is because modifications can be made to a detection system to extend the beamsteering extent acceptability. Alternatively, modifications that must be made to the detection system, i.e. to demultiplex several wavelengths, can compromise the result found in section 3.

Figure A.4 presents four potential detection schemes. Scheme (1) is a repeat of Figure A.1, presented for comparison. We have shown that the maximum acceptable beamsteering extent for this scheme, as limited by the detector, is the etendue $r_{detector}\theta_{detector}$.

Scheme (2) represents an adaptation of scheme (1), including a diffraction grating to demultiplex multiple wavelengths. The grating generally compromises the maximum acceptable beamsteering extent, because its efficiency varies with incidence angle. A specific example of this characteristic is shown in Figure A.5, which indicates that steering of a beam incident on a grating is transmitted as an intensity fluctuation to the detector. Furthermore, laser beam polarization plays a role. The lens ahead of the grating in scheme (2) is designed to collimate the light onto the grating to reduce this grating efficiency effect.

Schemes (3) and (4) are modifications of scheme (1) designed to extend the maximum acceptable beamsteering extent. Scheme (3) employs a retroreflector array (similar to a road sign that retroreflects car headlights, making signs readable at long

distances) to return the laser through the flow in a double-pass arrangement. This idea is an adaptation of the concept used for wavefront correction in imaging through atmospheric turbulence (Chipman et al. 1988). In principle, rays that nearly retrace their paths will "un-steer" in the backward direction all the steering acquired in the forward direction, finally leaving the flow with a greatly reduced steering extent. Three main types of retroreflectors, shown in Figure A.6, can be used in the array; the corner cube is most popular because its efficiency is highest. However, like the grating, the corner-cube retroreflector array has a varying efficiency with input angle, shown in Figure A.7. Figure A.7 was generated by detailed raytrace computations; the decreasing efficiency is due to an increasing fraction of rays that enter the cube but do not strike all three sides before exiting as the incidence angle increases. Again, the lens shown in scheme (3) is designed to nearly collimate the light onto the retroreflector array to reduce this unwanted angular sensitivity. A single retroreflector could be used rather than an array, but, as shown in Figure A.6, the retroreflected beam is offset from the input beam by a dimension on the order of the retroreflector size. In general, the retroreflectors must be kept smaller than the smallest steering structures in the flow, and arrays of miniature retroreflectors are often suitable for this purpose. However, diffraction from arrays with very small retroreflectors initiates an undesirable beam "spread" upon retroreflection.

Scheme (4) utilizes an integrating sphere to increase the maximum acceptable beamsteering extent by relieving the constraints associated with the direct incidence of light onto a detector. A detector will usually have a nonuniform sensitivity across its active area and a quantum efficiency that varies with incidence angle; therefore it will be sensitive to beam steering. The sphere transforms light of arbitrary nature entering one of

its ports into uniform, diffusely emitted light at all ports. If the detector monitors the light output from a sphere's port, the properties of the input port of the sphere, rather than those of the detector, define the maximum acceptable beamsteering extent of the entire collection system. The radius of the input port, r_{port}, can easily be made large, and it can accept incidence angles, θ_{port}, of nearly 90 degrees. Therefore the maximum acceptable beamsteering extent for the sphere-based collection system, $r_{port}\sin\theta_{port}$, is relatively large (note that since θ_{port} is large in this case, the quantity $r_{port}\sin\theta_{port}$ is used rather than $r_{port}\theta_{port}$).

Integrating spheres have been used successfully to reduce beamsteering noise in detection systems by several orders (Petersen et al. 1997). The main drawback of the integrating sphere is its low throughput, which is usually on the order of 1%. The throughput depends on the reflectivity of the sphere's interior, the sizes of the ports and sphere, and the detector size and proximity to the output port. The sphere also has a secondary drawback: it acts as a low-pass filter to modulated light (i.e., a 10 ns pulse entering a typical sphere will exit as a relatively long exponential decay). This characteristic may have repercussions for modulation-based spectroscopic techniques.

6. Discussion

We have seen that the grating and retroreflector have angular sensitivities that complicate the anti-beamsteering system optimization process. In fact, nearly all components in an absorption diagnostic system demonstrate such angular sensitivities. The transmittance of lenses and windows versus incident angle can lead to significant beamsteering noise. Such effects must be folded into system analyses. Practical factors such as dirty optics can also play a significant role. For these reasons, the number of optics downstream of the beam-steering flow should be minimized whenever possible.

7. Conclusions

The flowchart shown in Fig. A.8 is a useful guide for properly managing beamsteering in direct absorption measurements. Because anti-beamsteering detection systems can be laborious to incorporate, Fig. A.8 attempts to offer alternate solutions to beamsteering and suggests anti-beamsteering detection systems as a last resort. However, in many cases, the anti-beamsteering detection systems, discussed above in section A.5, are required. The best anti-beamsteering detection system depends strongly on the application, and therefore must be chosen on a case-by-case basis. The primary factors for selecting an anti-beamsteering detection system are listed in the lower box of Fig. A.8. In the PDE work presented in this thesis, scheme (2) was used most regularly because the small steering structures present in PDEs disable scheme (3) and the low sphere throughput usually disables scheme (4).

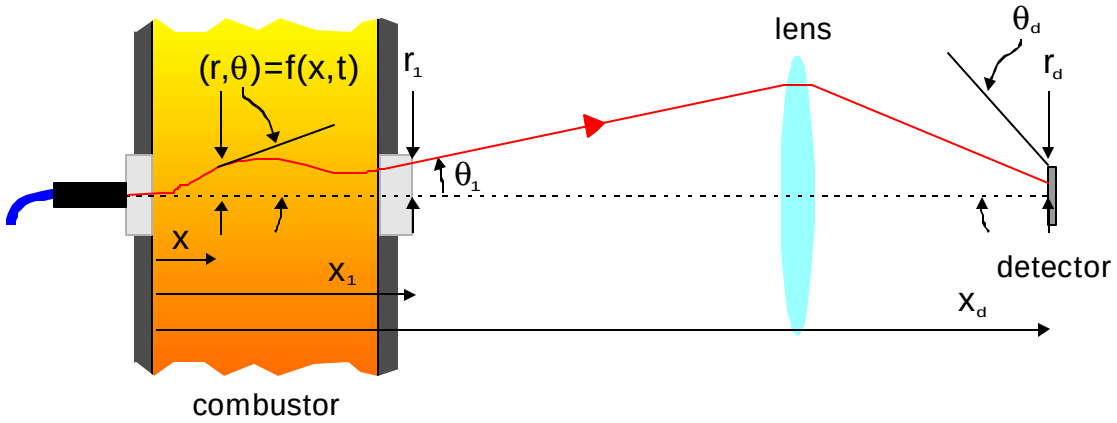

Figure A.1. Detail of a laser absorption sensor applied to a combustor possessing strong refractive index gradients.

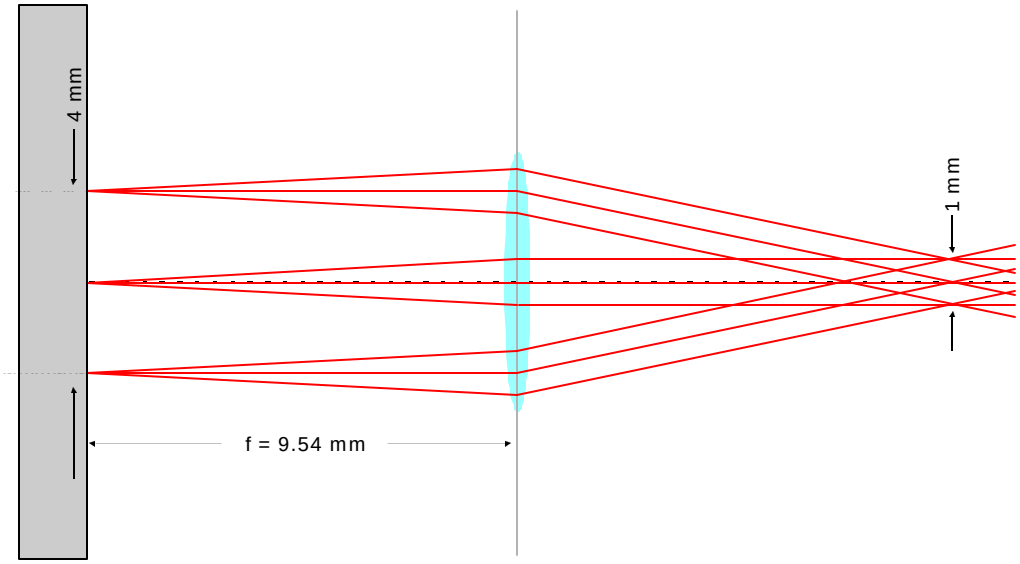

Figure A.2. Example etendue-conserving transformation. Light originates from a 4mm aperture at angles < 3 degrees from the horizontal. The lens transforms the light such that it fills a smaller (1mm) region but at increased angles (< 12 degrees). The etendue of 12 mm°deg is unchanged by the transformation.

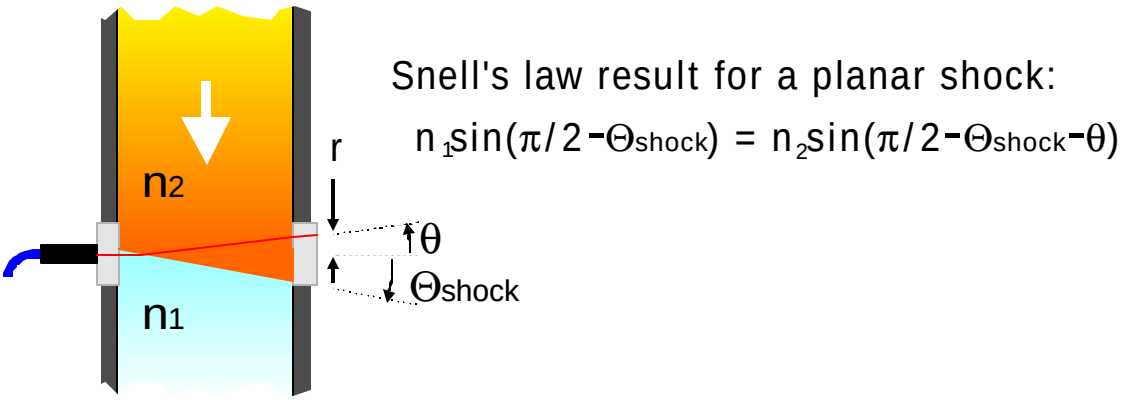

Figure A.3. Schematic used to compute the beamsteering induced by a planar shock wave (modeled as a step change in refractive index).

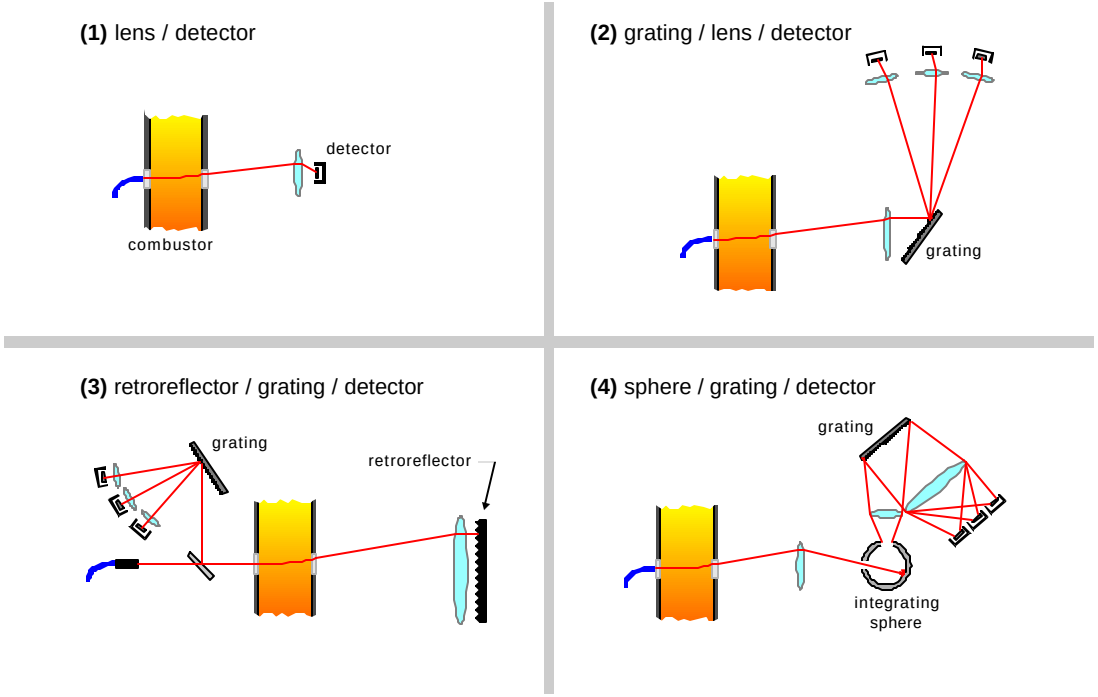

Figure A.4. Four anti-beamsteering collection schemes.

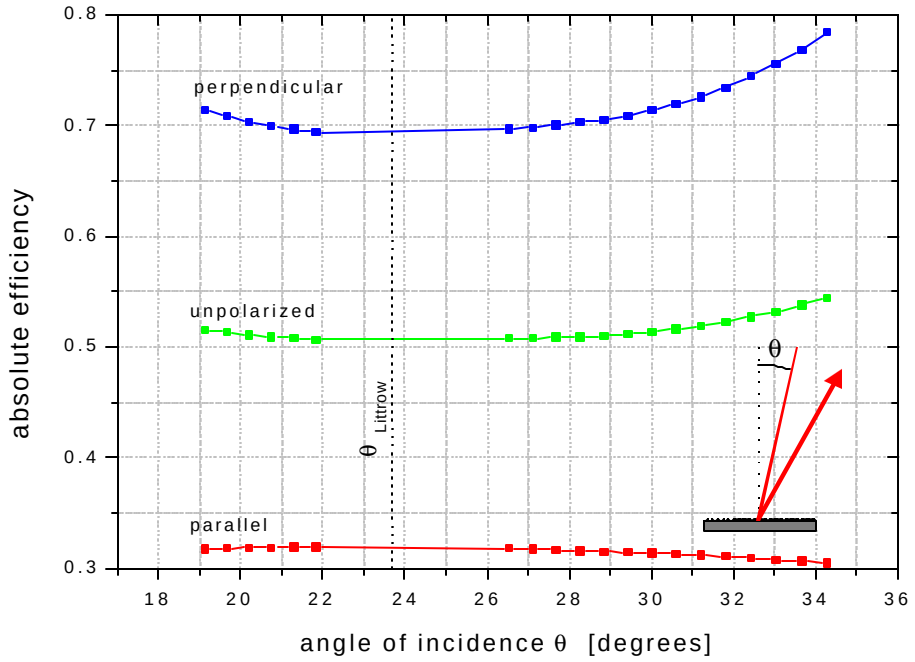

Figure A.5. Angular response of 600 g/mm ruled reflection grating, blaze angle 17.45°, λ = 1343 nm. The grating's efficiency is least sensitive to input angle when used in the near-Littrow configuration.

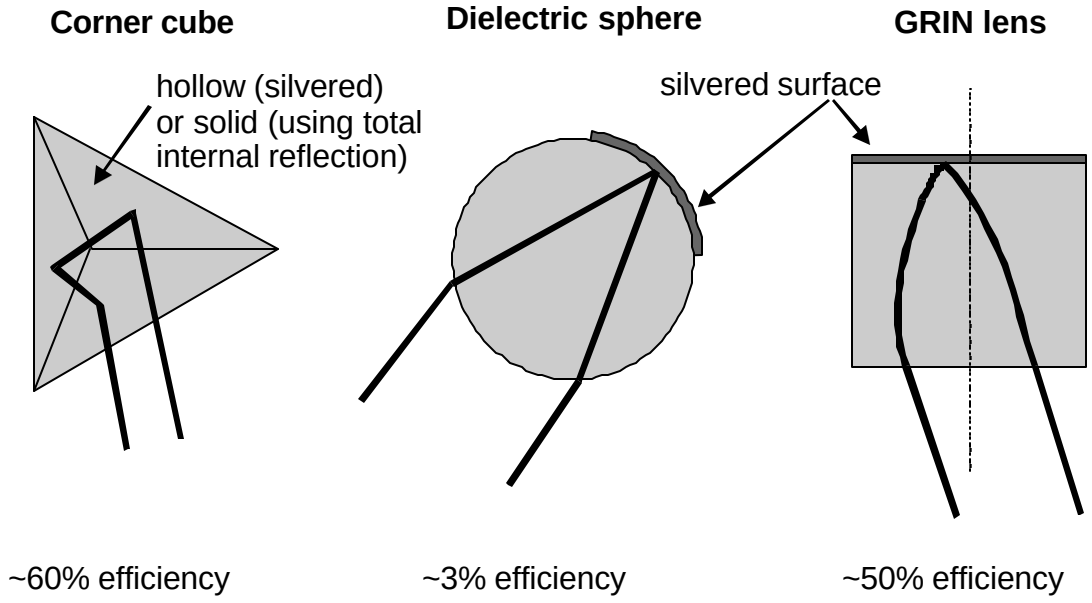

Figure A.6. Three common retroreflectors.

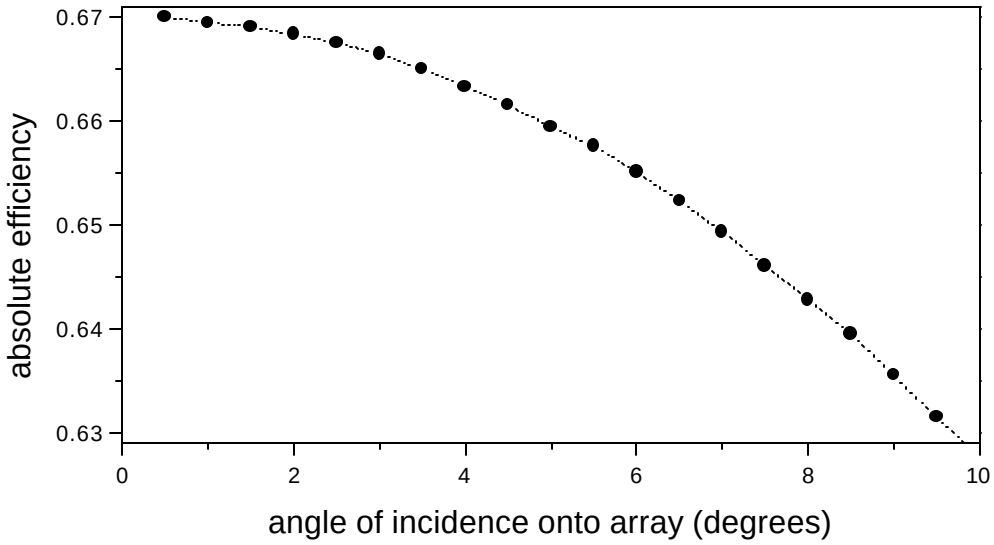

Figure A.7. Angular response of an array of corner-cube retroreflectors. As in the case of the diffraction grating, the angular sensitivity of the retroreflector array's efficiency is a potential source of beamsteering noise.

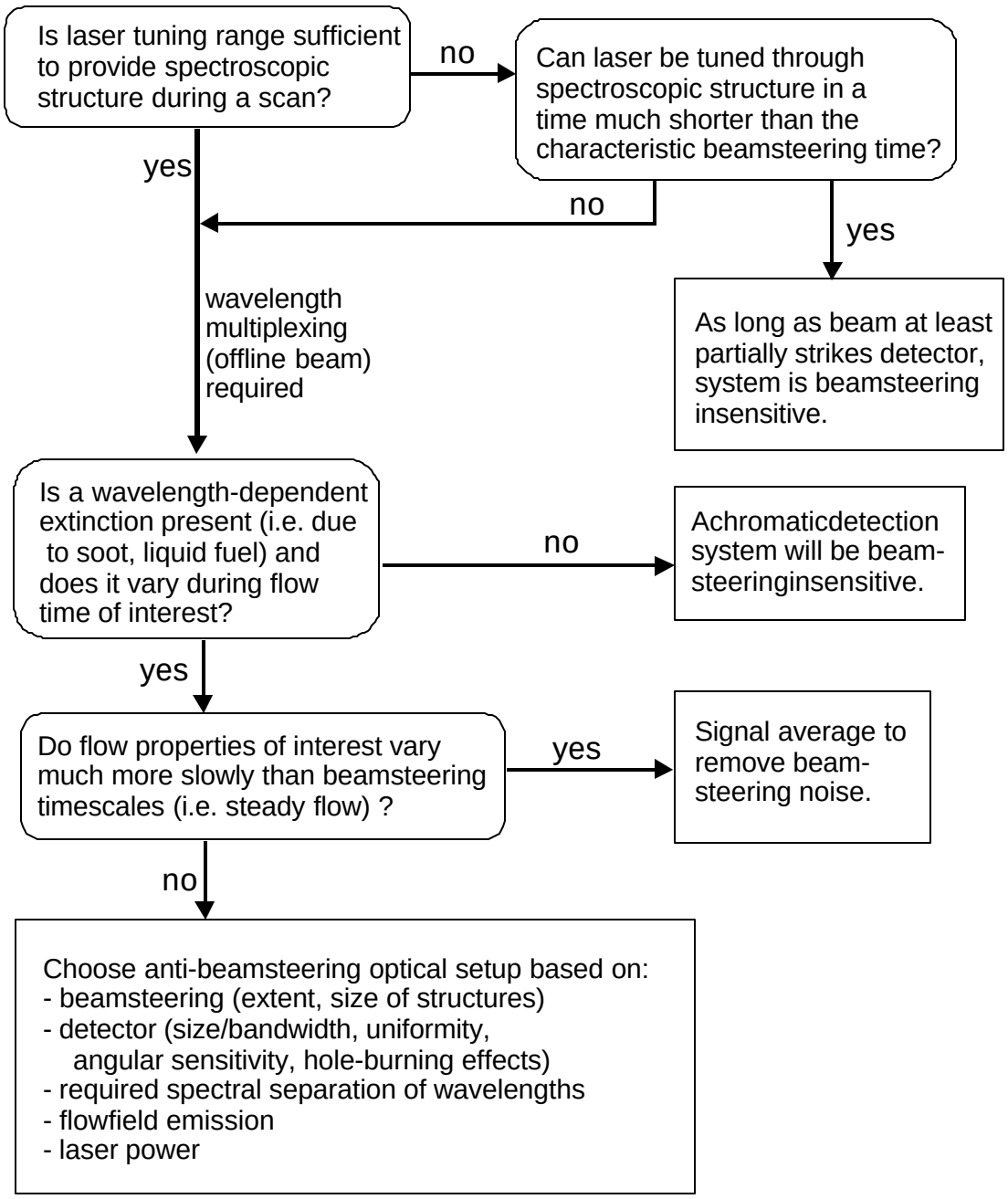

Figure A.8. Flowchart for managing beamsteering in laser absorption experiments.

Appendix B

Seeding atomic absorbers for time-of-flight velocimetry

1. Salt-coated surfaces

To facilitate the velocimetry described in section 3.4, CsCl salt is applied to a stainless steel needle held in the center of a PDE (see Fig. 3.8). Shortly after the saltwater is applied to the needle, the water evaporates and CsCl salt crystallizes on the needle surface, coating it with fine (~ 10 μm) salt grains shown in Fig. B.1. When the salt-coated needle is subjected to the detonated-gas flow, the high heat transfer and shear continuously melt and deform the salt grains; in addition, salt fragments or entire salt grains are frequently stripped from the needle. A microscope image of salt remnants on a needle after three detonations is shown in Fig. B.2.

A salt particle stripped from the needle rapidly equilibrates to the local gas conditions, exploding to form a gas cloud of at least 1000 times the original particle volume (a 3 μm × 3 μm × 3 μm crystal forms a cloud with dimensions on the order of 30 μm). Turbulence continuously spreads the cloud and mixes it with nearby clouds; since the dominant eddy size in the detonated-gas flow should be roughly one-tenth the tube diameter, we might expect the Cs clouds to be spread over approximately 4 mm in this 4 cm diameter tube. Such spreading is in fact observed; the dominant Cs absorption structures in Fig 3.9 exhibit a width of approximately 4 μs, corresponding to Cs

structures of roughly 4 mm in size. The measured structures maintain this approximate size during the majority of the detonated-gas exhaust.

Atomic absorbers such as Cs are strong enough that a single salt particle causes deep absorption structure downstream of the seeding surface (a 3 μm × 3 μm × 3 μm CsCl crystal, spread over ~ 3 mm by turbulence, will cause ~ 90% absorption of a resonant laser beam). Since very few salt particles contribute to the absorption signal, the statistics of the salt release cause the signal to contain intense structure.

The time-of-flight velocimetry technique depends on the formation of such intense absorption structures at the probe beam locations. The structure is governed by flow properties (the shear at the seeding surface and the turbulence just downstream) that may not be adjustable by the diagnostician. However, the structure is also governed by the salt coating properties (size and adhesiveness of grains) which can, in principle, be tailored to increase the distinctiveness of the absorption structures and thereby optimize the time-of-flight velocimetry technique.

2. Alternative seeding techniques

For flows in which seeding from a salt-coated surface is not effective (e.g., due to a relatively slow flow with inadequate shear at the seeding surface), alternative seeding techniques can be employed to revive time-of-flight velocimetry. For example, the needle could be replaced by a solid structural rod containing the atomic absorber of interest. A pulsed laser, focused onto the rod, could be used to ablate clouds of the

absorber in any desired fashion. Ultrasonic actuators to drive periodic material release can also be envisioned. In short, seeding for time-of-flight velocimetry should be possible in most flows, as long as intrusive seeding surfaces are allowed into the flow.

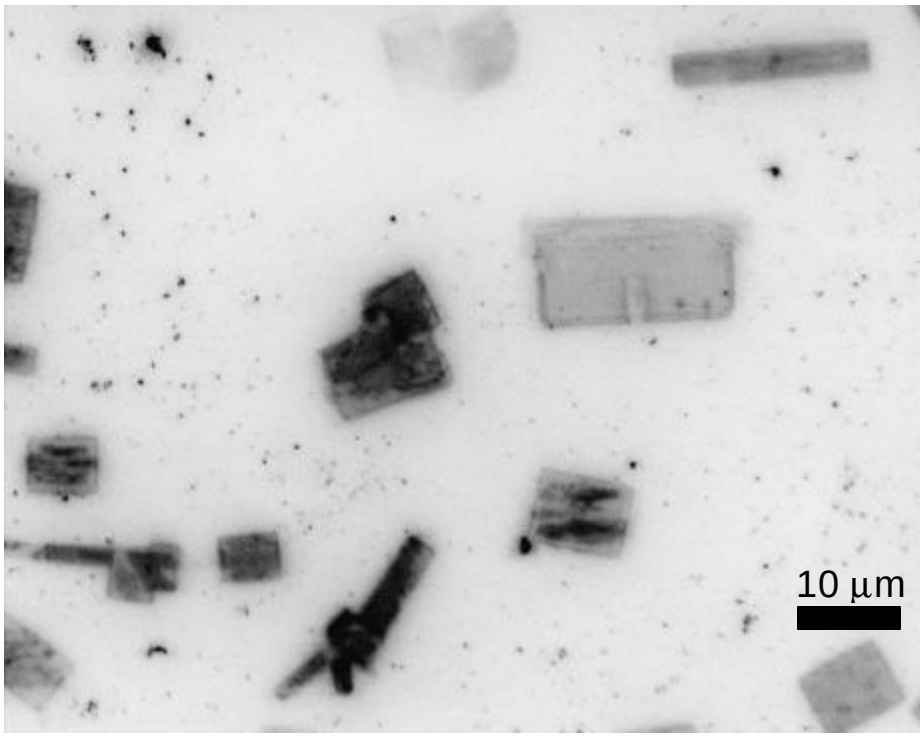

Figure B.1. Image of KCl crystals on a flattened stainless steel seeding needle. A solution of saltwater and fluorescein dye was painted onto the needle; after drying, this image was acquired using fluorescence microscopy.

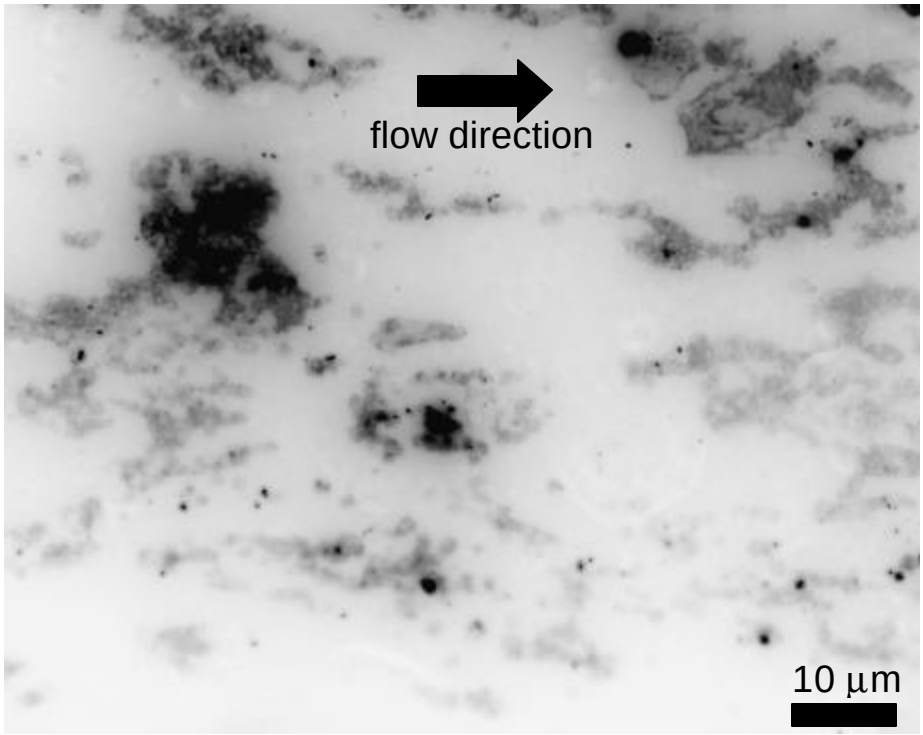

Figure B.2. Same as Fig. B.1, but after three detonations had traversed the needle in the direction shown. Salt crystals have been melted and deformed; fragments and crystals have been stripped from the stainless steel surface.

References

Allen, M. G. (1998). Diode laser absorption sensors for gas-dynamic and combustion flows. *Meas. Sci. Technol. 9*, 545-562.

Arroyo, M. P. and R. K. Hanson (1993). Absorption-measurements of water-vapor concentration, temperature, and line-shape parameters using a tunable InGaAsP diode-laser. *Appl. Opt. 32*, 6104-6116.

Arroyo, M. P., S. Langlois, and R. K. Hanson (1994). Diode-laser absorption technique for simultaneous measurements of multiple gasdynamic parameters in high-speed flows containing water vapor. *Appl. Opt. 33*, 3296-3307.

Baer, D. S. and R. K. Hanson (1992). Tunable diode-laser absorption diagnostics for atmospheric-pressure plasmas. *J. Quant. Spectrosc. Radiat. Transfer 47*, 455-475.

Baer, D. S., V. Nagali, E. R. Furlong, R. K. Hanson, and M. E. Newfield (1996). Scanned- and fixed-wavelength absorption diagnostics for combustion measurements using multiplexed diode lasers. *AIAA J. 34*, 489-493.

Brock, A., N. Mina-Camilde, and C. Manzanares I (1994). Vibrational spectroscopy of C–H bonds of C_2H_4 liquid and C_2H_4 in liquid Argon solutions. *J. Phys. Chem. 98*, 4800-4808.

Brophy, C. M., D. W. Netzer, J. O. Sinibaldi, and R. G. Johnson (2000). Operation of a JP-10 / air pulse detonation engine. Paper 3591 at *36th AIAA/ASME/SAE/ASEE Joint Propulsion Conference*, Huntsville, AL.

Bussing, T. and G. Pappas (1994). An introduction to pulse detonation engines. Paper 0263 at the *32nd AIAA Aerospace Sciences Meeting*, Reno, NV.

Caron, J. N., Y. Q. Yang, J. B. Mehl, and K. V. Steiner (1998). Gas-coupled laser acoustic detection at ultrasonic and audio frequencies. *Rev. Sci. Inst. 69*, 2912-2917.

Chang-Hasnain, C. J. (2000). Tunable VCSEL. *IEEE J. Sel. Top. Quant. Elect. 6***,** 978-987.

Chipman, R.A., J. Shamir, H. J. Caulfield, and Q. B. Zhou (1988). Wavefront correcting properties of corner cube arrays. *Appl. Opt. 27*, 3203-3209.

Chou, S. I., D. S. Baer, R. K. Hanson, W. Z. Collison, and T. Q. Ni (2001). HBr concentration and temperature measurements in a plasma etch reactor using diode laser absorption spectroscopy. *J. Vac. Sci. Tech. A 19*, 477-484.

Churnside, J. H. and R. J. Lataitis (1989). Wander of an optical beam in the turbulent atmosphere. *Appl. Opt. 29*, 926-930.

Coldren, L. A. (2000). Monolithic tunable diode lasers. *IEEE J. Sel. Top. Quant. Elect. 6***,** 988-999.

Eidelman, S. (1997). Pulse Detonation Engine: A Status Review and Technology Development Road Map. Paper 2740 at the *33rd AIAA/ASME/SAE/ASEE Joint Propulsion Conference*, Seattle, WA.

Furlong, E. R., R. M. Mihalcea, M. E. Webber, D. S. Baer, and R. K. Hanson (1999). Diode-laser sensors for real-time control of pulsed combustion systems. *AIAA J. 37*, 732-737.

Furlong, E. R. (1998). Diode-laser absorption spectroscopy applied for the active control of combustion. Ph.D. Thesis, Stanford University, Stanford, CA.

Georges, R., M. Bach, and M. Herman (1997). High resolution FTIR spectroscopy using a slit jet: sampling the overtone spectrum of C_2H_4. *Mol. Phys. 90*, 381-387.

Hanson, R. K. (1977). Shock-tube spectroscopy: advanced instrumentation with a tunable diode-laser. *Appl. Opt. 16,* 1479-1481.

Hanson, R. K. (1980). Absorption-spectroscopy in sooting flames using a tunable diode-laser. *Appl. Opt. 19,* 482-484.

Kailasanath, K. and G. Patnaik (2000a). Performance estimates of pulsed detonation engines. *Proc. Comb. Inst. 28,* 595-601.

Kailasanath, K., C. Li, E. Chang, and G. Patnaik (2000b). Computational studies of pulsed detonation engines. *13th ONR Propulsion Conference*, Minneapolis, MN.

Kiefer, J.H., and A. C. Manson (1981). Refractive index change and curvature in shock waves by angled beam refraction. *Rev. Sci. Inst. 52,* 1392-1396.

Lee S. Y., C. Conrad, J. Watts, R. Woodward, S. Pal, and R. J. Santoro (2000). Deflagration to detonation transition study using simultaneous Schlieren and OH PLIF images. Paper 3217 at the *36th AIAA/ASME/SAE/ASEE Joint Propulsion Conference*, Huntsville, AL.

Li, C., K. Kailasanath, and G. Patnaik (2000). A numerical study of flow field evolution in a pulsed detonation engine. Paper 0314 at the *38th AIAA Aerospace Sciences Meeting and Exhibit*, Reno, NV.

Li, D., N. J. Bowring, and J. G. Baker (1993). A scanning temperature control system for laser diodes. *Meas. Sci. Technol. 4*, 1111-1116.

Mihalcea, R. M., M. E. Webber, D. S. Baer, and R. K. Hanson (1998). Combustion Emissions Measurements Using Diode-Laser Sensors. Paper 3948 at the *34th AIAA/ASME/SAE/ASEE Joint Propulsion Conference*, Cleveland, OH.

Mohanraj, R., C. L. Merkle, and H. B. Ebrahimi (2001). Modeling of pulse detonation engine operation. Paper 0475 at the *39th AIAA Aerospace Sciences Meeting*, Reno, NV.

Nagali, V., J. T. Herbon, D. C. Horning, D. F. Davidson, and R. K. Hanson (1999). Shock-tube study of high-pressure H_2O spectroscopy. *Appl. Opt. 38*, 6942-6950.

Nagali, V., S. I. Chou, D. S. Baer, and R. K. Hanson (1997). Diode-laser measurements of temperature-dependent half-widths of H_2O transitions in the 1.4 μm region. *J. Quant. Spectrosc. Radiat. Transfer 57*, 795-809.

Nefedov, A. P., V. A. Sinel'shchikov, and A. D. Usachev (1999). Collisional broadening of the Na-D lines by molecular gases. *Physica Scripta 59*, 432-442.

Petersen E. L., R. W. Bates, D. F. Davidson, and R. K. Hanson (1997). Development of laser absorption techniques for shock tube studies at elevated pressures. Paper 4605 at the *21st International Symposium on Shock Waves*, Great Keppel Island, Australia.

Rothman, L. S., C. P. Rinsland, A. Goldman, S. T. Massie, D. P. Edwards, J. M. Flaud, A. Perrin, C. CamyPeyret, V. Dana, and J. Y. Mandin (1998). The HITRAN molecular spectroscopic database and HAWKS (HITRAN Atmospheric Workstation): 1996 edition. *J. Quant. Spectrosc. Radiat. Transfer 60*, 665-710.

Sanders, S. T., T. M. Muruganandam, D. W. Mattison, and R. K. Hanson (2001a). Diode-laser sensors for detonation flows. Paper 5733 at the *23rd International Symposium on Shock Waves*, Fort Worth, TX.

Sanders, S. T., J. Wang, J. B. Jeffries, and R. K. Hanson (2001b). Diode-laser absorption sensor for line-of-sight gas temperature distributions. *Appl. Opt. 40*, 4405-4415.

Sanders, S. T., D. W. Mattison, L. Ma, and R. K. Hanson (2001c). Diode-laser sensors for pulse detonation engines. Paper 143 at the *2nd Joint Meeting of the US Sections of the Combustion Institute*, Oakland, CA.

Sanders, S. T., D. W. Mattison, J. B. Jeffries, and R. K. Hanson (2001d). Rapid temperature tuning of a 1.4-μm diode laser with application to high-pressure H_2O absorption spectroscopy. *Opt. Lett. 26,* 1568-1570.

Sanders, S. T., D. W. Mattison, T. M. Muruganandam, and R. K. Hanson (2001e). Multiplexed diode-laser absorption sensors for aeropropulsion flows. Paper 0412 at the *39th AIAA Aerospace Sciences Meeting*, Reno, NV.

Sanders, S. T., J. A. Baldwin, T. P. Jenkins, D. S. Baer, and R. K. Hanson (2000a). Diode-laser sensor for monitoring multiple combustion parameters in pulse detonation engines. *Proc. Comb. Inst. 28*, 587-594.

Sanders, S. T., T. P. Jenkins, and R. K. Hanson (2000b). Diode laser sensor system for multi-parameter measurements in pulse detonation engine flows. Paper 3592 at the *36th AIAA/ASME/SAE/ASEE Joint Propulsion Conference*, Huntsville, AL.

Sanders, S. T., T. P. Jenkins, J. A. Baldwin, D. S. Baer, and R. K. Hanson (2000c). Diode laser absorption sensor for measurements in pulse detonation engines. Paper 0358 at the *38th AIAA Aerospace Sciences Meeting*, Reno, NV.

Schauer, F., J. Stutrud, and R. Bradley (2001). Detonation initiation studies and performance results for pulsed detonation engine applications. Paper 1129 at the *39th AIAA Aerospace Sciences Meeting*, Reno, NV.

Seasholtz, R. G., A. E. Buggele, and M. F. Reeder (1997). Flow measurements based on Rayleigh scattering and Fabry-Perot interferometer. *Opt. and Lasers in Eng. 27*, 543-570.

Shepherd, J. E., J. M. Austin, T. Chao, F. Pintgen, E. Wintenberger, S. Jackson, and M. Cooper (2001). Detonation Initiation, Propagation, and Structural Response. *14th ONR Propulsion Conference*, Chicago, IL.

Silver, J. A., D. J. Kane, and P. S. Greenberg (1995). Quantitative species measurements in microgravity flames with near-IR diode lasers. *Appl. Opt. 34*, 2787-2801.

Sutton, G.W. (1969). Effect of turbulent fluctuations in an optically active fluid medium. *AIAA J. 7*, 1737-1743.

Teulet, P. (1998). Etude des ecarts a l'equilibre radiatif et thermique dans les plasmas air et air-sodium. Application au diagnostic spectroscopique. Ph.D. Thesis, Universite Paul Sabatier, Toulouse, France.

Teulet, P., J. P. Sarrette, and A. M. Gomes (2000). Collisional-radiative modelling of one- and two-temperature air and air-sodium plasmas at atmospheric pressure with temperatures of 2000-12000K. *J. Quant. Spect. & Rad. Trans. 70*, 159-187.

Thompson, P. A. (1971). *Compressible-fluid dynamics*. New York: McGraw-Hill.

Varghese, P. L. and R. K. Hanson. Tunable infrared diode-laser measurements of line strengths and collision widths of 12C16O at room temperature. *J. Quant. Spect. & Rad. Trans. 24*, 479-489.

Vogel, P. and V. Ebert (2001). Near shot noise detection of oxygen in the A-band with vertical-cavity surface-emitting lasers. *Appl. Phys. B. 72*, 127-135.

Wang. J., M. Maiorov, D. S. Baer, D. Z. Garbuzov, J. C. Connolly, and R. K. Hanson (2000). *In situ* combustion measurements of CO with diode-laser absorption near 2.3 μm. *Appl. Opt. 39*, 5579-5589.

Wang, J. (2001a). New Strategies of Diode Laser Absorption Sensors. Ph.D. Thesis, Stanford University, Stanford, CA.

Wang, J., S. T. Sanders, J. B. Jeffries, and R. K. Hanson (2001b). Oxygen measurements at high pressures with vertical cavity surface-emitting lasers. *Appl. Phys. B 72*, 865-872.

Webber, M. E., D. S. Baer, and R. K. Hanson (2001). Ammonia monitoring near 1.5 μm with diode-laser absorption sensors. *Appl. Opt. 40*, 2031-2042.

Wehe, S. D., D. S. Baer, and R. K. Hanson (1999). Diode-laser sensor for velocity measurements in hypervelocity flows. *AIAA J 37*, 1013-1015.

Wehe, S.D. (2000). Development of a tunable diode laser probe for measurements in hypervelocity flows. Ph.D. Thesis, Stanford University, Stanford, CA.

Welford, W.T., and R. Winston (1978). *The optics of nonimaging concentrators*, New York: Academic Press.